WAVE-EQUATION MIGRATION VELOCITY ANALYSIS USING IMAGE-SPACE GENERALIZED SOURCES

A DISSERTATION
SUBMITTED TO THE DEPARTMENT OF GEOPHYSICS
AND THE COMMITTEE ON GRADUATE STUDIES
OF STANFORD UNIVERSITY
IN PARTIAL FULFILLMENT OF THE REQUIREMENTS
FOR THE DEGREE OF
DOCTOR OF PHILOSOPHY

Claudio Guerra
June 2010

I certify that I have read this dissertation and that, in my opinion, it is fully adequate in scope and quality as a dissertation for the degree of Doctor of Philosophy.

(Biondo Biondi) Principal Adviser

I certify that I have read this dissertation and that, in my opinion, it is fully adequate in scope and quality as a dissertation for the degree of Doctor of Philosophy.

(Jon F. Claerbout)

I certify that I have read this dissertation and that, in my opinion, it is fully adequate in scope and quality as a dissertation for the degree of Doctor of Philosophy.

(Jerry Harris)

Approved for the University Committee on Graduate Studies.

Abstract

Preface

The electronic version of this report[1] makes the included programs and applications available to the reader. The markings **ER**, **CR**, and **NR** are promises by the author about the reproducibility of each figure result. Reproducibility is a way of organizing computational research that allows both the author and the reader of a publication to verify the reported results. Reproducibility facilitates the transfer of knowledge within SEP and between SEP and its sponsors.

ER denotes Easily Reproducible and are the results of processing described in the paper. The author claims that you can reproduce such a figure from the programs, parameters, and makefiles included in the electronic document. The data must either be included in the electronic distribution, be easily available to all researchers (e.g., SEG-EAGE data sets), or be available in the SEP data library[2]. We assume you have a UNIX workstation with Fortran, Fortran90, C, X-Windows system and the software downloadable from our website (SEP makerules, SEPScons, SEPlib, and the SEP latex package), or other free software such as SU. Before the publication of the electronic document, someone other than the author tests the author's claim by destroying and rebuilding all ER figures. Some ER figures may not be reproducible by outsiders because they depend on data sets that are too large to distribute, or data that we do not have permission to redistribute but are in the SEP data library, or that the rules depend on commercial packages such as Matlab or Mathematica.

---

[1] http://sepwww.stanford.edu/private/docs/sep137

[2] http://sepwww.stanford.edu/public/docs/sepdatalib/toc_html

CR denotes Conditional Reproducibility. The author certifies that the commands are in place to reproduce the figure if certain resources are available. The primary reasons for the CR designation is that the processing requires 20 minutes or more.

NR denotes Non-Reproducible figures. SEP discourages authors from flagging their figures as NR except for figures that are used solely for motivation, comparison, or illustration of the theory, such as: artist drawings, scannings, or figures taken from SEP reports not by the authors or from non-SEP publications. Some 3D synthetic data examples associated with this report are classified as NR because they were generated externally to SEP and only the results were released by agreement.

Our testing is currently limited to LINUX 2.6 (using the Intel Fortran90 compiler) and the SEPlib-6.4.6 distribution, but the code should be portable to other architectures. Reader's suggestions are welcome. For more information on reproducing SEP's electronic documents, please visit *http://sepwww.stanford.edu/research/redoc/*.

Acknowledgments

Contents

List of Tables

List of Figures

Chapter 1

Introduction

Chapter 2

Pre-Stack Exploding-Reflector Model

This chapter introduces the pre-stack exploding-reflector model (PERM). PERM uses *exploding* reflectors as the initial conditions to synthesize data, in a manner similar to the well-known exploding-reflector model (ERM). However, PERM also considers reflectivity as a function of subsurface-offsets, as opposed to the zero-subsurface offset initial condition used by ERM. In this sense, PERM is a generalization of ERM since wave-equation migration of PERM data can generate a pre-stack image, which is not achievable with ERM. The modeling of PERM data can be performed using any wave propagation scheme; here I use the one-way wave-equation. PERM shares with ERM the ability to perform multiple modeling experiments simultaneously, greatly reducing data volume. Data size reduction is very appealing for migration velocity analysis, especially using wavefield-extrapolation methods in 3D projects. After describing the exploding-reflector concept, I generalize it by describing the theory of PERM. The usefulness of PERM to migration velocity analysis, is demonstrated through migration examples.

INTRODUCTION

Migration is applied to seismic data to generate an image of the subsurface. For many years, migration was applied only in the post-stack domain, using the idea of exploding reflectors (Loewenthal et al., 1976; Claerbout, 1985). The simple but powerful concept of the exploding-reflector model (ERM) states that a zero-offset time section can be considered as the recording at the surface of wavefields generated by simultaneous explosions of all points in the subsurface. The strength of the explosions is proportional to the reflection coefficient and, because the wavefield propagates from the subsurface to the surface, to obtain correct kinematics the medium velocity must be halved.

Migration in the post-stack domain assumes that data is transformed to some approximation of the zero-offset acquisition geometry. Because of the required transformation to zero-offset, many algorithms have been developed, including dip moveout (DMO — Hale (1984); Black and Egan (1988); Liner (1991)), migration to zero-offset (MZO — Tygel et al. (1998); Bleistein et al. (1999), and common-reflection surface (Gelchinsky, 1988; Cruz et al., 2000). DMO and MZO can be considered very particular cases of the more general azimuth moveout (AMO — (Biondi et al., 1998)), which must be applied to 3D data prior to common-azimuth migration (Biondi and Palacharla, 1996).

In fairly simple geology, ERM perfectly matches the kinematics of the zero-offset data that would have been recorded with coincident source and receivers at the surface. This means that for ERM to hold, it is necessary that the downgoing path from the source to a point in the subsurface be the same as the upgoing path from the point in the subsurface back to the receiver, Because of this assumption, ERM does not model multiples and prismatic waves. Moreover, the coincident ray-path assumption is often invalid in areas of geological complexity. Therefore, post-stack migration does not produce reliable images in the presence of strong lateral velocity variation.

In areas of complex geology, pre-stack depth migration becomes mandatory not only for imaging purposes but also for velocity estimation. In such areas, migration by wavefield extrapolation has been widely used to produce the final image because it properly handles complex distortions of the wavefields. However, due to the high computational cost, wavefield extrapolation methods are rarely used to estimate the migration velocity model in 3D projects (Fei et al., 2009). Instead Kirchoff migration and ray-based methods are still the industry standards. In addition to the lower cost, ray-based methods are very flexible with respect to strategies for defining the velocity model using selected reflectors (Stork, 1992; Kosloff et al., 1996, 1997; Billette et al., 1997), which is not possible using the conventional migration-velocity analysis with wave-extrapolation methods. But despite their advantages, ray methods do not satisfactorily describe complex wave propagation in the presence of large lateral velocity contrasts. In this case, a more complete description of the wavefield complexities is needed, and therefore we face the challenge of decreasing the cost of migration-velocity analysis by wavefield extrapolation while maintaining its robustness. In addition, it can be usefull to incorporate ray-based strategies, as the horizon-based or the grid-tomography approaches, in the framework of migration-velocity analysis by wavefield extrapolation.

A typical way of decreasing the cost of wavefield extrapolation is to reduce the amount of input data. Data size can be reduced by selecting a smaller number of shots. Figure 2.1 shows pre-stack images computed with the multi-offset imaging condition (Rickett and Sava, 2002), in which the wavefields are spatially cross-correlated. The lags of the spatial cross-correlation are the so-called subsurface offsets. In Figure 2.1a is the migration result of 380 shots 24 m apart, and in Figure 2.1b is the migration result of 23 shots 384 m apart. The shot records are modeled with the one-way wave equation, using a smoothed version of the Marmousi velocity model. The same velocity model is used to migrate the data. The right panel is the zero-subsurface-offset section and the left panel is the subsurface-offset-domain common-image gather (SODCIG) selected at $x = 2760$ m on the right panel. Notice the slanted lines in the SODCIG of Figure 2.1b representing the angles according to which reflectors are illuminated. For the full migration using all the shots, the slanted lines constructively interfere and the energy is focused at zero-subsurface-offset (Figure 2.1a).

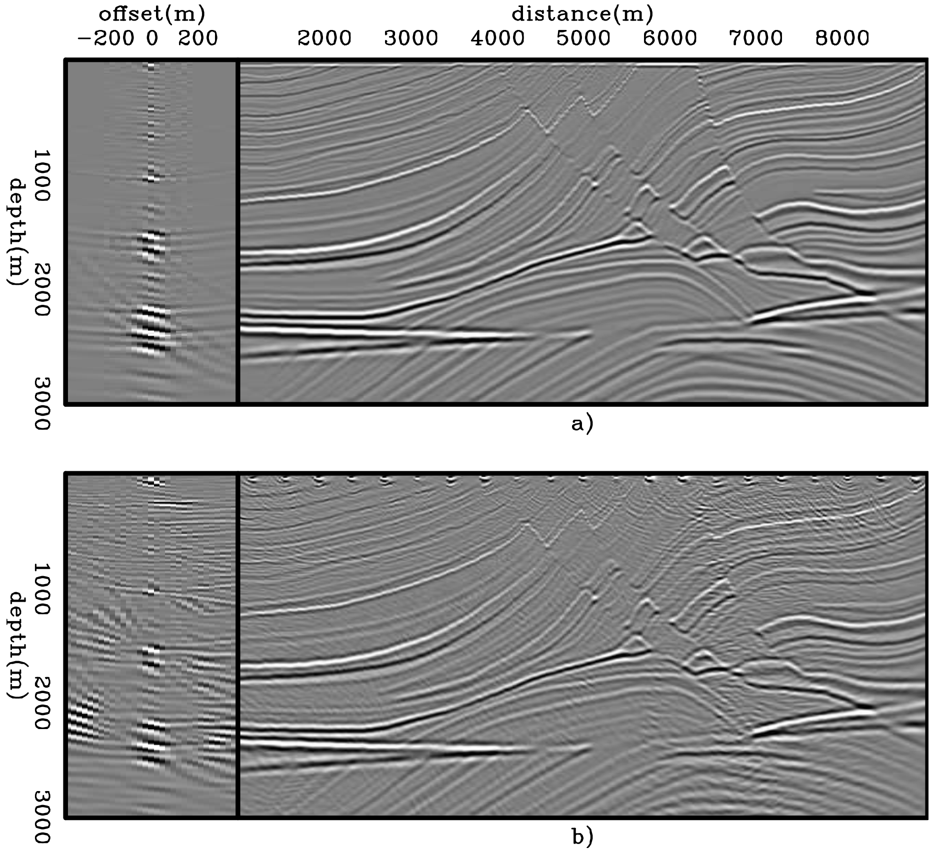

Figure 2.1: a) Shot-profile migration of 380 off-end shots 24 m apart. b) Shot-profile migration of 23 off-end shots 384 m apart. Both images were computed with the correct velocity model. Notice slanted lines present in Figure 2.1b. perm/. perm01

By selecting only a few shots, the migration output shows poor angular coverage. An alternate way of reducing data size is by combining shot-profiles into areal shots based on the linearity of wavefield propagation. Data is multiplied by a comb function and stacked to originate one areal shot. The comb function is shifted until all shots are selected. The original angular coverage is maintained if the period of the sampling function is sufficiently big (Figure 2.2a). However, if many shots are combined, crosstalk is generated, since unrelated shots and receiver wavefields are cross-correlated during imaging (Figure 2.2b). Compare Figures 2.2a and 2.2b with Figure 2.1a. Crosstalk can completely overwhelm the reflectors, and the kinematic information for migration velocity analysis can be lost. This can be clearly seen in the angle-domain common-image gathers (top) and residual moveout panels (bottom) in Figure 2.3a-c. They are selected at the same horizontal position as the SODCIG of Figures 2.1 and 2.2. The left column shows angle gather and residual moveout panel for the full migration, the column in the middle corresponds to the migration of 23 sampled shots, and the right column corresponds to the migration of the combined shots. Whereas the sub-sampling of shots still yields a reasonable residual moveout information, the crosstalk resulting from the combination of many shots destroys the velocity information.

The combination of wavefields is implicit in ERM. When reflectors are allowed to simultaneously explode, linearity of wavefield propagation is evoked to combine wavefields initiated at every point in the subsurface. However, crosstalk is not generated in post-stack migration based on ERM since no cross-correlation of wavefields is performed; rather the imaging condition is a simple summation over frequency, which extracts the image at zero time of wavefield propagation (Claerbout, 1971a). Therefore, it is natural to consider the combination of wavefields in any generalization of ERM.

Combination of wavefields is exploited by the prestack-exploding reflector model (PERM) (Biondi, 2006a) to significantly reduce the data size used in migration velocity updates. Like ERM, PERM uses the concept of exploding-reflectors to generate

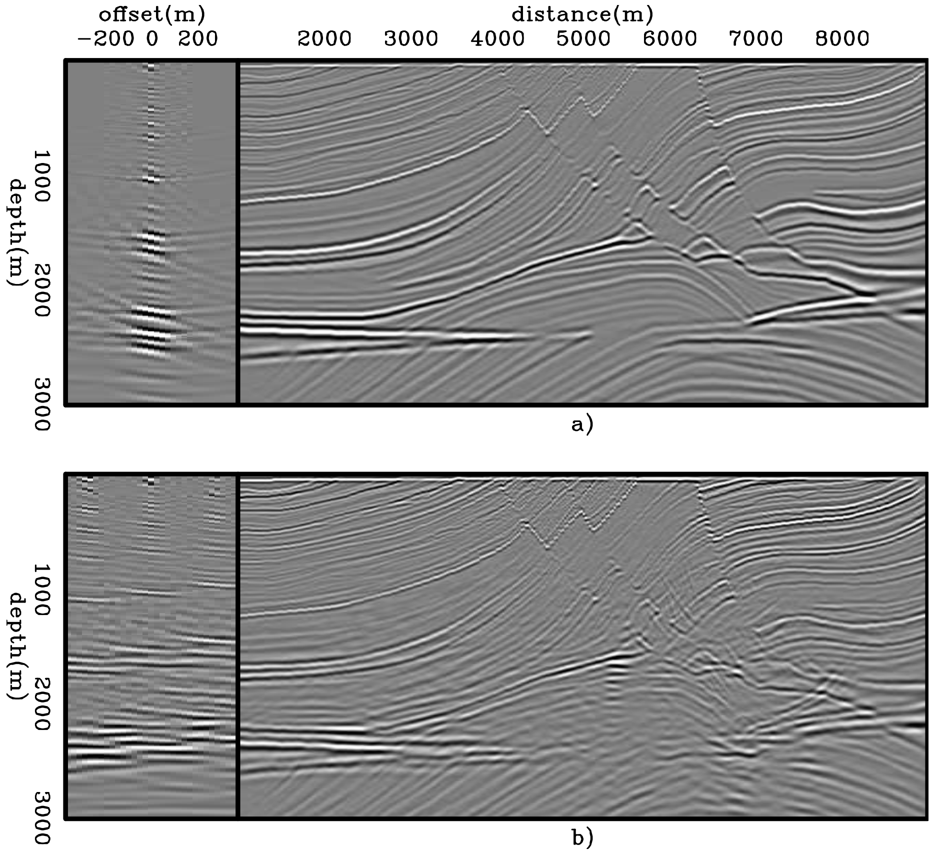

Figure 2.2: a) Shot-profile migration of 95 areal shots resulting from the combination of 4 shot profiles 2256 m apart. b) Shot-profile migration of 23 areal shots resulting from the combination of 16 shot profiles 564 m apart. Both images were computed with the correct velocity model. Notice crosstalk occurring periodically in the SODCIG of Figure 2.2b. perm/. perm02

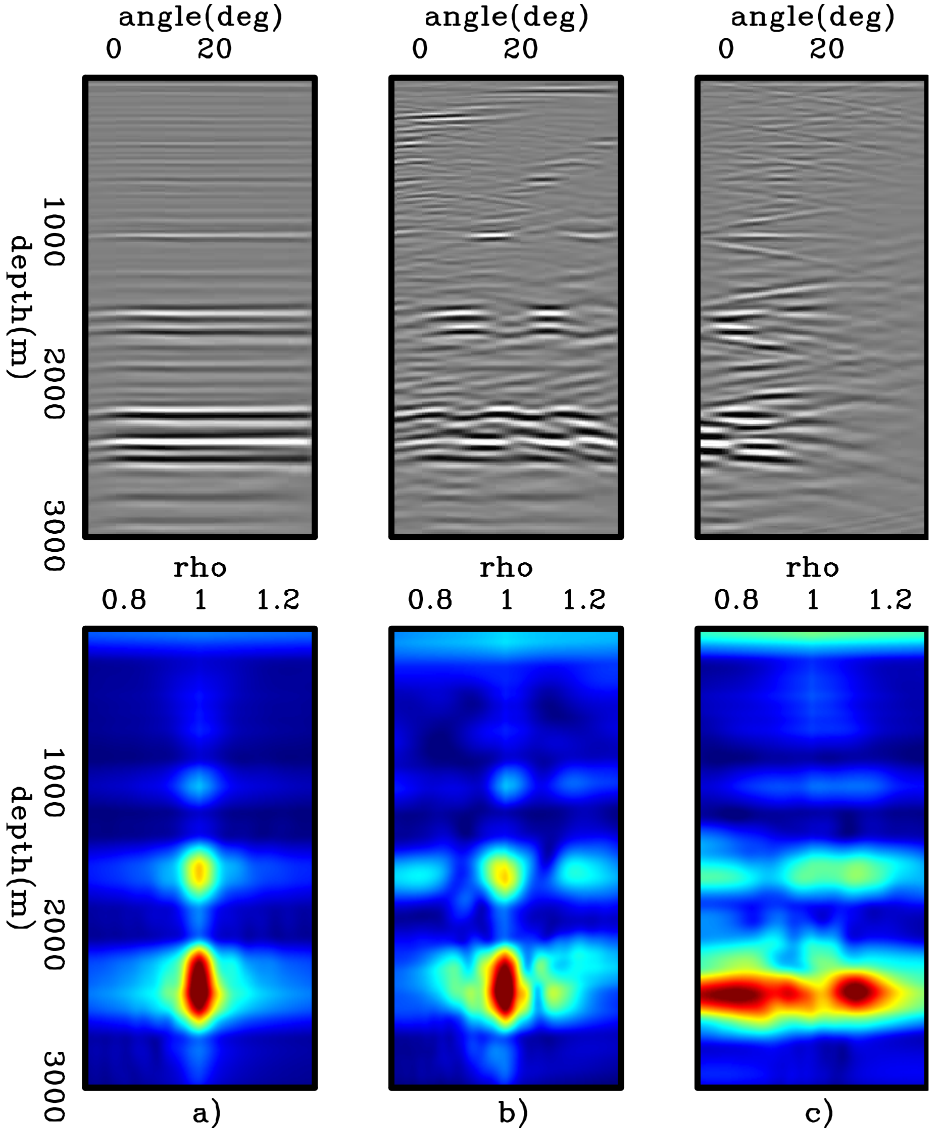

Figure 2.3: Angle-domain common-image gathers (top) and residual moveout panels (bottom). Left: full migration. Middle: migration of 23 sampled shots. Right: migration of the combined shots. Crosstalk resulting from the combination of many shots destroys the velocity information. perm/. perm03

wavefields. However, instead of considering reflectivity only as a function of the spatial coordinates, reflectivity is also parameterized as a function of subsurface-offsets. Its elementary idea is to synthesize data necessary to correctly image a single reflector of an isolated SODCIG, so that migration of PERM data shows the correct kinematics needed for performing velocity updates.

An essential feature of PERM is that it can be used in a target-oriented way, since the modeled data contains all the information necessary to image a predefined region of the subsurface. This concept is used in different methods, such as controlled illumination (Rietveld et al., 1992; Rietveld and Berkhout, 1992) and common-focus point (CFP) (Berkhout, 1997a,b; Thorbecke and Berkhout, 2006).

In this chapter, I introduce and further develop PERM. I will show that data synthesized with PERM has the kinematic information necessary to perform migration velocity analysis. Although, in this thesis, migration velocity analysis is performed using wave-equation tomography, ray-based tomography can also be used in conjunction with PERM data. Before introducing the theory of PERM, I will first describe the exploding-reflector concept of which PERM is a generalization. The usefulness of PERM for migration velocity analysis will be illustrated by comparing areal-shot migration of PERM wavefields with that of shot-profile migration for simple bidimensional models. The extension to a tridimensional (3D) medium is theoretically straightforward but challenging in practice because of computational cost and data handling issues. I will present the general 3D theory and show that under the common-azimuth approximation (Biondi and Palacharla, 1996), PERM drastically decreases data size.

EXPLODING-REFLECTOR MODEL

To describe the exploding-reflector model (ERM) let us analyze the modeling of seismic data under the acoustic approximation. Here, we consider the Born or single-scattering approximation. This consideration leads us to a linear operator whose adjoint is the migration operator.

Let us start with the constant-density acoustic wave equation for a single temporal frequency ω

$$\left(\nabla^2 + \omega^2 s^2(\mathbf{x})\right) P(\mathbf{x}, \omega) = 0, \tag{2.1}$$

where ∇^2 is the Laplacian operator, $s(\mathbf{x})$ is the slowness field, and $P(\mathbf{x}, \omega)$ is the wavefield. Note that $\mathbf{x} = (x, y, z)$ is the vector of spatial coordinates. By introducing reflectivity as $r(\mathbf{x}) = 1 - \frac{s^2(\mathbf{x})}{s_0^2(\mathbf{x})}$, where $s_0(\mathbf{x})$ is a smooth background slowness, equation 2.1 can be written as

$$\left(\nabla^2 + \omega^2 s_0^2(\mathbf{x}, \omega)\right) P(\mathbf{x}, \omega) \approx \omega^2 s_0^2(\mathbf{x}) r(\mathbf{x}) P(\mathbf{x}, \omega). \tag{2.2}$$

The total wavefield $P(\mathbf{x}, \omega)$ can be considered as the sum of an incident background wavefield $P_0(\mathbf{x}, \omega)$ with a perturbed or scattered wavefield $\Delta P(\mathbf{x}, \omega)$. Therefore, we can write

$$\left(\nabla^2 + \omega^2 s_0^2(\mathbf{x})\right) \Delta P(\mathbf{x}, \omega) \approx \omega^2 s_0^2(\mathbf{x}) r(\mathbf{x}) P(\mathbf{x}, \omega), \tag{2.3}$$

given that the background wavefield $P_0(\mathbf{x}, \omega)$ is the solution of equation 2.2 using the background slowness $s_0(\mathbf{x})$. Notice that equation 2.3 is a non-linear relationship between $r(\mathbf{x})$ and $\Delta P(\mathbf{x}, \omega)$. A linear operator can be derived by using Green's function and the Born (weak scattering) approximation. The background Green's function $G_0(\mathbf{x}', \mathbf{x}, \omega)$ is the solution of equation 2.1 using the background slowness in the presence of a point source $\delta(\mathbf{x} - \mathbf{x}')$ at $\mathbf{x}' = (x', y', z')$:

$$\left\{ \begin{array}{l} \left(\nabla^2 + \omega^2 s_0^2(\mathbf{x})\right) G_0(\mathbf{x}', \mathbf{x}, \omega) = 0 \\ G_0(\mathbf{x}', \mathbf{x} = \mathbf{x}', \omega) = \delta(\mathbf{x} - \mathbf{x}') \end{array} \right. . \tag{2.4}$$

Multiplying equation 2.4 by $[\omega^2 s_0^2(\mathbf{x}) r(\mathbf{x}) P(\mathbf{x}, \omega)]$, integrating with respect to $\mathbf{x}'$ over the volume V in the subsurface, and comparing the result with equation 2.3, we see that

$$\Delta P(\mathbf{x},\omega) \approx \int_V \omega^2 s_0^2(\mathbf{x}') r(\mathbf{x}') G_0(\mathbf{x}',\mathbf{x},\omega) P(\mathbf{x}',\omega) d\mathbf{x}'. \tag{2.5}$$

Under the weak scattering assumption, the total wavefield $P(\mathbf{x}',\omega)$ can be approximated by the background wavefield $P_0(\mathbf{x}',\omega)$, and the linear relationship between the scattered wavefield $\Delta P(\mathbf{x},\omega)$ and reflectivity $r(\mathbf{x})$ reads

$$\Delta P(\mathbf{x},\omega) \approx \int_V \omega^2 s_0^2(\mathbf{x}') r(\mathbf{x}') G_0(\mathbf{x}',\mathbf{x},\omega) P_0(\mathbf{x}',\omega) d\mathbf{x}'. \tag{2.6}$$

Using equation 2.6 and assuming that the background slowness field and the reflectivity distribution are known, the scattered wavefields $\Delta P(\mathbf{x_s},\mathbf{x_r},\omega)$ measured by receivers at $\mathbf{x_r} = (x_r, y_r, z_r)$ due to sources located at $\mathbf{x_s} = (x_s, y_s, z_s)$ are

$$\Delta P(\mathbf{x_s},\mathbf{x_r},\omega) \approx \int_V \omega^2 s_0^2(\mathbf{x}) G_0(\mathbf{x_s},\mathbf{x},\omega) r(\mathbf{x}) G_0(\mathbf{x},\mathbf{x_r},\omega) d\mathbf{x}, \tag{2.7}$$

which amounts to convolving the source Green's function with the reflectivity, then with the receiver Green's function, and summing the contributions of all points within V. By using one-way propagators, we downward propagate the source wavefield, convolve it with the reflectivity, and upward propagate this result up to the surface.

Zero-offset data is obtained by selecting from $\Delta P(\mathbf{x_s},\mathbf{x_r},\omega)$ traces with $\mathbf{x_s} = \mathbf{x_r}$,

$$\Delta P(\mathbf{x_s},\omega)|_{x_s=x_r} \approx \int \omega^2 s_0^2(\mathbf{x}) r(\mathbf{x}) \; G_0(\mathbf{x_s},\mathbf{x},\omega)|_{x_s=x_r} G_0(\mathbf{x},\mathbf{x_s},\omega) d\mathbf{x}. \tag{2.8}$$

ERM synthesizes zero-offset data by initiating virtual sources located on the reflectors. The fundamental consideration is that the downgoing and upgoing rays of a zero-offset source and receiver pair follow the same path. The exploding-reflector wavefield is propagated with half of the actual background velocity, and the virtual sources explode with strengths proportional to their reflection coefficients. Assuming that the background slowness and the reflectivity distribution are known, the wavefield generated by the exploding-reflector model $P_{ERM}(\mathbf{x},\omega)$ propagates according to the following one-way wave-equation:

$$\begin{cases} \left(\frac{\partial}{\partial z} + i\sqrt{\omega^2 s^2(\mathbf{x}) - |\mathbf{k}|^2}\right) P_{ERM}(\mathbf{x}, \omega) = r(\mathbf{x}) \\ P_{ERM}(x, y, z = z_{\max}, \omega) = 0 \end{cases} . \tag{2.9}$$

ERM is kinematically correct only if the source and receiver Green's functions are equal for $\mathbf{x_s} = \mathbf{x_r}$ at a point $\mathbf{x}$ in the subsurface. Notice that this condition is unlikely to be fulfilled in the presence of strong lateral velocity variations (Peles et al., 2004). Moreover, ERM does not model multiples and prismatic reflections (Claerbout, 1985).

In equation 2.9, the reflectivity $r(\mathbf{x})$ acts as the initial condition for the wavefield propagation. Notice that a migrated image can replace the reflectivity in the initial condition. Taking into consideration the imaging principle (Claerbout, 1971a) and the computation of pre-stack images by wave-extrapolation methods (Claerbout, 1985; Rickett and Sava, 2002), ERM, as initially formulated, implicitly assumes that all the seismic energy is perfectly focused at zero subsurface offset and that it is sufficient to parameterize the migrated image as a function of only the position vector $\mathbf{x}$. This implies that the slowness field is accurate and illumination of the subsurface is sufficiently good. When this is not the case, the migrated image must be described not only as a function of $\mathbf{x}$, but also as a function of the subsurface offset or aperture angle.

The generalization of ERM proposed in this thesis does not aim at computing pre-stack data *strictu sensu*. Rather, it synthesizes data in the generalized source domain whose migration with wavefield-extrapolation methods enables the computation of a pre-stack image. PERM uses the ERM concept with a poorly focused pre-stack image as the initial condition to propagate wavefields. The modeled data are, potentially, orders of magnitude smaller than the original shot records and contains all necessary kinematic information to update the velocity model using ray-based tomography or, as used in this thesis, wave-equation-based tomography. This characterizes the pre-stack-exploding-reflector model, which will be described in the next section.

PRE-STACK-EXPLODING-REFLECTOR MODEL

Migration-velocity analysis using ray-based methods is very flexible with respect of strategies we can use to optimize the velocity model. For instance, regarding to the intermediate migration of the nonlinear iterations, Kirchhoff migration is the most commonly used. However, images obtained with wave-extrapolation can also be used (Clapp, 2003), which yields more reliable moveout information in areas of geological complexity.

Also, in ray-based migration-velocity analysis reflectors must be identified. That is because traveltime perturbations can be caused by both velocity perturbations or perturbations in the reflector position. Two distinct approaches arise from the identification of reflectors: the horizon-based tomography (Kosloff et al., 1996) and the grid tomography (Kosloff et al., 1997; Billette et al., 1997). The horizon-based tomography uses representative reflectors, which typically have good signal-to-noise ratio and characterize the main velocity changes, to define the macro-velocity structure. Grid tomography also selects coherent reflectors but without the need of being laterally continuous. Contrasting with the horizon-based approach, grid tomography uses several reflector segments to estimate the velocity perturbation. At the later stages of migration-velocity analysis, grid tomography can also be used to refine a velocity model obtained with horizon-based tomography.

Migration-velocity analysis using wavefield-extrapolation methods does not have the same flexibility of its ray-based counterpart. This is partly because ray-based methods are a more mature technology. A characteristic of wave-extrapolation methods is the use of all events in the recorded wavefield to compute velocity perturbations. Ideally, the events should be consistent with the physics of wavefield-extrapolation method. When this is not the case, a preprocessing step is necessary to attenuate the events or the attenuation must be incorporated into the objective function (Mulder and ten Kroode, 2002). These authors show how multiples can strongly bias the velocity updates. Another strategy is to select only representative and coherent events for migration-velocity analysis using wavefield-extrapolation methods. However, differently from the ray-based migration-velocity analysis in which events are easily identified in the model space, event identification for migration-velocity analysis based on wavefield-extrapolation should be done in the data domain, which is a very difficult task.

The use of PERM wavefields can enable us to incorporate ray-based strategies in wavefield-extrapolation methods. As we will see in this chapter, reflectors must be identified to model PERM wavefields. Hence, a horizon-based strategy is easily incorporated in migration-velocity analysis by wavefield-extrapolation. Moreover, due to the localized nature of the initial conditions for modeling PERM wavefields, migration of a single pair of PERM wavefields produces an image with a fairly good approximation of the correct kinematics. Therefore, using PERM wavefields potentially enable us to apply a grid-based strategy in migration-velocity analysis by wavefield-extrapolation.

In addition to allowing more flexibility in migration-velocity analysis by wavefield-extrapolation, the size of PERM data set can be orders of magnitude smaller than the original data set enabling faster velocity updates.

The fundamental idea of PERM is to model data that describes the correct kinematics of an isolated SODCIG. Many shot records contribute to form the image at a point in the subsurface. Therefore, to model data using conventional one-way modeling, we would perform several modeling experiments consisting of downward continuing the source wavefield initiated by point sources at the surface, convolving the propagated source wavefield with the SODCIG, and upward continuing the convolution result up to the surface. As we do not know beforehand which shots contribute to forming the image at a point in the subsurface, we would have to model every shot originally present in the original dataset.

Ideally, instead of performing many modeling experiments, we would like to synthesize a small amount of data with the condition that migration has the same kinematics as the initial SODCIG. This can be achieved by using a strategy similar to

ERM. To compute SODCIGs using the new modeled data, we need to synthesize source and receiver wavefields.

The modeling of PERM source D_P and receiver U_P wavefields can be carried out by any wavefield-continuation scheme. Here, we use the following one-way wave equations:

$$\left\{ \begin{array}{l} \left(\frac{\partial}{\partial z} - i\sqrt{\omega^2 s_0^2(\mathbf{x}) - |\mathbf{k}|^2}\right) D_P(\mathbf{x},\omega;\mathbf{x_m}) = I_D(\mathbf{x_m},\mathbf{h}) \\ D_P(x,y,z=z_{\max},\omega;\mathbf{x_m}) = 0 \end{array} \right. , \tag{2.10}$$

and

$$\left\{ \begin{array}{l} \left(\frac{\partial}{\partial z} + i\sqrt{\omega^2 s_0^2(\mathbf{x}) - |\mathbf{k}|^2}\right) U_P(\mathbf{x},\omega;\mathbf{x_m}) = I_U(\mathbf{x_m},\mathbf{h}) \\ U_P(x,y,z=z_{\max},\omega;\mathbf{x_m}) = 0 \end{array} \right. , \tag{2.11}$$

where $I_D(\mathbf{x_m},\mathbf{h})$ and $I_U(\mathbf{x_m},\mathbf{h})$ is the isolated SODCIG at the horizontal location $\mathbf{x_m}$ for a single reflector, suitable for the initial conditions for the source and receiver wavefields, respectively. The subsurface-offset $\mathbf{h}$ can be parameterized as $\mathbf{h} = (h_x, h_y, h_z)$. In this thesis, when describing 2D problems $\mathbf{h} = (h_x)$, and for the 3D case, $\mathbf{h} = (h_x, h_y)$. We do not consider the computation of the vertical subsurface offset h_z as introduced by Biondi and Shan (2002). The initial conditions are obtained by rotating the original unfocused SODCIGs according to the apparent geological dip of the reflector. For dipping reflectors, this rotation maintains the velocity information needed for migration velocity analysis. The rotation of SODCIGs will be described later in this chapter. If the initial condition has energy focused at the zero-subsurface offset; and if no pre-stack information is available, the pre-stack image can be parameterized only by its spatial coordinates, and PERM is equivalent to ERM.

Let us now illustrate the generation of PERM data synthesized from a single SODCIG. We start with a pre-stack image computed with shot-profile migration of 401 split-spread shots at every 10 m and maximum offset of 2250 m, using a 10% lower velocity (Figure 2.4). The model consists of one reflector at 750 m depth embedded in a medium with a constant velocity of 1000 m/s. The pre-stack image has 81 subsurface offsets ranging from -400 m to 400 m. Notice the poor focusing of energy around the zero-subsurface offset due to inaccurate velocity.

The SODCIG at $x_m = 0$ m was used as the initial condition for modeling the corresponding pair of PERM source and receiver wavefields using the same inaccurate velocity. The wavefields are upward propagated according to equations 2.10 and 2.11. The PERM data is shown in Figure 2.5. Notice that the receiver wavefield (Figure 2.5a) occurs at positive times, while the source wavefield (Figure 2.5b) occurs at negative times. According to the imaging principle (Claerbout, 1971a), reflectors explode at time zero. This is the time at which the source wavefield impinges on the reflector. Because the receiver wavefield exists after the source wavefield has reached the reflector, the areal receiver data $U_P(x, y, z = 0, \omega; \mathbf{x_m})$ is upward propagated forward in time. For the same reason, the areal source data $D_P(x, y, z = 0, \omega; \mathbf{x_m})$ is upward propagated backward in time.

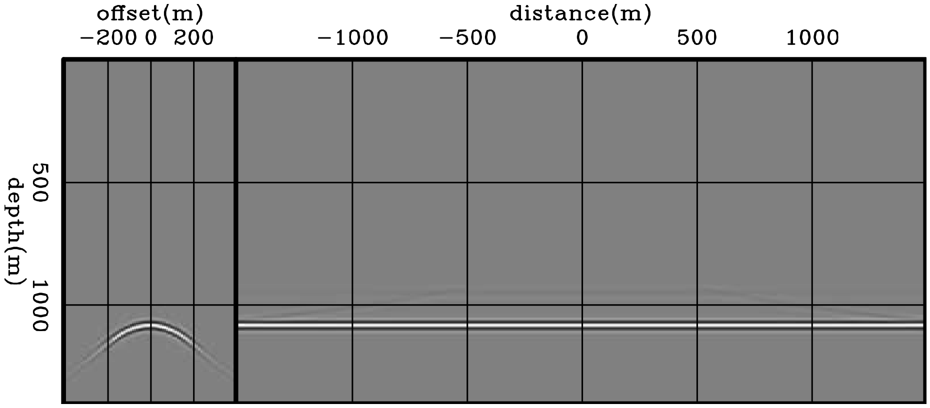

Figure 2.4: Shot-profile migration of 401 split-spread shots 10 m apart with a 10% slower velocity. The model consists of a horizontal reflector embedded in constant velocity of 1000 m/s. perm/. refpl01

Areal-shot migration of data from Figure 2.5 with the same inaccurate velocity shows kinematics at near subsurface offsets similar to those of the original shot-profile migration (compare Figures 2.6 and 2.4). However, for farther subsurface offsets energy is not adequately imaged. This can be easily explained by analyzing how the

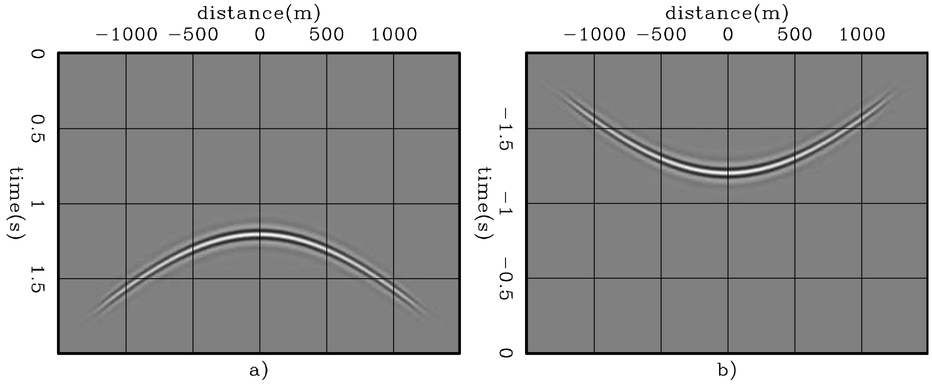

Figure 2.5: Data synthesized by PERM having as the initial condition the SODCIG at $x_m = 0$ m. a) The receiver wavefield. b) The source wavefield. perm/. refpl02

image $I_P(\mathbf{x}, \mathbf{h}; \mathbf{x_m})$ is formed when applying the multi-offset imaging condition to the downward propagated PERM wavefields modeled from a SODCIG located at $\mathbf{x_m}$. For one particular frequency, it reads

$$I_P(\mathbf{x}, \mathbf{h}; \mathbf{x_m}) = D_P^*(\mathbf{x} - \mathbf{h}; \mathbf{x_m}) U_P(\mathbf{x} + \mathbf{h}; \mathbf{x_m}), \tag{2.12}$$

where '*' stands for the complex conjugate. Notice that the maximum absolute distance at which wavefields still correlate is $|2h_{max}|$ for symmetric SODCIGs with respect to subsurface offset or, more generally, twice the subsurface offset range. Therefore, to ensure that the areal-shot migrated image has kinematics at all subsurface offsets similar to those in the original isolated SODCIG, we need to model PERM data from a set of SODCIGs within that neighborhood around the central SODCIG.

The areal-shot migration of PERM data synthesized by isolated SODCIGs within the interval $(-2max\,|h_x|\,, 2max\,|h_x|)$ is shown in Figure 2.7. By using more data, energy is adequately imaged at far subsurface offsets (compare with Figures 2.4 and 2.6). To further understand the behavior of the areal-shot migrated image, let us examine the reflection angle-domain common-image gathers (ADCIGs) (Sava and Fomel, 2003). ADCIGs computed from the SODCIGs of Figures 2.4, 2.6 and 2.7 attest to the more accurate imaging when migrating data modeled from the set of SODCIGs

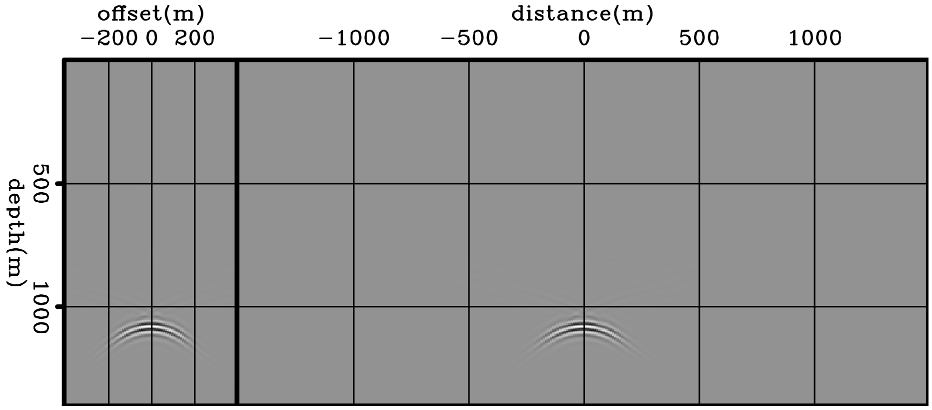

Figure 2.6: Areal-shot migration of PERM data shown in Figure 2.5 with a 10% slower velocity. By comparing with Figure 2.4 we see that far subsurface-offsets are not properly imaged. perm/. refpl03

around $\mathbf{x_m}$ (Figure 2.8). Although the ADCIG from the the image computed with a single pair of PERM data (Figure 2.8b) shows reasonable kinematics, the amplitude of wide-aperture angles is weaker than that of the original ADCIG (Figure 2.8a). Notice that the amplitude behavior of the ADCIG computed with several areal shots from SODCIGs within the neighborhood of $\mathbf{x_m}$ (Figure 2.8c) better matches that of the original isolated SODCIG.

If, instead of using the incorrect migration velocity, we input the correct migration velocity to the areal-shot migration, energy nicely focuses at zero subsurface offset (Figure 2.9). This property will be used to perform migration velocity updates in Chapter 3.

In the previous examples we saw that PERM data contains all the kinematic information needed to perform migration velocity analysis and the image computed with PERM wavefields resembles the original shot-profile migrated image. However, by carefully examining these images we can see that the former has stronger side lobes due to the squaring of the wavelet, which is mathematically explained by the modeling and migration of PERM wavefields initiated at a single SODCIG selected at $\mathbf{x_m}$. For one particular frequency, and considering, for simplicity, a plane reflector

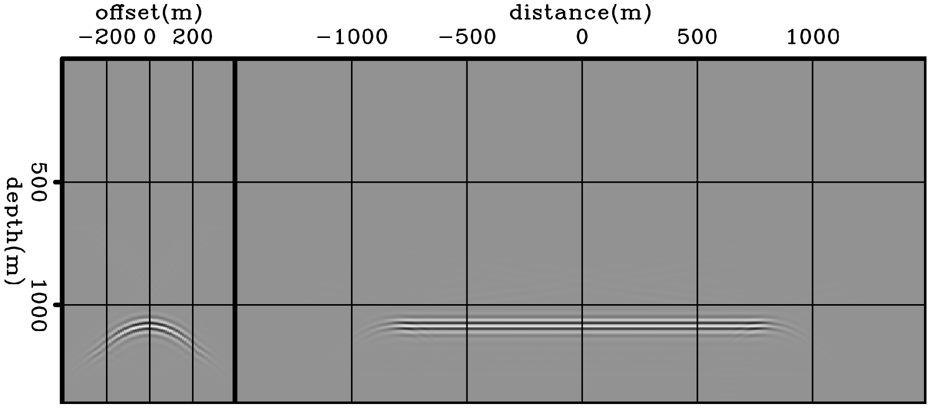

Figure 2.7: Areal-shot migration of PERM data having a set of isolated SODCIGs around $x_m = 0$ m as the initial condition with a 10% slower velocity. By comparing with Figure 2.4 we see that the kinematics of far subsurface-offsets is properly recovered. perm/. refpl04

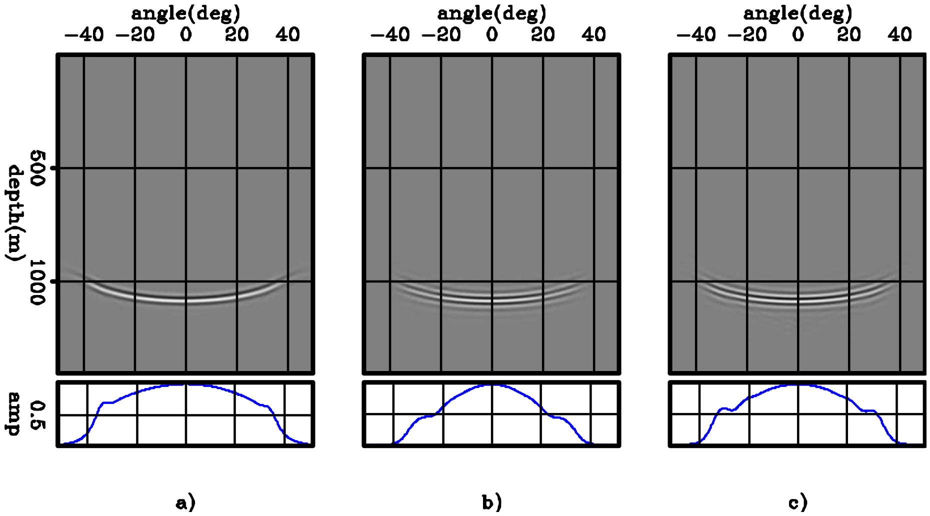

Figure 2.8: ADCIGs selected at $x_m = 0$ m. a) Computed from the shot-profile migration; b) computed from the areal-shot migration of one pair of PERM data modeled from the SODCIG at $x_m = 0$ m; and c) computed from the areal-shot migration of pairs of PERM data modeled from a set of SODCIGs around $x_m = 0$ m. Notice that although the kinematics are similar, the amplitudes in c) better match those of a). perm/. refpl05

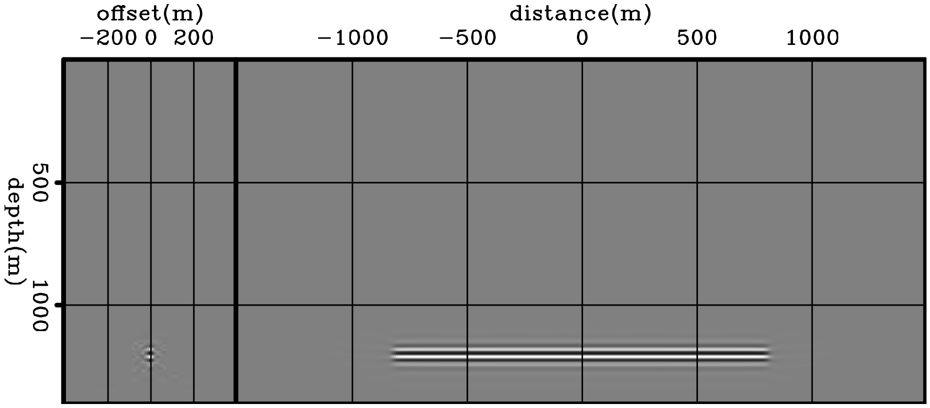

Figure 2.9: Areal-shot migration of PERM data having a set of isolated SODCIGs around $x_m = 0$ m as the initial condition with the correct velocity. Energy nicely focuses at zero-subsurface offset. perm/. refpl06

so that the initial conditions are the same for modeling source D_P and receiver U_P wavefields, PERM modeling can be described by

$$D_P(\boldsymbol{\xi};\mathbf{x_m}) = \sum_{\mathbf{x}}\sum_{\mathbf{h}} G_0(\boldsymbol{\xi},\mathbf{x}-\mathbf{h})I(\mathbf{x_m},\mathbf{h}), \tag{2.13}$$

and

$$U_P(\boldsymbol{\xi};\mathbf{x_m}) = \sum_{\mathbf{x}}\sum_{\mathbf{h}} G_0(\boldsymbol{\xi},\mathbf{x}+\mathbf{h})I(\mathbf{x_m},\mathbf{h}). \tag{2.14}$$

The pre-stack image is injected to the modeling by projecting the subsurface offsets $\mathbf{h}$ on the spatial axis $\mathbf{x}$. The Green's function G_0 upward propagates the wavefields from the subsurface (represented by the the coordinates $\mathbf{x}$) up to the depth level where the wavefields are collected (represented by the coordinates $\boldsymbol{\xi}$). Its subscript denotes that the wavefield propagation is performed with the background slowness $s_0(\mathbf{x})$ used to migrate the original shot-profiles.

The wavefields are recursively downward propagated in depth according to

$$D_P(\mathbf{x};\mathbf{x_m}) = \sum_{\boldsymbol{\xi}} G_1^*(\boldsymbol{\xi},\mathbf{x}) D_P(\boldsymbol{\xi};\mathbf{x_m}), \tag{2.15}$$

and

$$U_P(\mathbf{x};\mathbf{x_m}) = \sum_{\boldsymbol{\xi}} G_1^*(\boldsymbol{\xi},\mathbf{x}) U_P(\boldsymbol{\xi};\mathbf{x_m}). \tag{2.16}$$

Note that in equations 2.15 and 2.16 the subscript of the Green's function indicates the use of a different migration velocity.

The lateral shifts of the wavefields for the multi-offset imaging condition are represented by

$$D_P(\mathbf{x}-\mathbf{h};\mathbf{x_m}) = \sum_{\boldsymbol{\xi}} G_1^*(\boldsymbol{\xi},\mathbf{x}-\mathbf{h}) \sum_{\mathbf{x}'}\sum_{\mathbf{h}'} G_0(\boldsymbol{\xi},\mathbf{x}'-\mathbf{h}') I(\mathbf{x_m},\mathbf{h}'), \tag{2.17}$$

and

$$U_P(\mathbf{x}+\mathbf{h};\mathbf{x_m}) = \sum_{\boldsymbol{\xi}} G_1^*(\boldsymbol{\xi},\mathbf{x}+\mathbf{h}) \sum_{\mathbf{x}'}\sum_{\mathbf{h}'} G_0(\boldsymbol{\xi},\mathbf{x}'+\mathbf{h}') I(\mathbf{x_m},\mathbf{h}'). \tag{2.18}$$

The PERM image is obtained by inserting equations 2.17 and 2.18 into equation 2.12

$$\begin{aligned} I_P(\mathbf{x},\mathbf{h};\mathbf{x_m}) &= \sum_{\boldsymbol{\xi}}\sum_{\mathbf{x}'}\sum_{\mathbf{h}'} G_0(\boldsymbol{\xi},\mathbf{x}'-\mathbf{h}') G_1^*(\boldsymbol{\xi},\mathbf{x}-\mathbf{h}) I(\mathbf{x_m},\mathbf{h}') \\ &\times \sum_{\boldsymbol{\xi}}\sum_{\mathbf{x}'}\sum_{\mathbf{h}'} G_1^*(\boldsymbol{\xi},\mathbf{x}+\mathbf{h}) G_0(\boldsymbol{\xi},\mathbf{x}'+\mathbf{h}') I(\mathbf{x_m},\mathbf{h}'), \end{aligned} \tag{2.19}$$

which finally gives

$$\begin{aligned} I_P(\mathbf{x},\mathbf{h};\mathbf{x_m}) &= \sum_{\boldsymbol{\xi}'}\sum_{\mathbf{x}'}\sum_{\mathbf{h}'}\sum_{\boldsymbol{\xi}''}\sum_{\mathbf{x}''}\sum_{\mathbf{h}''} G_0(\boldsymbol{\xi}',\mathbf{x}'-\mathbf{h}') G_1^*(\boldsymbol{\xi}',\mathbf{x}-\mathbf{h}) \\ &\times G_1^*(\boldsymbol{\xi}'',\mathbf{x}+\mathbf{h}) G_0(\boldsymbol{\xi}'',\mathbf{x}''+\mathbf{h}'') I(\mathbf{x_m},\mathbf{h}') I(\mathbf{x_m},\mathbf{h}''), \end{aligned} \tag{2.20}$$

From equation 2.20, we can see that, if the velocity used in the downward propagation is the same as that in the upward propagation, the pre-stack image I_P at x_m is approximately a squared version of the original image. This means that in addition to the stronger side lobes, reflectors in the PERM image will always have positive polarity and the amplitude variation in the PERM image will be more pronounced than that in the original image. The last amplitude effect can be mitigated by taking the square root of the absolute value of initial conditions while keeping is polarity.

Migration of PERM wavefields generated at all SODCIGs is obtained by summing over all $\mathbf{x_m}$

$$\begin{aligned} I_P(\mathbf{x},\mathbf{h}) &= \sum_{\mathbf{x_m}}\sum_{\boldsymbol{\xi}'}\sum_{\mathbf{x}'}\sum_{\mathbf{h}'}\sum_{\boldsymbol{\xi}''}\sum_{\mathbf{x}''}\sum_{\mathbf{h}''} G_0(\boldsymbol{\xi}',\mathbf{x}'-\mathbf{h}')G_1^*(\boldsymbol{\xi}',\mathbf{x}-\mathbf{h}) \\ &\times \; G_1^*(\boldsymbol{\xi}'',\mathbf{x}+\mathbf{h})G_0(\boldsymbol{\xi}'',\mathbf{x}''+\mathbf{h}'')I(\mathbf{x_m},\mathbf{h}')I(\mathbf{x_m},\mathbf{h}''). \end{aligned} \tag{2.21}$$

For the simple case of a horizontal reflector in a constant velocity medium, we have shown that migration of PERM data produces images with the same kinematics as the shot profile migration. Now, we introduce a dipping reflector in the same constant background velocity medium. In the presence of a non-zero geological dip, a pre-processing of the initial conditions is necessary to obtain correct kinematics. This pre-processing step is represented by a rotation of the pre-stack image according to the apparent geological dip.

Dip-independent initial conditions

Shot-profile and areal-shot migrations by wavefield extrapolation compute pre-stack images by means of the multi-offset imaging condition (Rickett and Sava, 2002), in which source and receiver wavefields are laterally shifted prior to time correlation. However, the shift between wavefields might not be restricted to the horizontal direction. For instance, vertical shifts of the wavefields produce the vertical-subsurface-offset gathers, which provide reliable velocity information in the presence of steep dips (Biondi and Shan, 2002).

Ideally, wavefields should be shifted along the geological dip direction. According to Biondi and Symes (2004), SODCIGs computed this way do not suffer from image-point dispersal in the presence of dip and inaccuracies in the migration velocity. The image-point dispersal causes events with different reflection angles from the same reflection point in the subsurface to be imaged at different locations.

The image-point dispersal in 2D is illustrated in Figure 2.10 for the case of migrating with a velocity slower (Figure 2.10a) and faster (Figure 2.10b) than the true velocity. For simplicity, let us consider constant velocity in the vicinity of the image point, so source and receiver rays are straight.

When the migration velocity is too low, the reflector is imaged at a shallower depth. The image point computed with horizontal shifts of the wavefields I_{hx} is shifted down-dip with respect to the image point computed with shifts along the apparent geological dip I_{hg}. The geological dip is called apparent because of the migration velocity error. The point I is where source and receiver rays cross at an angle that is twice the apparent reflection angle γ. Source and receiver rays cross deeper than the image points, causing events to curve downward in the SODCIG.

When the migration velocity is too high, the reflector is imaged at a greater depth. The image point I_{hx} is shifted up-dip with respect to I_{hg}. Source and receiver rays cross shallower than the image points, causing events to curve upward in the SODCIG.

Generating SODCIGs along the geological-dip direction overcomes the problem of the image-point dispersal. However, it is computationally demanding since, wavefields must be stored at various depths. Furthermore, accurate dip information is difficult to obtain, especially when events cross because of velocity inaccuracy.

Biondi and Symes (2004) point out that, at least to the first order, the reflection-angle domain is immune to image-point dispersal. This is because the SODCIG to ADCIG transformation shifts events to the line connecting I and I_{hg} in Figure 2.10 at the same image point shared by all the reflection angles.

In the presence of dip, to accurately model PERM data it is crucial that the initial conditions are free of image-point dispersal, so that all the energy of a point in the

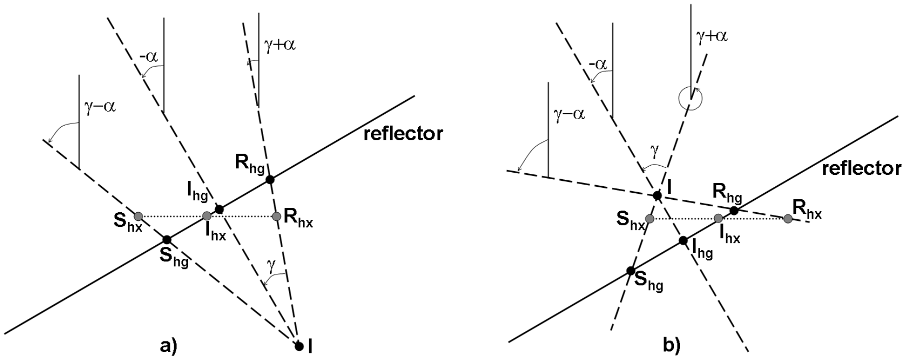

Figure 2.10: Geometry for the computation of SODCIGs. Source, receiver and image points are labeled with S, R and I, respectively. The subscript hx corresponds to subsurface offsets computed with horizontal shift. The subscript hg corresponds to subsurface offsets computed by shifting along the apparent geological dip α. a) Underestimated velocity, and b) overestimated velocity. Modified from Biondi and Symes (2004). perm/. pdisp

subsurface is contained by the corresponding SODCIG injected into the modeling. Since SODCIGs along the geological dip are not easily computed, can we pre-process the SODCIGs computed with horizontal shifts of the wavefields such that they are transformed into a good approximation of the SODCIGs along the geological dip?

To answer this question, let us first examine the angle relationships in Figure 2.10. The angles $\gamma + \alpha$ and $\gamma - \alpha$ are the source and receiver ray angles, respectively. They are the propagation directions of the wavefields locally at the image point. In 2D, α and γ are related to slopes in the pre-stack image according to

$$\tan \alpha = -\frac{dz_m}{dx_m} \tag{2.22}$$

and

$$\tan \gamma = -\frac{dz}{dh_x}, \tag{2.23}$$

where the subscript m in equation 2.22 refers to the local nature of the relationship.

The solutions of the differential equations 2.22 and 2.23 define slant-stack paths, which allow us to transform the 2D pre-stack image $I(x, z, h_x)$ into $I(x, z, \alpha, \gamma)$ by angle decomposition according to the following integrals:

$$I(x, z, \alpha, \gamma) = \int_{x_{m_i}}^{x_{m_f}} \int_{-h_x}^{h_x} W(x_m - x) \frac{dI(x, z, h_x)}{dz} dx_m dh_x \bigg|_{\substack{z=z_h+h_x \tan\gamma \\ z=z_m+x_m \tan\alpha}} \tag{2.24}$$

where the derivative with respect to z is performed to recover the correct phase. The local window $W(x_m - x)$ is used in the local slant-stack integral on x_m, being defined as

$$\begin{cases} 1, x_{m_i} \leq x \leq x_{m_f}, \\ 0, elsewhere \end{cases}$$

where $x_{m_i} = x_m - \frac{x_w}{2}$ and $x_{m_f} = x_m + \frac{x_w}{2}$, with x_w being the width of the local window.

Again, using simple trigonometry, we have

$$\tan(\gamma + \alpha) = \frac{\tan\gamma + \tan\alpha}{1 - \tan\gamma \tan\alpha}, \tag{2.25}$$

$$\tan(\gamma - \alpha) = \frac{\tan\gamma - \tan\alpha}{1 + \tan\gamma \tan\alpha}. \tag{2.26}$$

To align the initial conditions with the geological dip, we need to change the dip along the subsurface-offset axis according to the apparent geological dip, yielding the new subsurface offset $\widetilde{h_{x_s}}$ and $\widetilde{h_{x_r}}$ for the initial conditions of the modeling of source and receiver wavefield, respectively. This is accomplished by solving the following differential equations:

$$\tan(\gamma + \alpha) = -\frac{dz}{d\widetilde{h_{x_s}}}, \tag{2.27}$$

$$\tan(\gamma - \alpha) = \frac{dz}{d\widetilde{h_{x_r}}}. \tag{2.28}$$

The solutions of equations 2.27 and 2.28 define new slant-stack operations which, in combination with equations 2.25 and 2.26, reduce the dimensionality of the decomposed pre-stack image (equation 2.24) by transforming $I(x, z, \alpha, \gamma)$ into $I_D(x, z, \widetilde{h_{x_s}})$ and $I_U(x, z, \widetilde{h_{x_r}})$.

In 3D, the cross-line offsets also must be rotated according to the apparent geological dip in the cross-line direction in addition to the in-line rotation. By assuming that source and receiver rays are coplanar such that they cross, the 3D transformation to the reflection-angle domain (Biondi and Tisserant, 2004) is given by

$$k_{h_x} = -k_z \sec \alpha_{y'} \tan \gamma, \tag{2.29}$$

and

$$k_{h_y} = -k_{y'} \tan \gamma \tan \alpha_{x'}, \tag{2.30}$$

where $\alpha_{x'}$ and $\alpha_{y'}$ are the apparent geological dips in the in-line and cross-line directions, respectively. Notice that the 3D transformation is dependent on the apparent geological dip in contrast with the 2D case. In the spatial domain, equations 2.29 and 2.30 define slant-stack transformations along the paths

$$z = z_{h_x} + \frac{h_x}{\cos \alpha_{y'}} \tan \gamma, \tag{2.31}$$

and

$$z = z_{h_y} + h_y \tan \alpha_{x'} \tan \alpha_{y'} \tan \gamma, \tag{2.32}$$

respectively. The term $\cos \alpha_{y'}$ in equation 2.31 stretches the inline-subsurface-offset axis, while the combination of terms $\tan \alpha_{x'}$ and $\tan \alpha_{y'}$ in equation 2.32 can stretch or shrink the crossline-subsurface-offset axis.

Under the common-azimuth approximation, the 3D rotation is similar to the 2D rotation (equation 2.24) except for the subsurface-offset stretching factor (equation 2.31). Later in this chapter, we will see areal-shot migration results of 3D-PERM wavefields modeled from the initial conditions computed with and without considering the stretching term.

To illustrate the generation of dip-independent initial conditions, 801 split-spread shots 10 m apart with maximum offset of 3250 m were modeled with a velocity of 1000 m/s and migrated with velocity underestimated by 10% (Figure 2.11). The model has a 20° dipping reflector and a horizontal reflector at a depth of 2500 m. The SODCIG located at 0 m was used as the initial condition for the modeling of PERM data without applying the pre-processing described above. Since PERM models one event of one isolated SODCIG, the dipping reflector and the horizontal reflector originate two different pairs of PERM wavefields. This means that reflectors used in the modeling need to be interpreted in the pre-stack volume. The pair of source and receiver wavefields for the dipping reflector are shown in Figure 2.12.

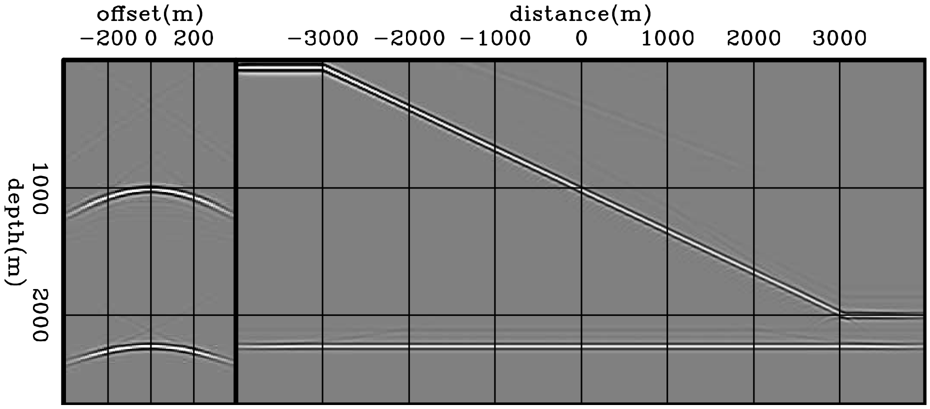

Figure 2.11: Shot-profile migration of 801 split-spread shots 10 m apart with velocity 10% slower than the true velocity. The model is represented by a 20° dipping reflector and a horizontal reflector at a depth of 2500 m embedded in a medium with a constant velocity of 1000 m/s. perm/. dip01

Since the modeling of a single non-rotated SODCIG carries no dip information, migration of the corresponding PERM data using the correct velocity does not shift

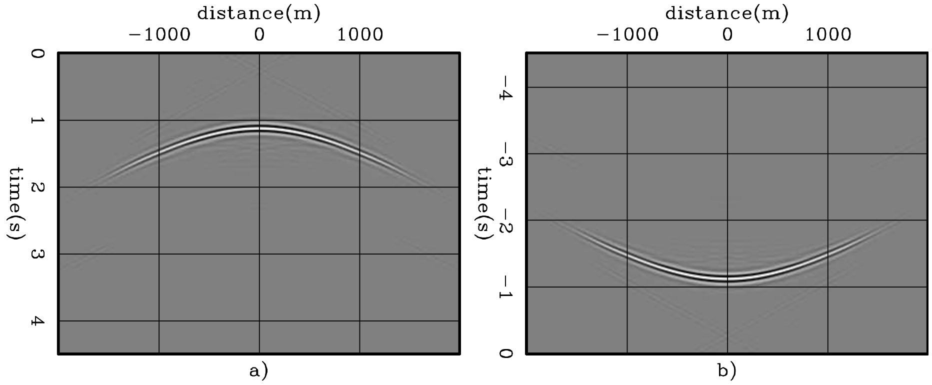

Figure 2.12: Data synthesized by PERM having as the initial condition the dipping reflector in the SODCIG at $x_m = 0$ m. a) The receiver wavefield. b) The source wavefield. perm/. dip02

events laterally, as can be seen in Figure 2.13. As expected, the horizontal reflector focuses at zero-subsurface offset. However, notice how the dipping reflector still presents a residual curvature. Migration of PERM data from SODCIGs within a neighborhood around $x_m = 0$ m is shown in Figure 2.14. Again, the residual curvature is present and any migration velocity analysis using this result will lead to incorrect velocity updates. This residual curvature is a result of not having corrected the image-point dispersal. Unless stated, SODCIGs in the figures are selected at $x = 0$ m.

The rotation was applied to the image in Figure 2.11, and the new PERM data was modeled using the initial conditions shown in Figure 2.15. Notice that the initial condition for modeling the source wavefield (Figure 2.15a) and the initial condition for modeling the receiver wavefield (Figure 2.15b) have the dipping event oriented in opposite directions in the SODCIG. The rotation changes neither the horizontal reflector nor the-zero subsurface offset, as can be seen in the right panels.

The source and receiver wavefields for the dipping reflector after rotation are shown in Figure 2.16. The events in Figures 2.16a and 2.16b are shown in the same areal shot for illustration only. Actually, they pertain to different areal shots since

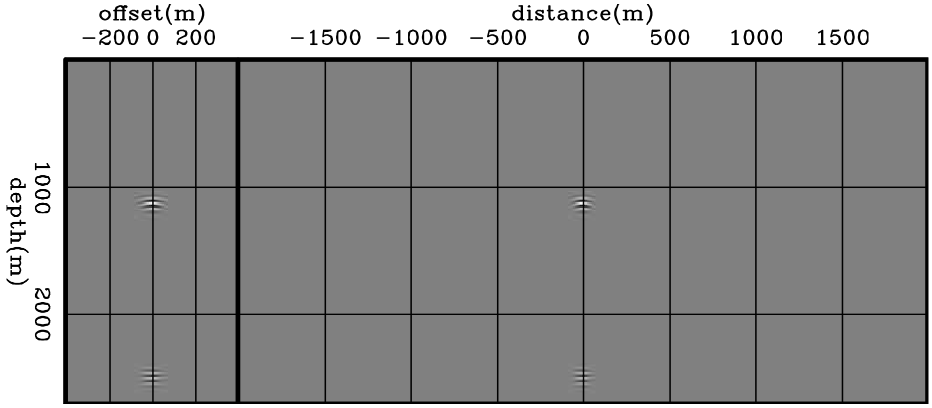

Figure 2.13: Areal-shot migration of PERM data shown in Figure 2.12 using the correct velocity. The horizontal reflector is focused at zero-subsurface offset, but the dipping reflector shows residual curvature. perm/. dip03

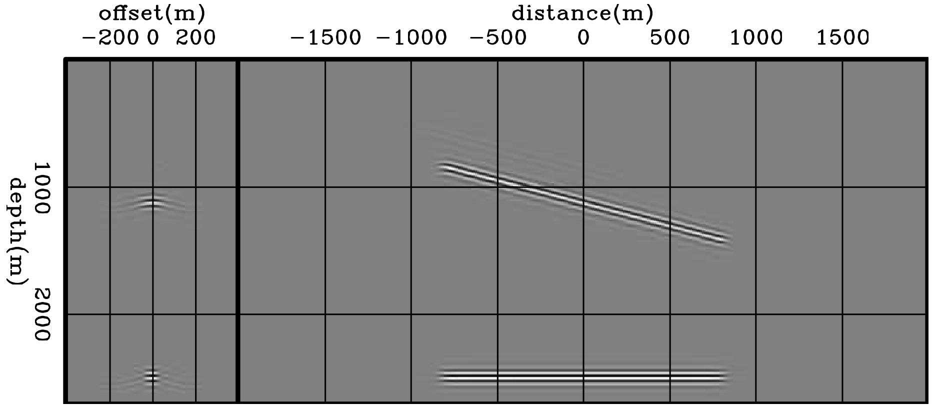

Figure 2.14: Areal-shot migration with correct velocity of PERM data having a set of isolated SODCIGs around $x_m = 0$ m as the initial conditions. As in Figure 2.13, the horizontal reflector is focused at zero-subsurface offset, but the dipping reflector shows residual curvature. perm/. dip04

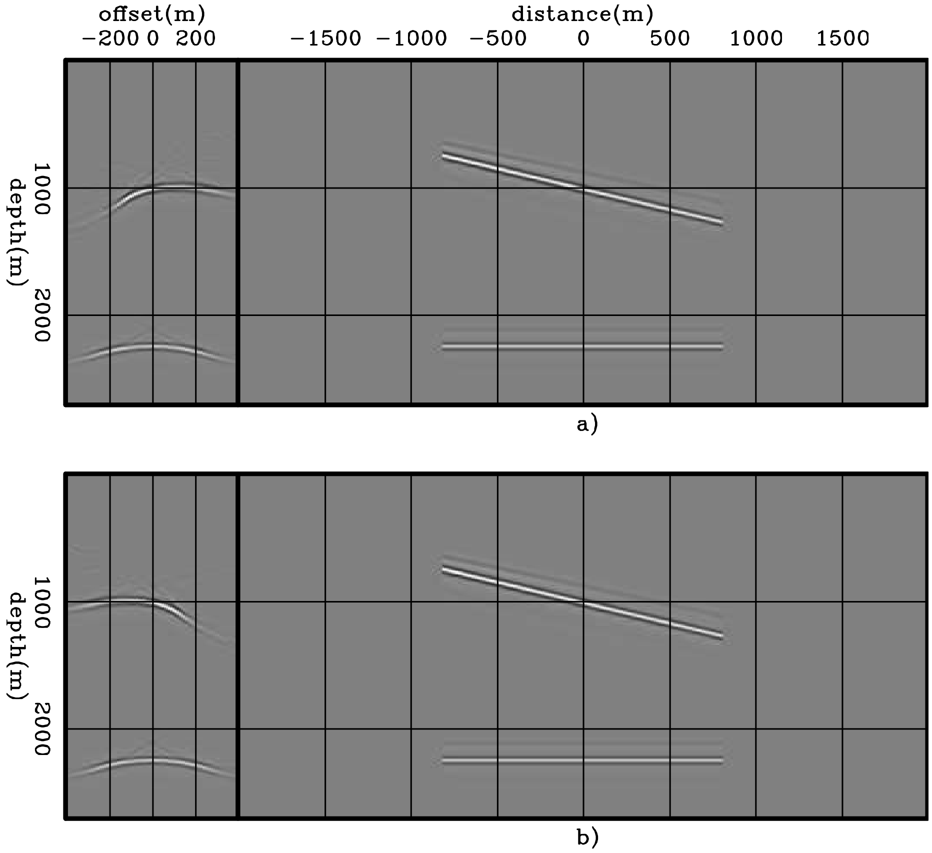

Figure 2.15: Initial conditions for modeling a) source and b) receiver wavefields. The dipping reflector is oriented in opposite directions in the SODCIG. Rotation affects neither the horizontal reflector nor the-zero subsurface offset, as can be seen in the right panels. perm/. dip05

each reflector was injected separately into the modeling.

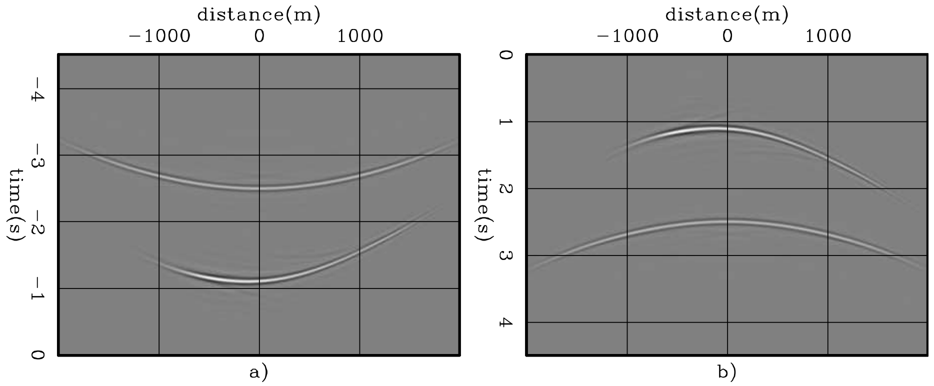

Figure 2.16: Dip-independent PERM data for the dipping reflector from the rotated SODCIG at $x_m = 0$ m. a) The receiver wavefield. b) The source wavefield. perm/. dip06

Areal-shot migration of dip-independent PERM data is shown in Figure 2.17. Notice that the segment of the dipping reflector is shifted laterally with respect to that of the horizontal reflector. Since the dip-independent wavefields carry information about the dip of the reflector, the observed reflector movement is now consistent with migration with a higher velocity.

Migration with the correct velocity of dip-independent PERM data modeled from a set of SODCIGs in a neighborhood around $x_m = 0$ m confirms the correctness of the rotation (Figure 2.18). The focusing of the dipping reflector around zero subsurface offset is greatly improved when compared with Figure 2.14. The corresponding ADCIGs confirm the more consistent move-out after rotation (Figure 2.19). Note the residual move-out in the angle gather corresponding to the image computed with wavefields with non-rotated initial conditions (Figure 2.19a), and the image from wavefields computed with the proposed rotation is much flatter (Figure 2.19b).

In the example with two reflectors, we initiated each modeling experiment from one isolated SODCIG of one single reflector to compute a pre-stack image restricted to a certain region in the output space. However, depending on the number of reflectors and the size of the prestack image, this procedure can generate a dataset even larger

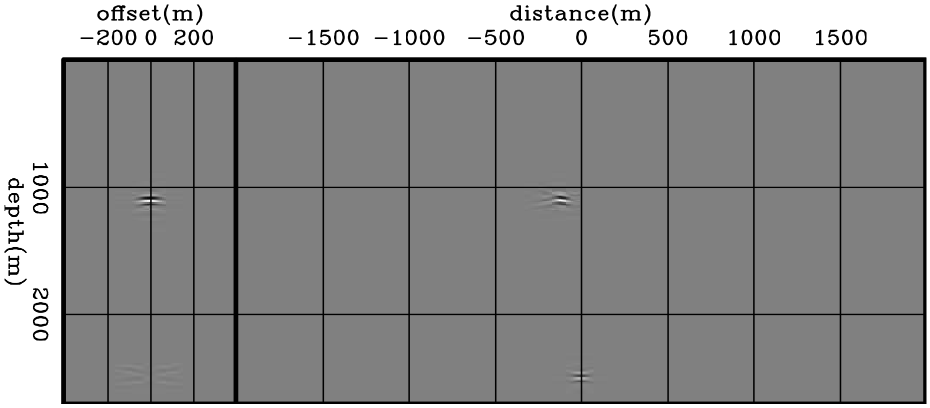

Figure 2.17: Areal-shot migration with the correct velocity of dip-independent PERM data having the rotated the SODCIGs at $x_m = 0$ m as the initial condition. The SODCIG on the left is selected at the horizontal position where the dipping reflector was laterally shifted to. Compare with Figure 2.13. The dipping reflector is now focused in contrast to the image in Figure 2.13, where it shows residual curvature. perm/. dip07

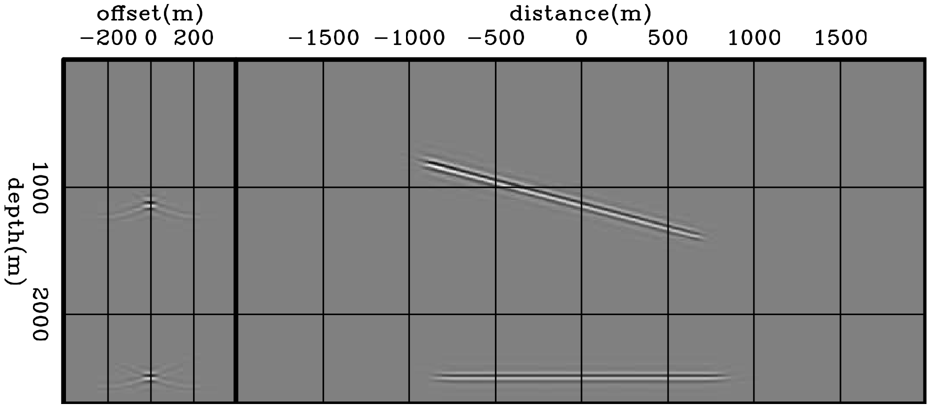

Figure 2.18: Areal-shot migration with correct velocity of dip-independent PERM data having a set of rotated SODCIGs around $x_m = 0$ m as the initial conditions. Compare with Figure 2.14. The focusing of the dipping reflector is greatly improved when using the rotated initial conditions. perm/. dip08

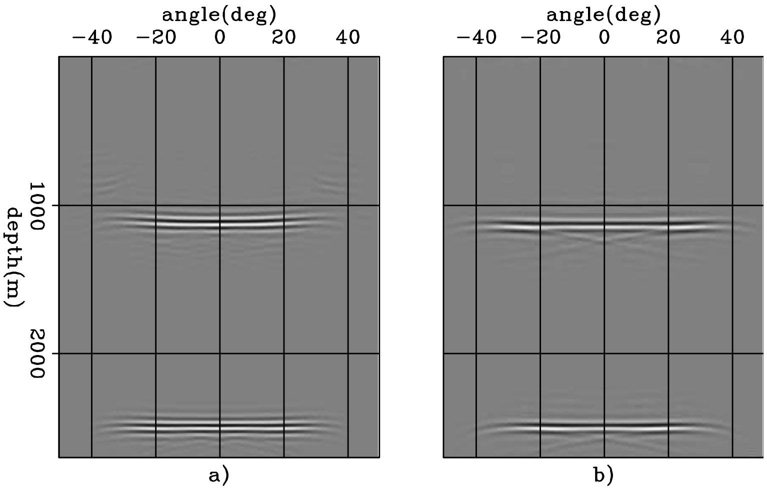

Figure 2.19: ADCIGs of images computed with the correct migration velocity using PERM data having: a) non-rotated initial conditions, and b) rotated initial conditions. Note the residual move-out in a) and the flatter response in b). perm/. dip09

than the original shot-profiles, defeating the original purpose of PERM, which is to synthesize a smaller dataset to be used in migration velocity analysis. We see next that using a combination of modeling experiments can decrease the size of PERM data.

Combination of modeling experiments

In the previous examples, if we were to fully image the reflectors, there might be twice as many areal shots as in the original shot-profiles. In equation 2.21, there is a summation over $\mathbf{x_m}$ since the initial conditions are isolated SODCIGs. To decrease the number of modeling experiments, we can apply the concept of generalized sources and use the linearity of wavefield propagation to combine isolated SODCIGs and inject them simultaneously into one single model experiment as

$$\left\{ \begin{array}{l} \left(\frac{\partial}{\partial z} - i\sqrt{\omega^2 s_0^2(\mathbf{x}) - |\mathbf{k}|^2}\right) \widehat{D_P}(\mathbf{x},\omega) = \widehat{I_D}(\mathbf{x}-\mathbf{h}) \\ \widehat{D_P}(x,y,z=z_{\max},\omega) = 0 \end{array} \right. , \tag{2.33}$$

and

$$\begin{cases} \left(\frac{\partial}{\partial z} + i\sqrt{\omega^2 s_0^2(\mathbf{x}) - |\mathbf{k}|^2}\right) \widehat{U_P}(\mathbf{x},\omega) = \widehat{I_U}(\mathbf{x}+\mathbf{h}) \\ \widehat{U_P}(x,y,z=z_{\max},\omega) = 0 \end{cases}, \tag{2.34}$$

where $\widehat{I_D}(\mathbf{x}-\mathbf{h})$ and $\widehat{I_U}(\mathbf{x}+\mathbf{h})$ are the combination of SODCIGs for a single reflector to be used as the initial conditions for the modeling of combined wavefields, $\widehat{D_P}(\mathbf{x},\omega)$ and $\widehat{U_P}(\mathbf{x},\omega)$, the source and receiver wavefields, respectively. The selection of SODCIGs can be thought of as the multiplication of the pre-stack image by a 2D–comb function, which is shifted laterally to select new set of SODCIGs to initiate the modeling of another pair of combined wavefields. After shifting along one period of the sampling function in the x and y directions, all the points on the reflector are used in the modeling. Consequently, the number of modeling experiments equals the number of lateral shifts of the sampling function.

Since the wavefields are initiated on the reflectors using combinations of SODCIGs, the idea of generalized sources applies, characterizing the image-space generalized source domain.

Again, for one particular frequency and a plane reflector so that the initial conditions are the same for modeling source $\widehat{D}_P$ and receiver $\widehat{U}_P$ wavefields, the modeling of a pair of PERM wavefields starting from combined SODCIGs can be described by

$$\widehat{D_P}(\boldsymbol{\xi};\Delta\mathbf{x}) = \sum_{\mathbf{x}}\sum_{\mathbf{h}}\sum_{m} G_0(\boldsymbol{\xi},\mathbf{x}-\mathbf{h})\delta(\widehat{\mathbf{x}}-m\Delta\mathbf{x})I(\widehat{\mathbf{x}},\mathbf{h}), \tag{2.35}$$

and

$$\widehat{U_P}(\boldsymbol{\xi};\Delta\mathbf{x}) = \sum_{\mathbf{x}}\sum_{\mathbf{h}}\sum_{m} G_0(\boldsymbol{\xi},\mathbf{x}+\mathbf{h})\delta(\widehat{\mathbf{x}}-m\Delta\mathbf{x})I(\widehat{\mathbf{x}},\mathbf{h}), \tag{2.36}$$

where $\sum_{m}\delta(\widehat{\mathbf{x}}-m\Delta\mathbf{x})$ is the 2D–sampling function.

The wavefields are recursively downward propagated in depth according to

$$\widehat{D_P}(\mathbf{x};\Delta\mathbf{x}) = \sum_{\boldsymbol{\xi}} G_1^*(\boldsymbol{\xi},\mathbf{x})\widehat{D_P}(\boldsymbol{\xi}), \tag{2.37}$$

and

$$\widehat{U_P}(\mathbf{x};\Delta\mathbf{x}) = \sum_{\boldsymbol{\xi}} G_1^*(\boldsymbol{\xi},\mathbf{x})\widehat{U_P}(\boldsymbol{\xi}). \tag{2.38}$$

The lateral shifts of the wavefields for the multi-offset imaging condition are represented by

$$\begin{aligned}\widehat{D_P}(\mathbf{x}-\mathbf{h};\Delta\mathbf{x}) &= \sum_{\boldsymbol{\xi}} G_1^*(\boldsymbol{\xi},\mathbf{x}-\mathbf{h}) \\ &\times \sum_{\mathbf{x}'}\sum_{\mathbf{h}'}\sum_{m} G_0(\boldsymbol{\xi},\mathbf{x}'-\mathbf{h}')\delta(\widehat{\mathbf{x}}-m\Delta\mathbf{x})I(\widehat{\mathbf{x}},\mathbf{h}'),\end{aligned} \tag{2.39}$$

and

$$\begin{aligned}\widehat{U_P}(\mathbf{x}+\mathbf{h};\Delta\mathbf{x}) &= \sum_{\boldsymbol{\xi}} G_1^*(\boldsymbol{\xi},\mathbf{x}+\mathbf{h}) \\ &\times \sum_{\mathbf{x}'}\sum_{\mathbf{h}'}\sum_{m} G_0(\boldsymbol{\xi},\mathbf{x}'+\mathbf{h}')\delta(\widehat{\mathbf{x}}-m\Delta\mathbf{x})I(\widehat{\mathbf{x}},\mathbf{h}').\end{aligned} \tag{2.40}$$

Applying the cross-correlation imaging condition to the wavefields of equations 2.39 and 2.40 gives

$$\begin{aligned}\widehat{I_P}(\mathbf{x},\mathbf{h};\Delta\mathbf{x}) &= \sum_{\boldsymbol{\xi}'}\sum_{\mathbf{x}'}\sum_{\mathbf{h}'}\sum_{m}\sum_{\boldsymbol{\xi}''}\sum_{\mathbf{x}''}\sum_{\mathbf{h}''}\sum_{n} G_0(\boldsymbol{\xi}',\mathbf{x}'-\mathbf{h}')G_1^*(\boldsymbol{\xi}',\mathbf{x}-\mathbf{h}) \\ &\times G_1^*(\boldsymbol{\xi}'',\mathbf{x}+\mathbf{h})G_0(\boldsymbol{\xi}'',\mathbf{x}''+\mathbf{h}'')\delta(\widehat{\mathbf{x}}-m\Delta\mathbf{x})\delta(\widehat{\mathbf{x}}-n\Delta\mathbf{x}) \\ &\times I(\widehat{\mathbf{x}},\mathbf{h}')I(\widehat{\mathbf{x}},\mathbf{h}''),\end{aligned} \tag{2.41}$$

which can be recast as

$$\begin{aligned} \widehat{I_P}(\mathbf{x},\mathbf{h};\Delta\mathbf{x}) &= I_P(\mathbf{x},\mathbf{h};\Delta\mathbf{x}) \\ &+ \sum_{\boldsymbol{\xi}'}\sum_{\mathbf{x}'}\sum_{\mathbf{h}'}\sum_{\boldsymbol{\xi}''}\sum_{\mathbf{x}''}\sum_{\mathbf{h}''}\sum_{n\neq m} G_0(\boldsymbol{\xi}',\mathbf{x}'-\mathbf{h}')G_1^*(\boldsymbol{\xi}',\mathbf{x}-\mathbf{h}) \\ &\times G_1^*(\boldsymbol{\xi}'',\mathbf{x}+\mathbf{h})G_0(\boldsymbol{\xi}'',\mathbf{x}''+\mathbf{h}'')\delta(\widehat{\mathbf{x}}-m\Delta\mathbf{x})\delta(\widehat{\mathbf{x}}-n\Delta\mathbf{x}) \\ &\times I(\widehat{\mathbf{x}},\mathbf{h}')I(\widehat{\mathbf{x}},\mathbf{h}''). \end{aligned} \tag{2.42}$$

The first term in the right-hand side of equation 2.42 is the desired image we would obtain by independently modeling and migrating PERM wavefields. The second term represents crosstalk. To obtain a crosstalk-free image, the sampling period must be large enough that wavefields initiated at different SODCIGs do not correlate. As previously shown when discussing how to compute PERM images with kinematics similar to those of the original shot-profile migration, PERM wavefields generated from SODCIGs within an interval equals to twice the subsurface-offset range $\boldsymbol{\eta}$ still contribute to the image at the central SODCIG. Crosstalk will occur if the sampling period is shorter than that interval. This is easily seen by realizing that the terms $\delta(\widehat{\mathbf{x}'}-m\Delta\mathbf{x})I(\widehat{\mathbf{x}'},\mathbf{h}')$ and $\delta(\widehat{\mathbf{x}''}-n\Delta\mathbf{x})I(\widehat{\mathbf{x}''},\mathbf{h}'')$ are 2D–periodic-rectangular functions with period $\Delta\mathbf{x}$ and width $\boldsymbol{\eta}$. We want the spatial 2D–correlation of these functions to be a 2D–periodic triangular function, without interference between the individual 2D–triangles. This is achieved by setting $\Delta\mathbf{x} > \boldsymbol{\eta}$.

The combination of modeling experiments is illustrated in Figure 2.20. We model PERM data starting with the rotated images from the previous section and combine SODCIGs into sets using the sampling period of 163 SODCIGs. Recalling that the number of subsurface-offsets is 81, it is expected that no crosstalk will occur when migrating the set with sampling period of 163 SODCIGs. In this case, since each reflector is used separately in the modeling, the total number of areal shots is 326, which is less than half of the original shot profiles.

We saw that carefully combining the modeling experiments decreases the data size while maintaining the correct kinematics, which is important for migration velocity

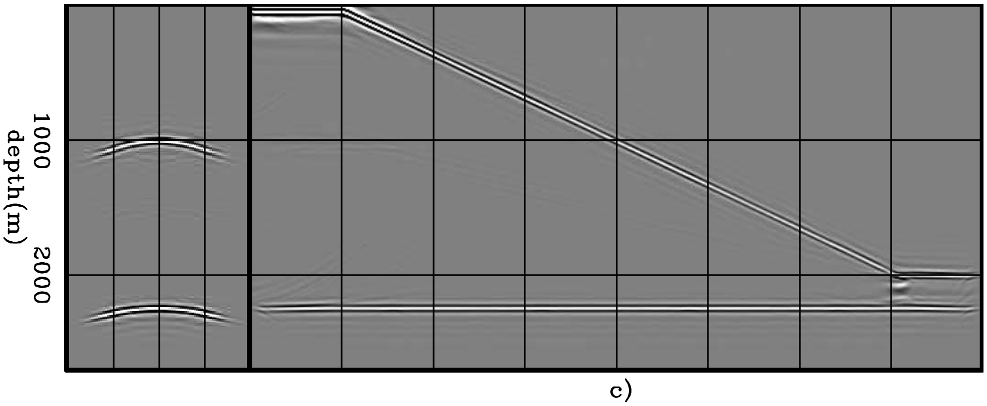

Figure 2.20: Areal-shot migration of PERM data synthesized from sets of SODCIGs selected with sampling period of 163 SODCIGs. Notice that no crosstalk is generated when the sampling period is larger than twice the subsurface-offset range. perm/. comb01b

analysis. However, combining the modeling experiments using a decorrelation distance between events does not achieve a significant data reduction, at least in 2D. In this case, data reduction depends on the number of subsurface-offsets which are necessary to capture all the relevant velocity information. In the example, the number of independent experiments is only less than one half as many as in the original dataset. Data reduction techniques like plane-wave decomposition, for instance, could lower data size by a factor of ten. As we will see in Chapter 3, further data reduction can be achieved by using the phase-encoding technique (Romero et al., 2000) to linearly combine the modeling experiments. This will enable us to use a shorter sampling period of SODCIGs, and also to inject more than one reflector in the modeling.

Although PERM theory was developed in 3D, all the examples I have shown so far have been 2D. Next, I discuss a 3D example under the common-azimuth approximation (Biondi and Palacharla, 1996) and show that in this case the SODCIGs in the y direction can be continuously sampled, and the number of modeling experiments will depend only on the sampling period in the x direction, drastically decreasing data size.

3D-PERM from common-azimuth migrated images

In the way PERM is formulated there is no restriction on the dimensionality of the pre-stack image used as the initial condition for the modeling, which means that if the original data have sufficient cross-line offsets as in the acquisition geometries with wide range of azimuths (Regone, 2007; Kapoor et al., 2007; Moldoveanu et al., 2008), the initial conditions are a five-dimensional hypercube on $\mathbf{x}$, h_x and h_y.

To synthesize PERM data starting with the five-dimensional initial conditions such that no crosstalk is generated during migration, the minimum number of modeling experiments is $4n_{h_x}n_{h_y}$, where n_{h_x} and n_{h_y} are the number of subsurface offsets in the x and y directions. Considering the usual parameters, the number of modeling experiments may be as low as several hundreds. This data reduction is very substantial if we compare, for instance, with data reduction achieved by 3D-plane-wave migration. Using plane waves, to obtain artifact-free SODCIGs due to the lack of illumination from some propagation directions we need to migrate roughly 2000 plane waves. This means that 3D-PERM data size can be one order of magnitude smaller than 3D-plane wave data.

Despite the recent good migration results obtained in geologically complex areas using wide-azimuth data, narrow-azimuth acquisition is still the industry standard. Narrow-azimuth data can be efficiently imaged by common-azimuth wave-equation migration (CAM) (Biondi and Palacharla, 1996). CAM reduce the dimensionality of the pre-stack wavefields, and therefore the cost of migration, by assuming zero cross-line offset. That does not mean that the cross-line offset wavenumber is zero. Rather, its asymptotic approximation is a function of the the in-line midpoint and in-line offset wavenumbers. Therefore, instead of a five-dimensional hypercube, CAM images are four-dimensional hypercubes in $\mathbf{x}$ and h_x.

Because of the zero-cross-line offset assumption, when using CAM images as the initial conditions to synthesize PERM data, the SODCIGs in the cross-line direction can be sampled continuously, as depicted in Figure 2.21b. Recall that PERM is equivalent to ERM if energy is focused at the zero subsurface offset, as well as if this is the only available subsurface offset. Contrast this case with the five-dimensional initial conditions for the full azimuth case of Figure 2.21a.

The continuous sampling of SODCIGs in the cross-line direction yields one more order of magnitude of data reduction. Therefore, under the common-azimuth approximation, 3D-PERM data size can be two orders of magnitude smaller than 3D-plane wave data.

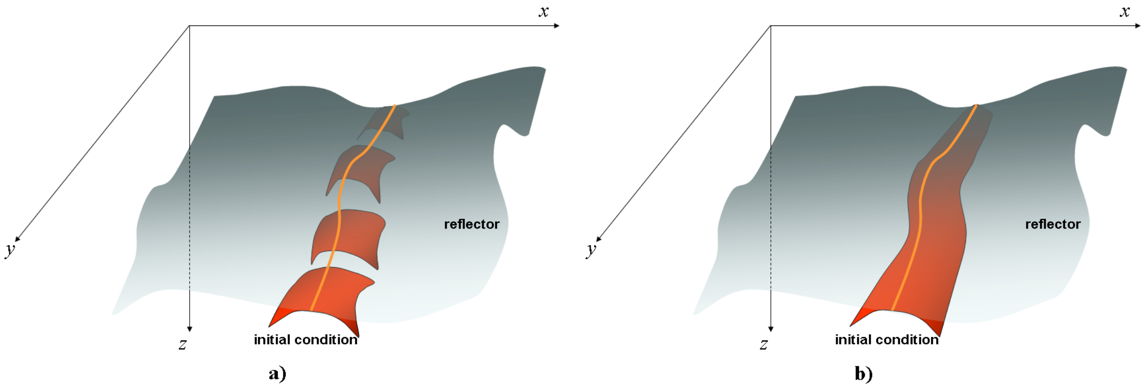

Figure 2.21: The initial conditions for synthesizing PERM data from CAM images can be specified as in b) because no pre-stack information exists in the cross-line direction, in contrast with the full azimuth situation in a). perm/. cam01

To illustrate the validity of the above assumptions, a split-spread data with maximum offset of 1587.5 m was computed using 3D-Born modeling (Rickett et al., 1996) on a 30° dipping reflector with 45° azimuth with respect to the acquisition direction, which is aligned with the in-line direction. There are 96 in-lines and cross-lines spaced 25 m apart. The offset interval is 25 m. The velocity used in the modeling is the 1D function $v(z) = (1500 + 0.5z)$ m/s.

The Born data was input to CAM with a 5% slower velocity. Migration results can be seen in Figures 2.22a and 2.22b for SODCIGs positioned at ($x = 750$ m, $y = 600$ m) and ($x = 750$ m, $y = 1000$ m), respectively. The panel on the left is the SODCIG, which contains 21 subsurface offsets ranging from -250 m to 250 m. The panel in the middle is the in-line at zero subsurface offset, with $y = 600$ m (Figure 2.22a) and $y = 1000$ m (Figure 2.22b). The panel on the right is the cross-line at zero subsurface offset, with $x = 750$ m.

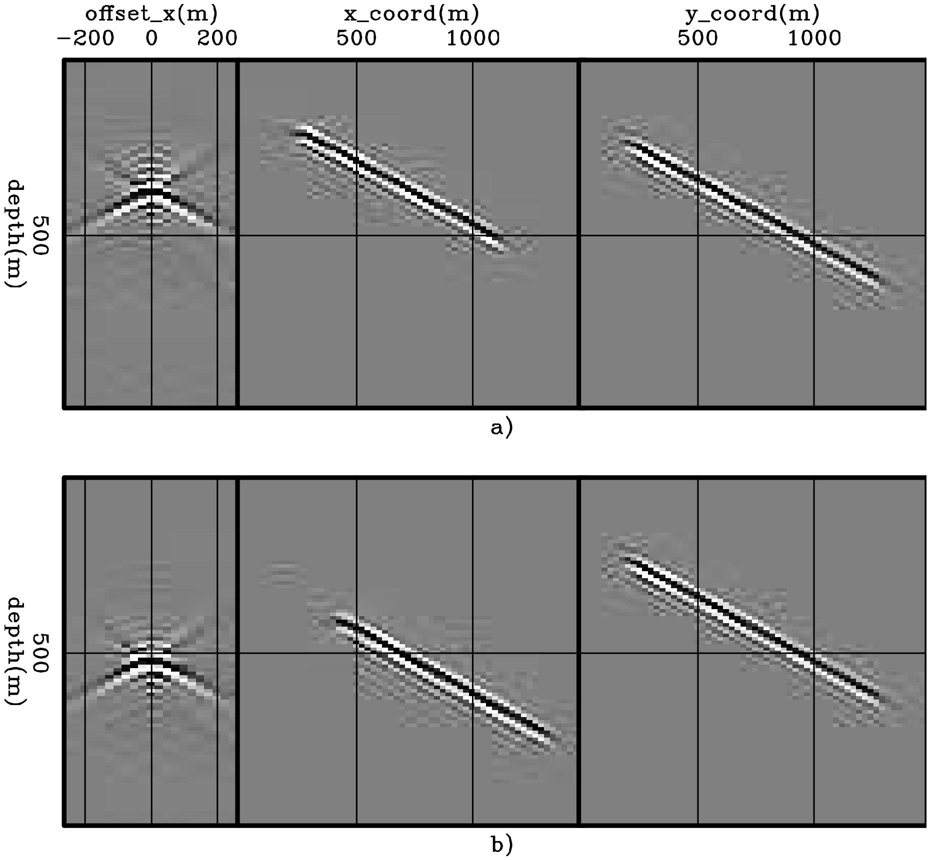

Figure 2.22: Common-azimuth migration of 3D-Born data modeled from a 30° dipping reflector with 45° azimuth with respect to the acquisition direction. The panel in the middle is the in-line at the zero-subsurface offset, and $y = 600$ m (Figure 2.22a) and $y = 1000$ m (Figure 2.22b). The panel on the right is the cross-line at the zero-subsurface offset, and $x = 750$ m. perm/. cam02

In the common-azimuth regime, the computation of the dip-independent initial conditions is performed by simply stretching the inline-subsurface-offset axis by $\sec \alpha_{y'}$ and rotating the SODCIGs in the in-line direction, since no cross-line offset is computed in migration.

To illustrate the effect of not stretching the in-line-subsurface-offset axis, source and receiver wavefields were modeled from two different initial conditions: one after simple rotation, and the other after stretching and rotation. Both used continuous sampling along the cross-line direction and sampling period of 48 in the in-line direction. This period is sufficient to avoid crosstalk during the areal-shot migration, given that the number of subsurface-offsets of the pre-stack image is 21. Only the synthesized 3D receiver wavefield for the non stretched case is shown in Figure 2.23. The left panel is the in-line at $y = 1200$ m, the right panel is the cross-line at $x = 1400$ m, and the top panel is the time-slice at $t = 0.5$ s. The 3D migrations of the 48 areal shots with the velocity underestimated by 5% are shown in Figures 2.24a-b for the non stretched case and Figures 2.25a-b for the stretched case. SODCIGs are positioned at ($x = 750$ m, $y = 600$ m) in Figures 2.24a and 2.25a, and at ($x = 750$ m, $y = 1000$

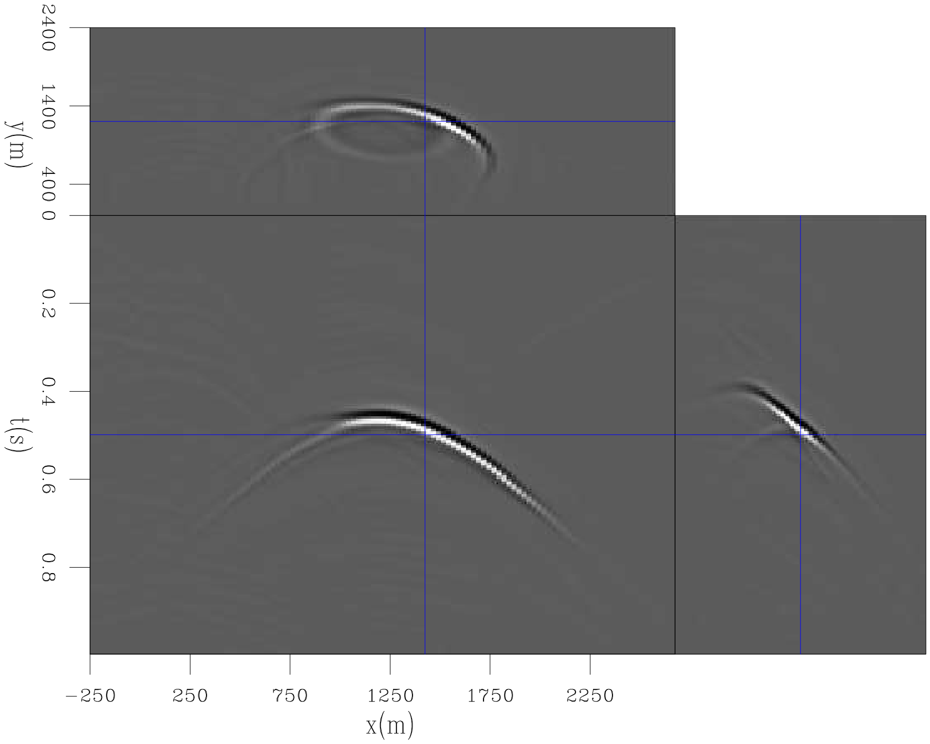

Figure 2.23: 3D-PERM receiver wavefield. The left panel is the in-line at $y = 1200$ m, the right panel is the cross-line at $x = 1400$ m, and the top panel is the time-slice at $t = 0.5$ s. $\boxed{\text{perm/. cam03}}$

m) in Figures 2.24a and 2.25a. To facilitate the comparison with the CAM images of Figures 2.22a-b, the polarity of the areal-shot migrated image is inverted due to the squaring of the wavelet. The kinematics of the SODCIGs computed with PERM wavefields overall matches those of the SODCIGs computed with CAM. However, notice how the images computed with PERM wavefields from the subsurface-offset stretched SODCIGs show slightly better amplitudes at farther subsurface offsets.

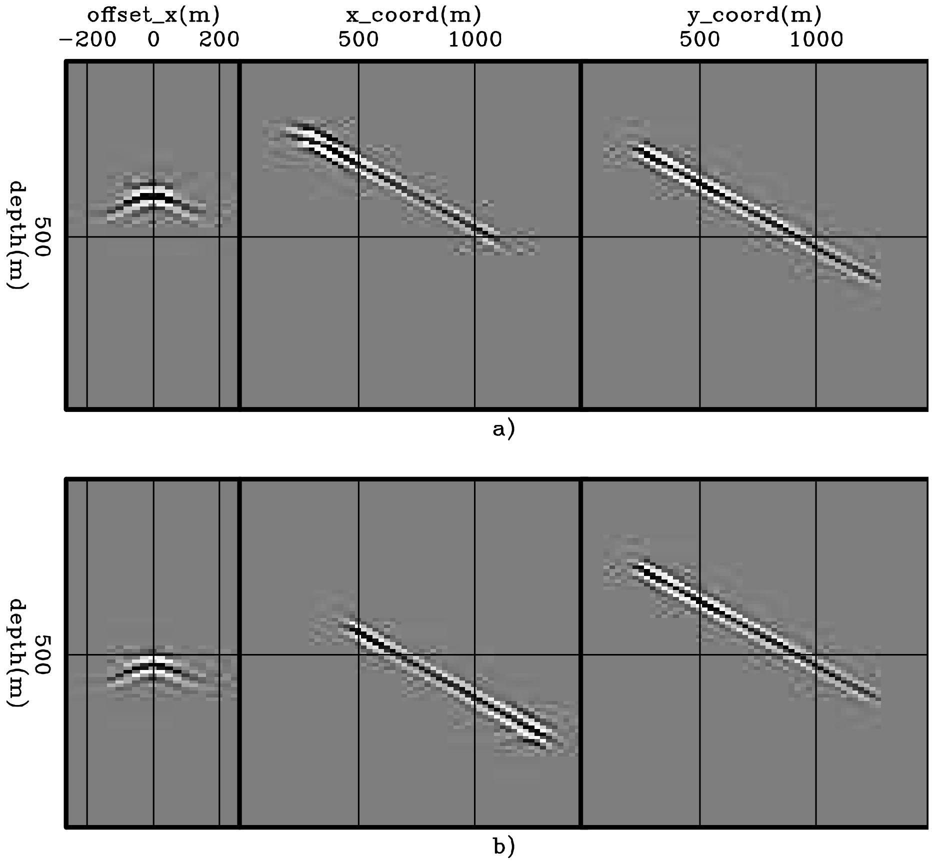

Figure 2.24: 3D-areal-shot migration of PERM data from non stretched subsurface offset SODCIGs. The panel in the middle is the in-line at the zero-subsurface offset, and $y = 600$ m (Figure 2.22a) and $y = 1000$ m (Figure 2.22b). The panel on the right is the cross-line at the zero-subsurface offset, and $x = 750$ m. Compare with Figure 2.22 and 2.25. perm/. cam04

The correct kinematics shown in Figures 2.24 and 2.25 enables the use of 3D

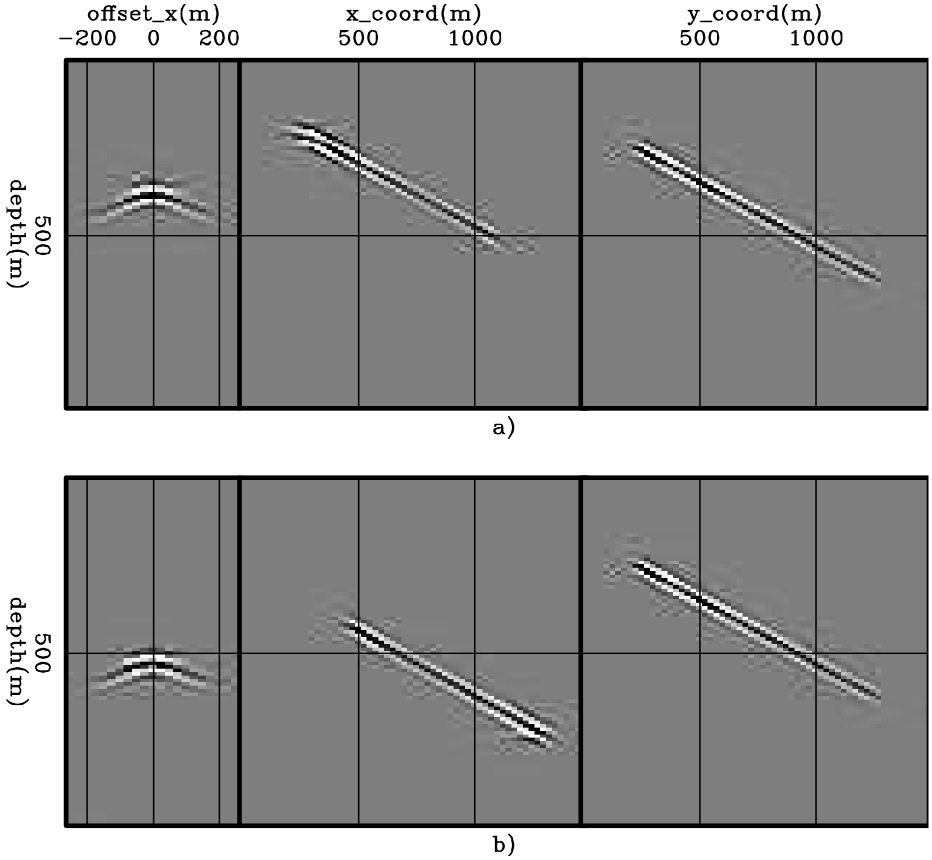

Figure 2.25: 3D-areal-shot migration of PERM data from stretched subsurface offset SODCIGs. The panel in the middle is the in-line at the zero-subsurface offset, and $y = 600$ m (Figure 2.22a) and $y = 1000$ m (Figure 2.22b). The panel on the right is the cross-line at the zero-subsurface offset, and $x = 750$ m. Compare with Figure 2.22 and 2.24. perm/. cam05

PERM wavefields computed from CAM images in the optimization of migration velocity. As the initial conditions for the modeling are continuously sampled in the cross-line direction, data size is drastically reduced. Chapter 5 will use these wavefields to optimize the migration velocity for a 3D survey from the North Sea.

CONCLUSIONS

In this chapter image-space generalized sources were obtained by combining PERM wavefields. We saw that wavefields synthesized by PERM provide migrated images with correct kinematics while decreasing data size. Data reduction is achieved by combining the modeling experiments and is controlled by the number of subsurface offsets that will be computed during areal-shot migration of PERM data. Recall that SODCIGs in the initial conditions must be separated by at least twice the maximum absolute subsurface-offset value to prevent crosstalk. Implicit to PERM is the requirement that reflectors must be identified in order to avoid reflector crosstalk during migration. 3D Pre-stack interpretation can be cumbersome, but it allows avoiding the use of reflectors with low signal-to-noise ratios in migration-velocity estimation. Moreover, in commercial software for migration velocity estimation reflector picking is a standard and almost entirely automated procedure.

Whereas in 2D PERM data size is comparable to that of the plane-wave decomposition, in 3D it is one order of magnitude smaller when computing cross-line subsurface-offsets. Further data size reduction by another order of magnitude is achieved if the initial conditions are computed with common-azimuth migration.

Chapter 3

Image-space phase-encoded wavefields

This chapter introduces image-space phase-encoded wavefields (ISPEW). ISPEW are computed using PERM along with phase-encoding techniques to further improve data reduction achieved with PERM. In this sense, ISPEW can also be defined as image-space generalized source wavefields. The phase encoding is performed during the modeling, in which every event in the initial conditions has its particular code. Phase encoding during the modeling allows injection of more closely spaced SODCIGs and multiple reflectors, while diminishing the prejudicial effect of crosstalk during imaging. Modeling of ISPEW can be confined to a region of the subsurface where the velocity model is inaccurate, allowing migration velocity analysis using wavefield extrapolation to be easily solved in a target-oriented manner. The use of phase encoding combined with the target-oriented modeling dramatically decreases the cost of migration velocity analysis, especially in 3D projects.

INTRODUCTION

Chapter 2 introduced the pre-stack exploding-reflector model (PERM). Using the concept of exploding reflectors, PERM synthesizes new wavefields that enables us to compute pre-stack images by wavefield extrapolation methods at a low cost. In 3D, PERM data size can be up to two orders of magnitude smaller than plane-wave data.

The strategy used in Chapter 2 to ensure that crosstalk of wavefields does not occur during migration is, using of the linearity of wavefield propagation, to simultaneously inject SODCIGs separated by a decorrelation distance equal to twice the subsurface-offset range. This decorrelation distance in PERM modeling plays a role similar to the grating interval in an optical fiber, which influences optical crosstalk in optical transmission systems and networks (Yamada et al., 1998). Crosstalk is further reduced (and bandwidth increased) by phase encoding the optical information (Teh et al., 2001).

Phase encoding is a well-established technique in radar (Levanon and Mozeson, 2004), medical imaging (Bernstein et al., 2005; Weishaupt et al., 2006), cryptography (Wang et al., 1996; Javidi et al., 1996) and wireless communication (Castoldi, 2002; Zigangirov, 2004). Phase encoding enables faster data acquisition, larger bandwidth and more reliable signal recovery. In wireless communication, for instance, systems using Code Division Multiple Access (CDMA), a method for accessing communication channels, allow several users to share the same communication channel without crosstalk. This is achieved by encoding the information during transmission using sequences with unique correlation properties (Gold, 1967; Dinan and Jabbari, 1998). Information is recovered with minimal distortion after decoding with the corresponding sequence.

Phase encoding has been long used in seismic exploration to enable simultaneous shooting for acquisition with seismic vibrators (Ward et al., 1990; Martin, 1993; Bagaini, 2006). To decrease seismic imaging cost, using the concept of generalized sources, wavefields are usually phase-encoded using phase functions like the plane-wave phase function (Schultz and Claerbout, 1978; Whitmore, 1995; Liu et al., 2006;

Duquet and Lailly, 2006) and random phase functions (Romero et al., 2000; Sun et al., 2002). Recently, phase-encoded wavefields have also been applied to velocity estimation by waveform inversion (Vigh and Starr, 2008; Ben-Hadj-Ali et al., 2009; Krebs et al., 2009) and migration-velocity analysis using wavefield extrapolation (Shen and Symes, 2008; Guerra et al., 2009a). Phase-encoded wavefields can also be used to decrease the cost of computing the Hessian operator in least-squares migration (Tang, 2009).

Usually, phase encoding is applied in the data space. Shot gathers are weighted with, ideally, orthogonal phase functions, and combined into areal shots. The corresponding point sources are also encoded with the same phase functions and combined into areal source functions. During migration, the cross-correlation of related wavefields, encoded with the same phase function, yields strong amplitudes corresponding to the real reflectors. The cross-correlation of unrelated wavefields, encoded with different phase functions, yields attenuated amplitudes corresponding to the attenuated crosstalk.

A similar strategy can be applied in the model space to encode PERM experiments (Guerra and Biondi, 2008b,a). A different pseudo-random sequence is assigned to each SODCIG used in the modeling of a pair of PERM wavefields, so that during migration correlation of unrelated wavefields is attenuated. This characterizes the image-space phase-encoded wavefields (ISPEW), and it allows decreasing the sampling interval of the combined SODCIGs and using more than one reflector in the initial conditions.

To provide relevant information for velocity updates when using generalized sources, crosstalk must be incoherent. This has been observed by Krebs et al. (2009) in the context of waveform inversion using phase-encoded wavefields, for which using different codes for different iterations yields more accurate models and improves convergence. Similarly, in the context of migration velocity analysis by wavefield extrapolation using ISPEW, if necessary, several random realizations of ISPEW can be computed to be used in different velocity iterations.

In migration velocity analysis using ray methods, it is common practice to limit the velocity update to a certain portion of the model space, especially for deeper levels when the velocity model is accurate enough at shallower depths. However, when performing pre-stack depth migration during velocity iterations, the entire model space has to be imaged. To avoid the worthless computation of the migrated image in regions where the velocity is sufficiently accurate, the wavefields can be downward extrapolated up to a datum at the bottom of this region (Berryhill, 1979; Bevc, 1997; Wang et al., 2006). Hence, if the wavefields are datumized, migration can be restricted to the region where the velocity accuracy needs to be improved.

Since PERM wavefields are upward propagated, they can be collected at any depth. Therefore, limiting the velocity update to the inaccurate velocity region is easily achieved using these wavefields. After being upward propagated with the inaccurate velocity of deeper levels, PERM wavefields are collected at the top of the inaccurate velocity region. Thus, PERM naturally datumizes the wavefields. ISPEW takes advantage of this characteristic to decrease the cost of both the modeling and migration velocity analysis iterations.

In this chapter, I describe how crosstalk is generated when migrating PERM data computed from combined SODCIGs separated by an interval that is shorter than the decorrelation distance and with more than one reflector in the initial conditions. I will show that phase-encoding techniques can be applied to the modeling of ISPEW, yielding further data size reduction while attenuating the deleterious effects of crosstalk. I will use an example with the Marmousi model to illustrate the usefulness of ISPEW to migration-velocity analysis.

CROSSTALK GENERATION

In the combination of modeling experiments of Chapter 2, two basic restrictions were applied to the initial conditions. First, the initial conditions contained only one reflector. Second, the sampling period was sufficiently large to avoid crosstalk during migration (Figures 2.20 and 2.24). Considering that we probably need more than one reflector to define the velocity structure, the first restriction would increase the number of the modeling experiments by a factor equal to the number of selected reflectors. Moreover, because the choice of the sampling period depends on how many subsurface offsets are needed for performing velocity updates, data size reduction is partly conditioned by the velocity inaccuracy, which causes energy to spread to subsurface offsets different from zero. As we will see in this section, if these restrictions are not observed, two different kinds of crosstalk are formed: one related to the correlation of wavefields from different reflectors, and the other related to the correlation of wavefields from unrelated SODCIGs. The first originates during the cross-correlation in time, whereas the second originates during the cross-correlation in space.

Let us first consider the crosstalk from different reflectors. Since reflectors are simultaneously injected in the initial condition, several events are present both in the source wavefield and in the receiver wavefield, as in Figure 2.16. During migration, in addition to the expected cross-correlations between the source and receiver wavefields synthesized from the same reflector, cross-correlation of wavefields from different reflectors will occur, generating crosstalk between reflectors. Areal-shot migration of a pair of PERM wavefields synthesized from a set of SODCIGs with sampling period of 163 is shown in Figure 3.1. The intermediate events between the dipping and the deeper reflectors are due to the cross-correlation of wavefields initiated at different reflectors.

To illustrate the reflector crosstalk generation, snapshots of the wavefield propagation are shown in Figure 3.2. Both wavefields are represented in the same panel. The panels on the left show the wavefields in the time-depth domain selected at horizontal positions where reflector crosstalk occurs in Figure 3.1. The panels on the right are taken at the propagation time when the wavefields cross on the left panels. The crossing times vary from 0.14 s to 1.24 s for the SODCIGs from right to left, respectively. The crossing times are a function of local dips, distance and propagation velocity between reflectors $\overline{v}$. For the simple case of parallel reflectors, the wavefield

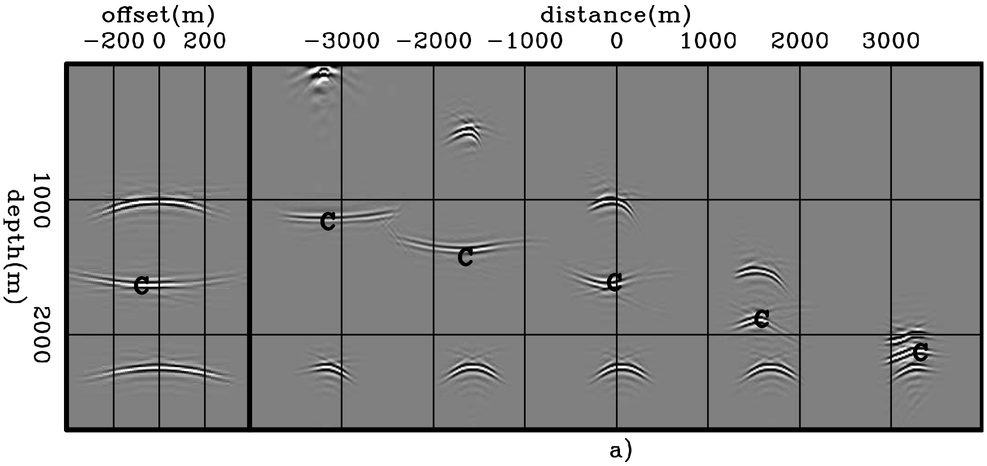

Figure 3.1: Areal-shot migration of PERM data synthesized from a set of SODCIGs selected with sampling period of 163. The two reflectors are simultaneously injected to the model. Notice the reflector crosstalk, labeled with ‘C’, resulting from the cross-correlation of the wavefields from the horizontal reflector with that from the dipping reflector. ispew/. comb02

propagation time at which reflector crosstalk t_{rc} occurs is

$$t_{rc} = \frac{0.5\Delta z_r}{\overline{v}}, \tag{3.1}$$

where Δz_r is the distance between reflectors.

Now let us consider the crosstalk formed by cross-correlating wavefields from unrelated SODCIGs of the same areal shot. From equation 2.42, repeated here,

$$\begin{aligned} \widehat{I_P}(\mathbf{x},\mathbf{h};\Delta\mathbf{x}) &= I_P(\mathbf{x},\mathbf{h};\Delta\mathbf{x}) + \sum_{\boldsymbol{\xi}'}\sum_{\mathbf{x}'}\sum_{\mathbf{h}'}\sum_{\boldsymbol{\xi}''}\sum_{\mathbf{x}''}\sum_{\mathbf{h}''}\sum_{n\neq m} G_0(\boldsymbol{\xi}',\mathbf{x}'-\mathbf{h}')G_1^*(\boldsymbol{\xi}',\mathbf{x}-\mathbf{h}) \\ &\times G_1^*(\boldsymbol{\xi}'',\mathbf{x}+\mathbf{h})G_0(\boldsymbol{\xi}'',\mathbf{x}''+\mathbf{h}'')\delta(\widehat{\mathbf{x}'}-m\Delta\mathbf{x})\delta(\widehat{\mathbf{x}''}-n\Delta\mathbf{x}) \\ &\times I(\widehat{\mathbf{x}'},\mathbf{h}')I(\widehat{\mathbf{x}''},\mathbf{h}''). \end{aligned}$$

we see that the crosstalk has structure similar to that of the desired image. Crosstalk is not formed for $\Delta\mathbf{x} > \boldsymbol{\eta}$, where $\boldsymbol{\eta}$ is the decorrelation distance equal to twice the subsurface-offset range. If this criterion is not observed, crosstalk will occur in the SODCIGs according to a period of $\Delta\mathbf{x}$.

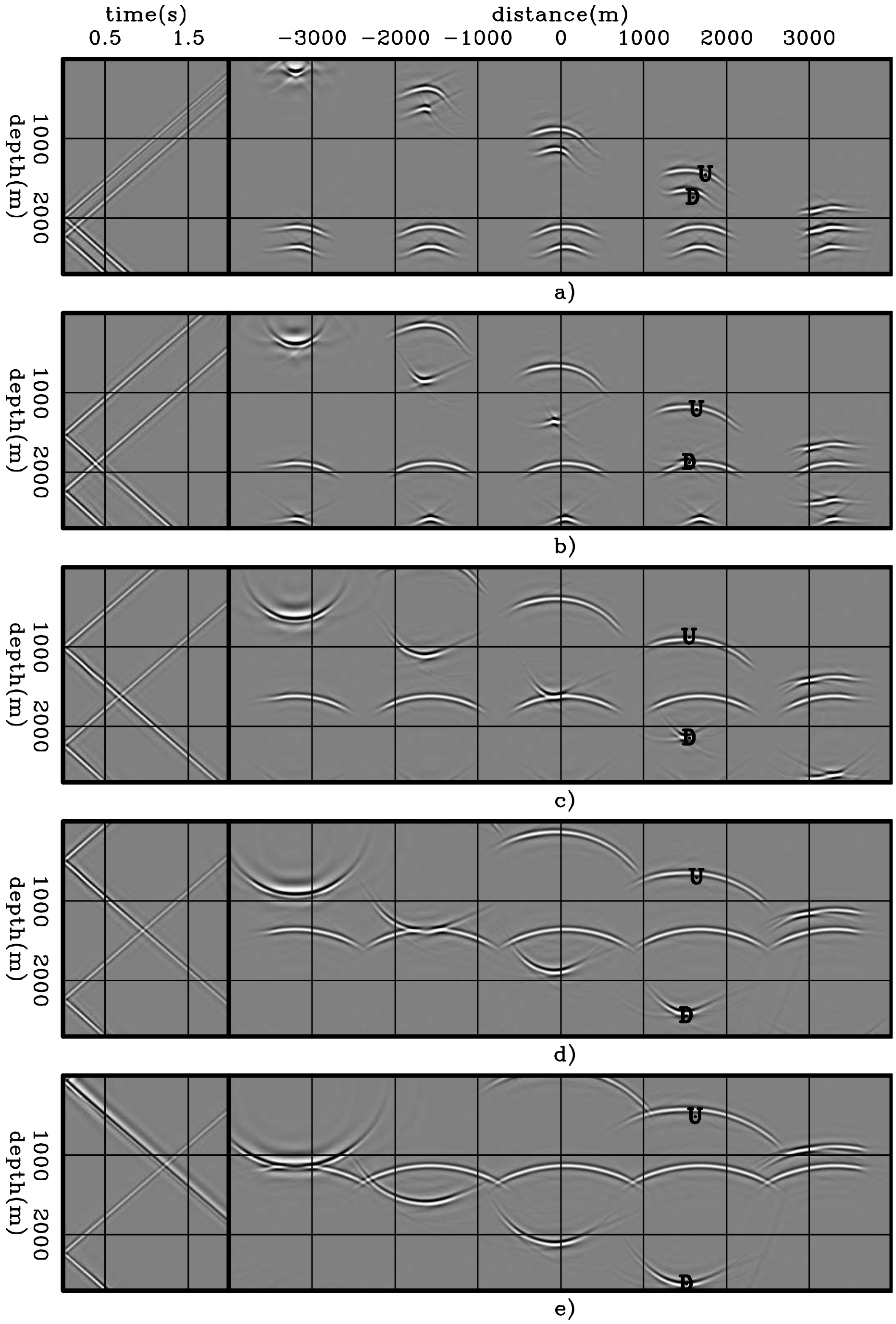

Figure 3.2: Snapshots of propagation of wavefields used to compute the image of Figure 3.1. Wavefields are labeled 'D' (Downgoing) for the source wavefield and 'U' (Upgoing) for the receiver wavefield. The panels on the left are selected at horizontal positions where the crosstalk occurs in Figure 3.1. The panels on the right are taken at the propagation time when the wavefields cross on the left panel. ispew/. comb03

To see how crosstalk from unrelated SODCIGs is formed, let us use the same two-reflector model as in Chapter 2. PERM data were modeled starting from the rotated images of Figure 2.15 using SODCIGs combined into sets with sampling period of 41 and 81 SODCIGs. Equation 2.19 shows that no crosstalk is generated if the sampling period is chosen to be the decorrelation distance of twice the subsurface-offset range, which in the present case must be greater than the distance spanned by 162 SODCIGs. Recall that the number of subsurface offsets in the original image is 81. As can be seen in Figures 3.3a and 3.3b, crosstalk occurs according periods of one-fourth and one-half of the sampling period, respectively. The corresponding ADCIGS at $x = 0$ m and the ADCIG computed from the image with no crosstalk are shown in the top panels of Figure 3.4. In the bottom panels we can see the corresponding ρ scans, computed using equation D-7 in Biondi and Symes (2004). Notice that manual picking can identify the correct $\rho = 0.9$ in Figures 3.4a-b. Therefore, ray-based methods for velocity update can back-project the correct moveout information. However, when wavefield-extrapolation methods are used velocity update, perturbed images computed from Figures 3.3a-b or 3.4a-b will potentially provide incorrect gradients.

CROSSTALK ATTENUATION

Let us now consider two different strategies to attenuate the two different types of crosstalk: the reflector crosstalk and the crosstalk from unrelated SODCIGs. In the first strategy, we will take advantage of the imaging principle to perform time cross-correlations within a window centered at zero time of wavefield propagation to avoid reflector crosstalk. In the second strategy, we will use random-phase encoding to combine the modeling experiments to attenuate both types of crosstalk. These are mutually excluding strategies, because when wavefields are phase encoded, the reference for the zero time of wavefield propagation is lost, since the frequency components of the wavefields are randomly injected in time into the modeling. We illustrate the crosstalk attenuation using a smoothed version of the Marmousi model.

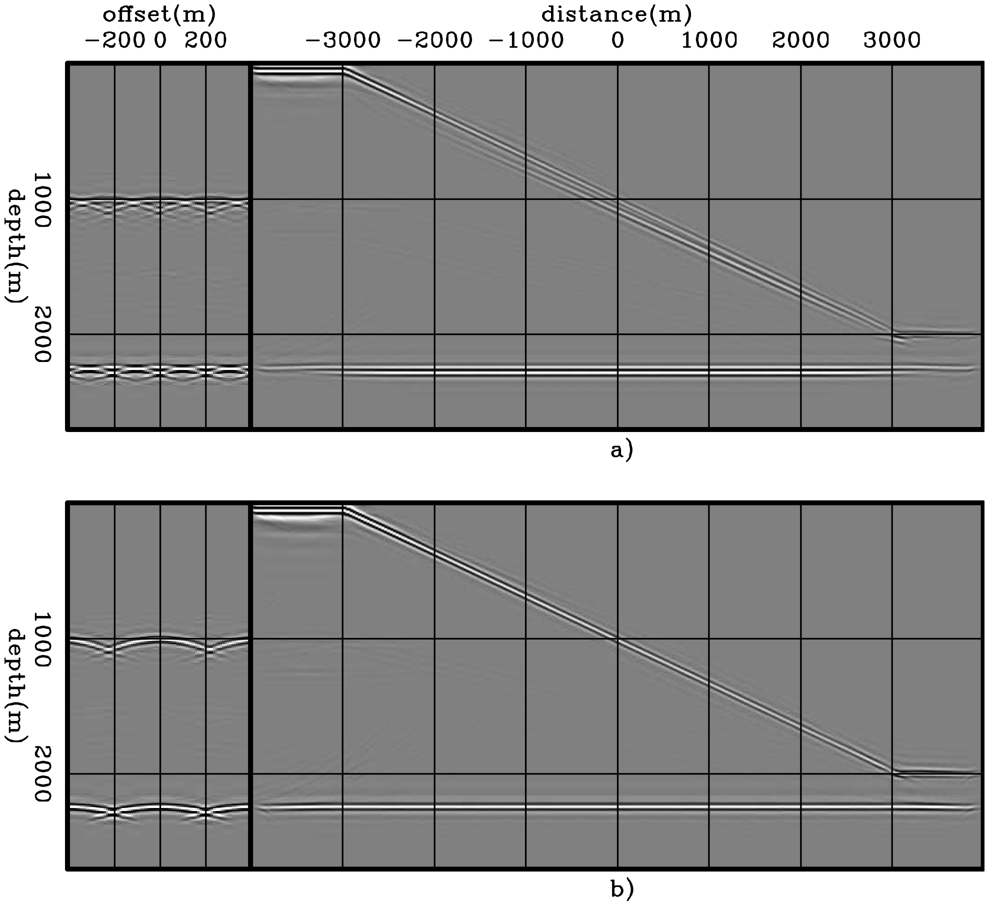

Figure 3.3: Areal-shot migration of PERM data synthesized from sets of SODCIGs selected with sampling period of: a) 41 and, b) 81. ispew/. ispew01

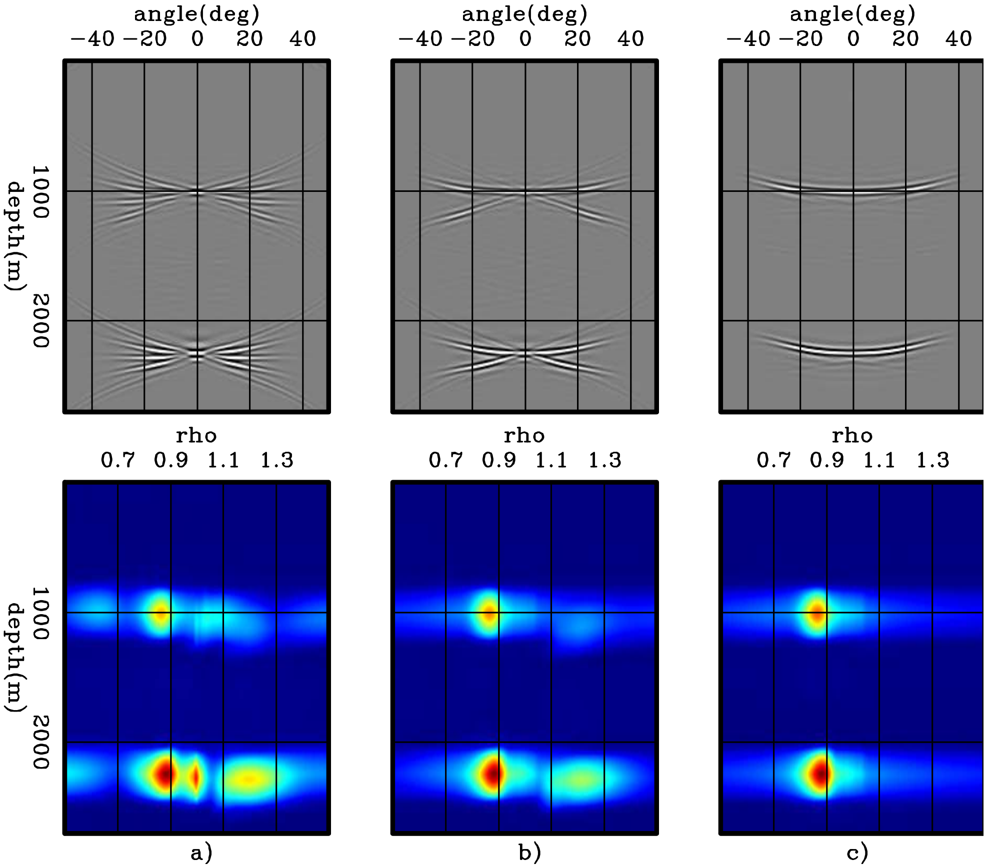

Figure 3.4: ADCIGs (top) and ρ-panels (bottom) corresponding to images computed by wavefields modeled with sampling period of: a) 41, b) 81, and c) 163. Velocity information has been destroyed by the crosstalk in a) and b). ispew/. ispew02

Time-windowed imaging condition

From Figure 3.2a, notice that for propagation times less than 0.14 s minus the period of the wavelet in time, no crosstalk will occur. This observation can be used to avoid crosstalk by applying a modified imaging condition. As Figure 3.2 shows, crosstalk is formed at times different from zero. Therefore, if the wavefields are cross-correlated within a time window centered at time zero with a length that excludes the times at which crosstalk is formed, reflector crosstalk can be avoided (Biondi, 2007). The time-windowed imaging condition for a single pair of areal shot reads

$$I_{P_w}(\mathbf{x},\mathbf{h}) = \sum_{\frac{-t_w}{2} \le t \le \frac{t_w}{2}} \mathcal{F}^{-1}\left[D^*(\mathbf{x}-\mathbf{h})\right]\mathcal{F}^{-1}\left[U(\mathbf{x}+\mathbf{h})\right], \tag{3.2}$$

where t_w is the length of the time window. When using one-way propagators, the wavefields are inverse Fourier transformed to time by $\mathcal{F}^{-1}$. Migration using the time-windowed imaging condition of equation 3.2 is shown in Figure 3.5. The length of the time window is 0.06 s, which avoids the cross-correlation of events from different reflectors. The image is completely free of reflector crosstalk.

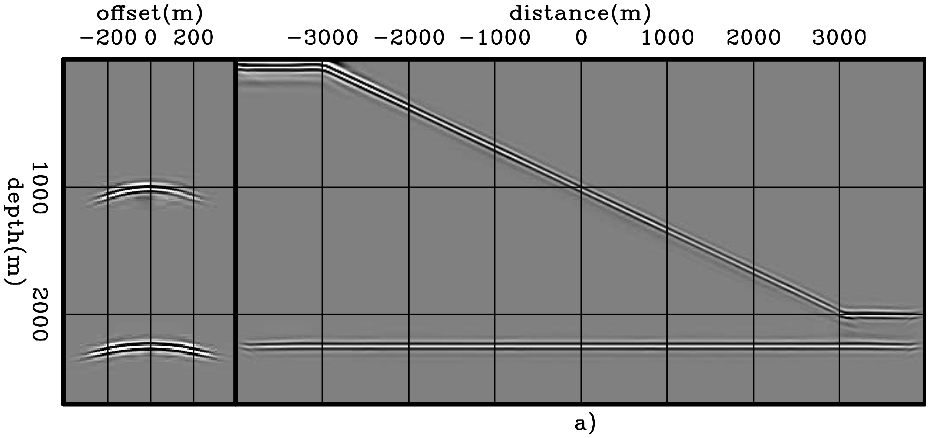

Figure 3.5: Areal-shot migration using the time-windowed imaging condition (equation 3.2). The reflector crosstalk is completely eliminated. ispew/. comb04

The efficacy of the time-windowed imaging condition for attenuating the reflector crosstalk is independent of the number of modeled events; however, it does depend on the distance between reflectors. This is illustrated using a smoothed Marmousi model example (Figure 3.6a). This model was input into one-way Born modeling, along with a 2D reflectivity derived from the true Marmousi velocity model, to generate 360 split-spread shot gathers with 6000 m maximum offset.

Shot-profile migration of the Born data was performed with a migration velocity approximately 5% slower than the modeling velocity for depth levels below the horizon shown in Figure 3.6b. Above this horizon, migration velocity is equal to the modeling velocity. All the left panels shown in this example are SODCIGs selected at $x = 5000m$. The right panel is the zero-subsurface-offset section. The background image contains 17 subsurface offsets 24 m apart, starting at -192 m. Four reflectors were selected to initiate the modeling of PERM wavefields. They were rotated according to the transformation described in Chapter 2. The background image and the selected reflectors are shown in Figures 3.7a-b, respectively, only for depths between 1500 and 3000 m. The rotated initial conditions for the modeling of source and receiver wavefields are shown in Figures 3.8a-b, respectively.

The horizontal distance between SODCIGs injected simultaneously into the modeling of one areal shot is 840 m, which means that 35 pairs of PERM wavefields are generated. This number corresponds to 1/ 10 of the original shot gathers. The spatial sampling interval is greater than the decorrelation distance, which in this case is 792 m. Hence, we do not expect crosstalk from unrelated SODCIGs.

PERM wavefields were modeled and collected at a depth of 1500 m. A pair of PERM wavefields are shown in Figure 3.9. These wavefields were migrated using the conventional (equation 2.12) and the time-windowed (equation 3.2) imaging conditions. The areal-shot migration using the conventional imaging condition is strongly contaminated with reflector crosstalk (Figure 3.10a). The areal-shot migration of PERM wavefields using the time-windowed imaging condition with a time-window length of 0.016 s successfully attenuated the reflector crosstalk in regions where reflectors are sufficiently separated (Figure 3.10b). However, as can be seen in the SODCIG in the left panel, some residual crosstalk from closely spaced reflectors still

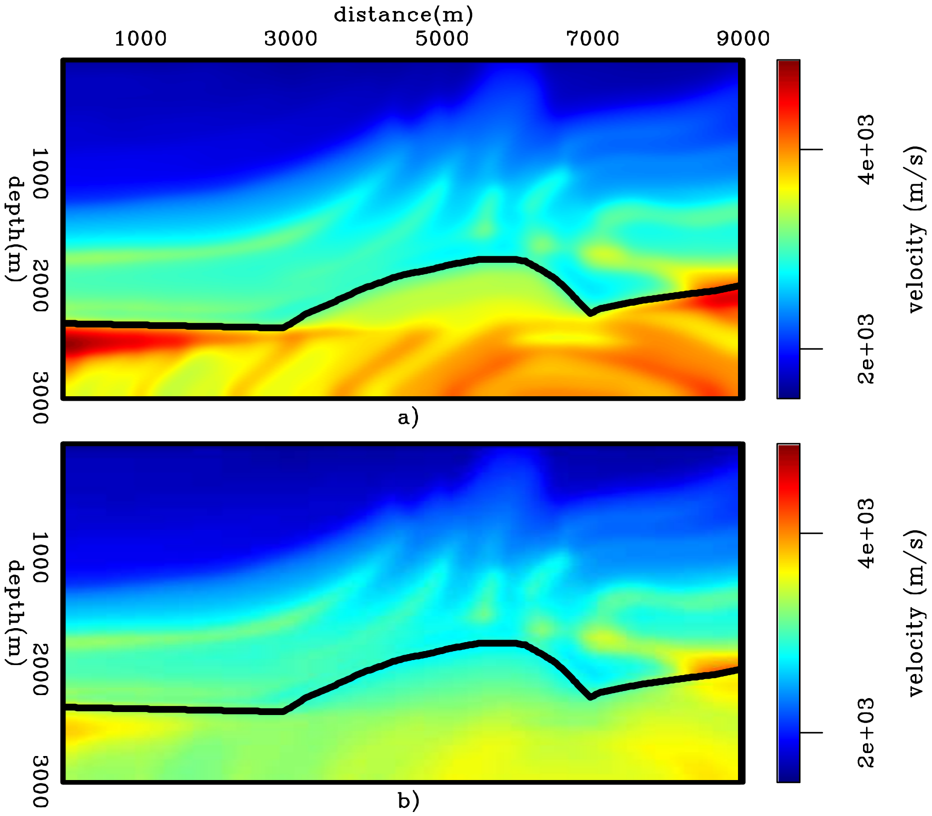

Figure 3.6: Velocity models for in the Marmousi example: a) Smooth velocity model used to model the Born data. b) Background velocity model used to migrate the Born data, and to model and migrate PERM data. ispew/. ismarm01

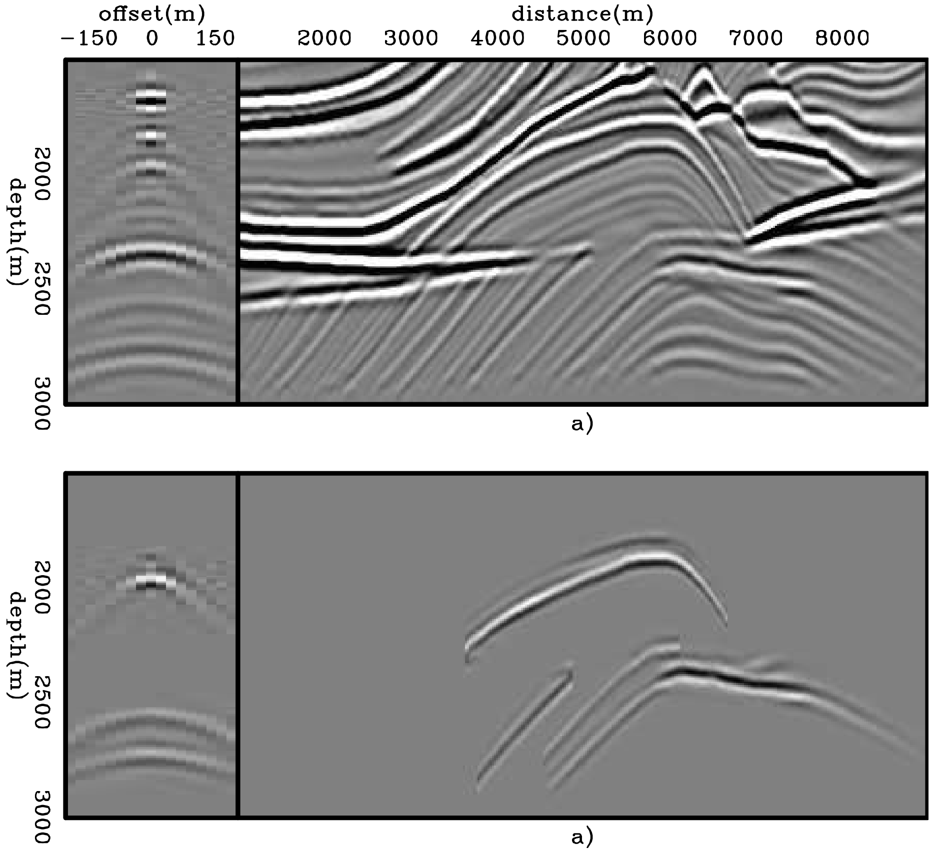

Figure 3.7: a) Pre-stack image computed with the background velocity model. b) Selected reflectors from the background image to perform modeling of wavefields. ispew/. ismarm02

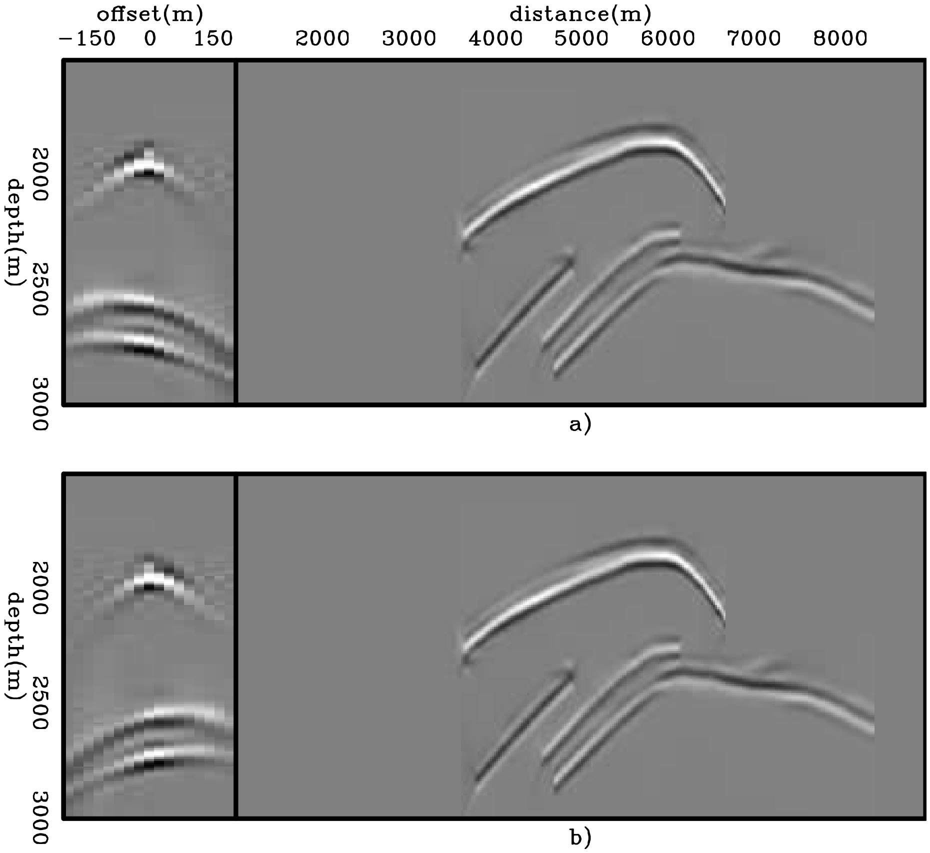

Figure 3.8: Rotated initial conditions for modeling: a) source wavefields, and b) receiver wavefields. ispew/. ismarm05

persists. This is because the time of wavefield propagation at which reflector crosstalk occurs is within the time window used for cross-correlation. This is easily seen by inserting the values for the local background velocity of 2540 m/s and the distance of 160 m between the two reflectors responsible for the reflector crosstalk into equation 3.1. The result, 0.125 s, is slightly smaller than the time-window length. Using a shorter time window could completely avoid crosstalk, but also could cause phase distortion.

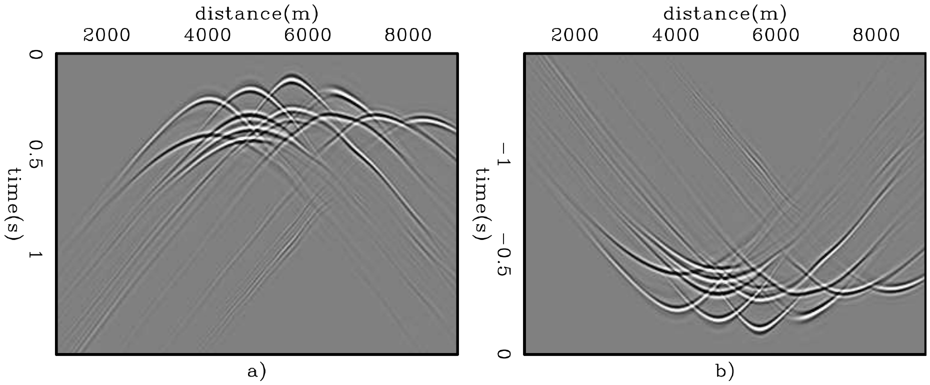

Figure 3.9: PERM wavefields for the Marmousi example: a) Receiver wavefield. b) Source wavefield. ispew/. ismarm03

The imaging principle states that the reflector image is formed at the zero time of wavefield propagation when the migration velocity is accurate. When the migration velocity is inaccurate, the focusing of the image departs from the zero time, and this can be potentially used to update the velocity model (Sava and Fomel, 2006; Yang and Sava, 2009). Depending on the magnitude of the velocity errors and the distance between reflectors, the use of the time-windowed imaging condition can corrupt the velocity information.

Next, we will see how phase-encoding the modeling experiments can attenuate crosstalk without the risk of affecting the velocity information.

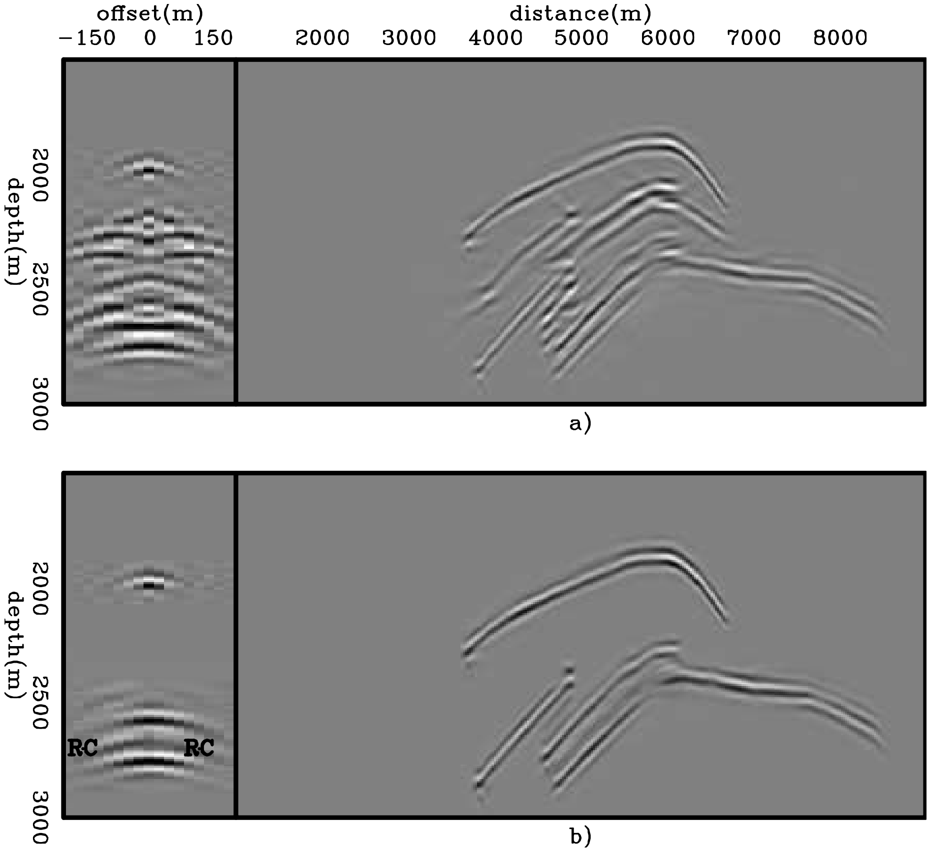

Figure 3.10: Pre-stack image computed with PERM wavefields and background velocity model using: a) the conventional imaging condition (equation 2.12), and b) the time-windowed imaging condition (equation 3.2). Reflector crosstalk is avoided when reflectors are sufficiently separated. However, some residual crosstalk is still present (RC). Notice the phase difference of the PERM image due to the squaring of the wavelet when compared to the windowed reflectors of Figure 3.7b. ispew/. ismarm04

Phase encoding the modeling experiments

Phase encoding is a well-established technique for decreasing the cost of seismic imaging by linearly combining the shot records, while maintaining the image quality (Schultz and Claerbout, 1978; Whitmore, 1995; Romero et al., 2000; Sun et al., 2002; Liu et al., 2006; Duquet and Lailly, 2006). Wavefields are usually phase-encoded in the data space simply because conventional wavefields are initiated and recorded at the contours of the reflection seismic problem. Therefore, the phase functions are parameterized according to the source index or source coordinates, which are data space parameters.

In a similar way, PERM wavefields initiated on the reflectors can also be phase-encoded. In this case, the phase functions are parameterized according to the model space coordinates and selected reflector, which are model space parameters. The parameterization of these phase functions characterizes the image-space phase encoding. The resulting wavefields are the image-space phase-encoded wavefields (ISPEW). We will see that randomly phase-encoding the modeling experiments enables us to have more than one reflector in the initial conditions and to use a spatial sampling period smaller than the decorrelation distance. This is not possible when using the time-windowed imaging condition strategy.

To describe how ISPEW are generated, let us slightly change the previous formulation of PERM to include the simultaneous modeling of more than one reflector. Horizontal reflectors are used for simplicity. For all the frequencies, modeling different random realizations $\mathbf{q}$ of pairs of ISPEW can be described by

$$\widetilde{D_I}(\boldsymbol{\xi}, \mathbf{q}, \omega) = \sum_{\mathbf{x}} \sum_{\mathbf{h}} G_0(\boldsymbol{\xi}, \mathbf{x} - \mathbf{h}, \omega) \widetilde{I}(\widehat{\mathbf{x}}, \mathbf{h}, \mathbf{q}, \omega), \tag{3.3}$$

and

$$\widetilde{U_I}(\boldsymbol{\xi}, \mathbf{q}, \omega) = \sum_{\mathbf{x}} \sum_{\mathbf{h}} G_0(\boldsymbol{\xi}, \mathbf{x} + \mathbf{h}, \omega) \widetilde{I}(\widehat{\mathbf{x}}, \mathbf{h}, \mathbf{q}, \omega). \tag{3.4}$$

The subscript of the Green's function G denotes propagation with a background velocity $s_0(\mathbf{x})$. The initial conditions $\widetilde{I}$ are computed as

$$\widetilde{I}(\widehat{\mathbf{x}}, \mathbf{h}, \mathbf{q}, \omega) = \sum_m \sum_j \delta(\widehat{\mathbf{x}} - m\Delta\mathbf{x})\beta(\widehat{\mathbf{x}}, j, \mathbf{q}, \omega)W_j(\widehat{\mathbf{x}}, \mathbf{h})I(\widehat{\mathbf{x}}, \mathbf{h}), \tag{3.5}$$

where W_j selects the reflector j by identifying and windowing it in the pre-stack image I, and $\beta(\widehat{\mathbf{x}}, j, \mathbf{q}, \omega)$ is a pseudo-random phase-encoding function defined as

$$\beta(\widehat{\mathbf{x}}, j, \mathbf{q}, \omega) = e^{i\epsilon(\widehat{\mathbf{x}}, j, \mathbf{q}, \omega)}, \tag{3.6}$$

with $\epsilon(\widehat{\mathbf{x}}, j, \mathbf{q}, \omega)$ usually being a uniformly distributed pseudo-random sequence with zero mean. Guerra and Biondi (2008a) also use Gold codes (Gold, 1967), sequences widely used in third- and fourth-generation cellphones, to phase-encode the modeling. The pseudo-random phase-encoding function causes the frequency components of the initial conditions to be randomly injected into the modeling. Source and receiver wavefields initiated at the same SODCIG and from the same reflector are equally encoded, whereas source and receiver wavefields initiated at different SODCIGs and from the different reflectors have different codes assigned to them.

The recursive downward propagation with a different velocity $s_1(\mathbf{x})$ is performed according to

$$\widetilde{D_I}(\mathbf{x}, \omega, \mathbf{q}) = \sum_{\boldsymbol{\xi}} G_1^*(\boldsymbol{\xi}, \mathbf{x}, \omega)\widetilde{D_I}(\boldsymbol{\xi}\omega, \mathbf{q}), \tag{3.7}$$

and

$$\widetilde{U_I}(\mathbf{x}, \omega, \mathbf{q}) = \sum_{\boldsymbol{\xi}} G_1^*(\boldsymbol{\xi}, \mathbf{x}, \omega)\widetilde{U_I}(\boldsymbol{\xi}\omega, \mathbf{q}). \tag{3.8}$$

The lateral shifts of the wavefields for the multi-offset imaging condition are represented by

$$\begin{aligned}\widetilde{D_I}(\mathbf{x}-\mathbf{h},\omega,\mathbf{q}) \;&=\; \sum_{\boldsymbol{\xi}}\sum_{\mathbf{x}'}\sum_{\mathbf{h}'}\sum_{m}\sum_{j} G_1^*(\boldsymbol{\xi},\mathbf{x}-\mathbf{h},\omega)G_0(\boldsymbol{\xi},\mathbf{x}'-\mathbf{h}',\omega)\\ &\times\; \delta(\widehat{\mathbf{x}}-m\Delta\mathbf{x})\beta(\widehat{\mathbf{x}},j,\mathbf{q},\omega)W_j(\widehat{\mathbf{x}},\mathbf{h}')I(\widehat{\mathbf{x}},\mathbf{h}'),\end{aligned} \tag{3.9}$$

and

$$\begin{aligned}\widetilde{U_I}(\mathbf{x}+\mathbf{h},\omega,\mathbf{q}) \;&=\; \sum_{\boldsymbol{\xi}}\sum_{\mathbf{x}'}\sum_{\mathbf{h}'}\sum_{m}\sum_{j} G_1^*(\boldsymbol{\xi},\mathbf{x}+\mathbf{h},\omega)G_0(\boldsymbol{\xi},\mathbf{x}'+\mathbf{h}',\omega)\\ &\times\; \delta(\widehat{\mathbf{x}}-m\Delta\mathbf{x})\beta(\widehat{\mathbf{x}},j,\mathbf{q},\omega)W_j(\widehat{\mathbf{x}},\mathbf{h}')I(\widehat{\mathbf{x}},\mathbf{h}'),\end{aligned} \tag{3.10}$$

Applying the cross-correlation imaging condition to the wavefields of equations 3.9 and 3.10 and summing over frequency and over realizations gives

$$\begin{aligned}\widetilde{I}_I(\mathbf{x},\mathbf{h}) \;&= \sum_{\omega}\sum_{\boldsymbol{\xi}'}\sum_{\mathbf{x}'}\sum_{\mathbf{h}'}\sum_{\boldsymbol{\xi}''}\sum_{\mathbf{x}''}\sum_{\mathbf{h}''}\sum_{\mathbf{q}}\sum_{m}\sum_{n}\sum_{j}\sum_{l}\\ &\times G_0^*(\boldsymbol{\xi}',\mathbf{x}'-\mathbf{h}',\omega)G_1(\boldsymbol{\xi}',\mathbf{x}-\mathbf{h},\omega)G_1^*(\boldsymbol{\xi}'',\mathbf{x}+\mathbf{h},\omega)G_0(\boldsymbol{\xi}'',\mathbf{x}''+\mathbf{h}'',\omega)\\ &\times\delta(\widehat{\mathbf{x}}-m\Delta\mathbf{x})\delta(\widehat{\mathbf{x}}-n\Delta\mathbf{x})\beta(\widehat{\mathbf{x}},j,\mathbf{q},\omega)\beta(\widehat{\mathbf{x}},l,\mathbf{q},\omega)\\ &\times W_j(\widehat{\mathbf{x}},\mathbf{h}')W_j(\widehat{\mathbf{x}},\mathbf{h}'')I(\widehat{\mathbf{x}},\mathbf{h}')I(\widehat{\mathbf{x}},\mathbf{h}''),\end{aligned} \tag{3.11}$$

which can be recast as

$$\begin{aligned}\widetilde{I}_I(\mathbf{x},\mathbf{h}) \;&= I_{\Delta x,j}(\mathbf{x},\mathbf{h})\\ &+\sum_{\omega}\sum_{\boldsymbol{\xi}'}\sum_{\mathbf{x}'}\sum_{\mathbf{h}'}\sum_{\boldsymbol{\xi}''}\sum_{\mathbf{x}''}\sum_{\mathbf{h}''}\sum_{\mathbf{q}}\sum_{m\neq n}\sum_{j\neq l}\\ &\times G_0^*(\boldsymbol{\xi}',\mathbf{x}'-\mathbf{h}',\omega)G_1(\boldsymbol{\xi}',\mathbf{x}-\mathbf{h},\omega)G_1^*(\boldsymbol{\xi}'',\mathbf{x}+\mathbf{h},\omega)G_0(\boldsymbol{\xi}'',\mathbf{x}''+\mathbf{h}'',\omega)\\ &\times\delta(\widehat{\mathbf{x}}-m\Delta\mathbf{x})\delta(\widehat{\mathbf{x}}-n\Delta\mathbf{x})\beta(\widehat{\mathbf{x}},j,\mathbf{q},\omega)\beta(\widehat{\mathbf{x}},l,\mathbf{q},\omega)\\ &\times W_j(\widehat{\mathbf{x}},\mathbf{h}')W_l(\widehat{\mathbf{x}},\mathbf{h}'')I(\widehat{\mathbf{x}},\mathbf{h}')I(\widehat{\mathbf{x}},\mathbf{h}'').\end{aligned} \tag{3.12}$$

The first term in the right-hand side of equation 3.12 is the desired image we would obtain by modeling and migrating PERM wavefields initiated at isolated reflectors of isolated SODCIGs and is the result of the cross-correlation of encoded wavefields with $m = n$ and $j = l$. The second term represents the attenuated crosstalk, which includes the attenuated reflector crosstalk and the attenuated crosstalk from unrelated SODCIGs. Crosstalk attenuation is achieved by the cross-correlation of quasi-orthogonal sequences, whose values are small if compared with the zero lag of the auto-correlation. Ideally, the attenuated crosstalk is unstructured and occurs as speckled noise throughout the image.

Theoretically, according to the law of large numbers, if the number of random realizations is sufficiently large, the crosstalk term is negligible. When summing migration results of different random realizations, reflectors constructively interfere, whereas crosstalk destructively interferes. In practice, a satisfactory crosstalk attenuation is achieved using a small number of realizations.

We use the Marmousi data to illustrate the generation and migration of ISPEW. The rotated SODCIGs of Figure 3.8 are phase-encoded to generate the initial conditions. We phase-encode the SODCIGs as well as the reflectors. The sampling period is 264 m, which roughly corresponds to $1/3$ of the decorrelation distance. We compute four random realizations, corresponding to 44 pairs of ISPEW. Two pairs of ISPEW from different random realizations initiated at the same SODCIGs are shown in Figure 3.11.

The areal-shot migration of ISPEW is shown in Figure 3.12. At the top, we see the result of migrating 44 wavefields from the four random realizations. At the bottom, we see the result of migrating 11 wavefields from one single random realization. Although the two images have a comparable quality, more realizations give a cleaner image.

To analyze the quality of the kinematic information, we compute residual-moveout panels from images computed with the original data (Figure 3.13a), with PERM wavefields and the time-windowed imaging condition (Figure 3.13b), with all four random realizations (Figure 3.13c), and with a single realization (Figure 3.13d). The residual moveout information in the four panels is very similar. However, the cost of obtaining it widely varies. For instance, migrating one random realization of ISPEW is approximately 30 times faster than migrating all the 360 original shots. Using

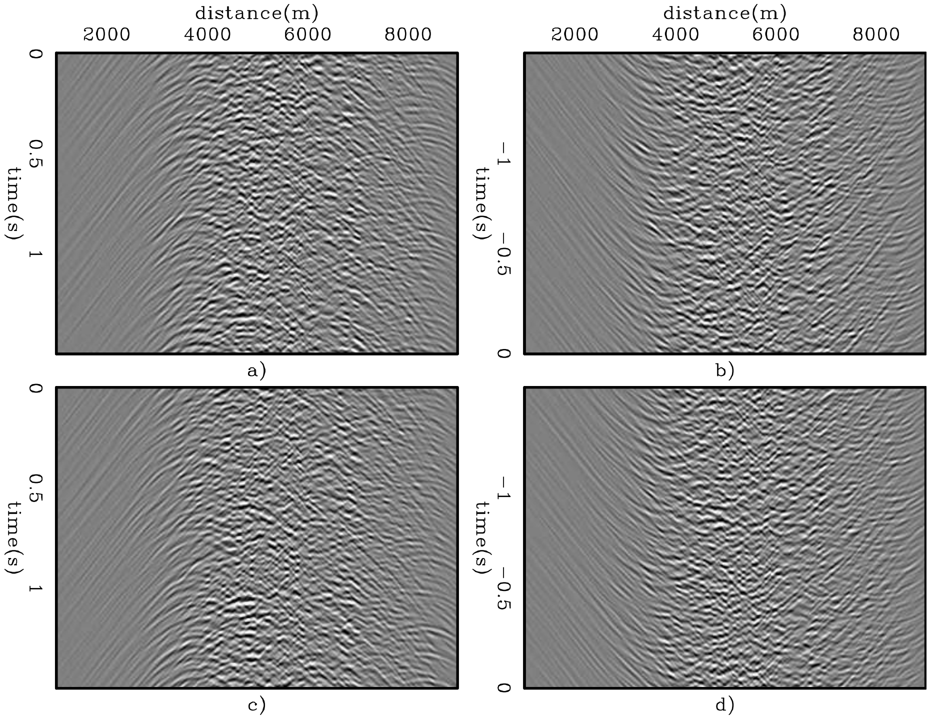

Figure 3.11: ISPEW from different random realizations initiated at the same SOD-CIGs for the Marmousi example: a,c) Receiver wavefields. b,d) Source wavefields. ispew/. ismarm06

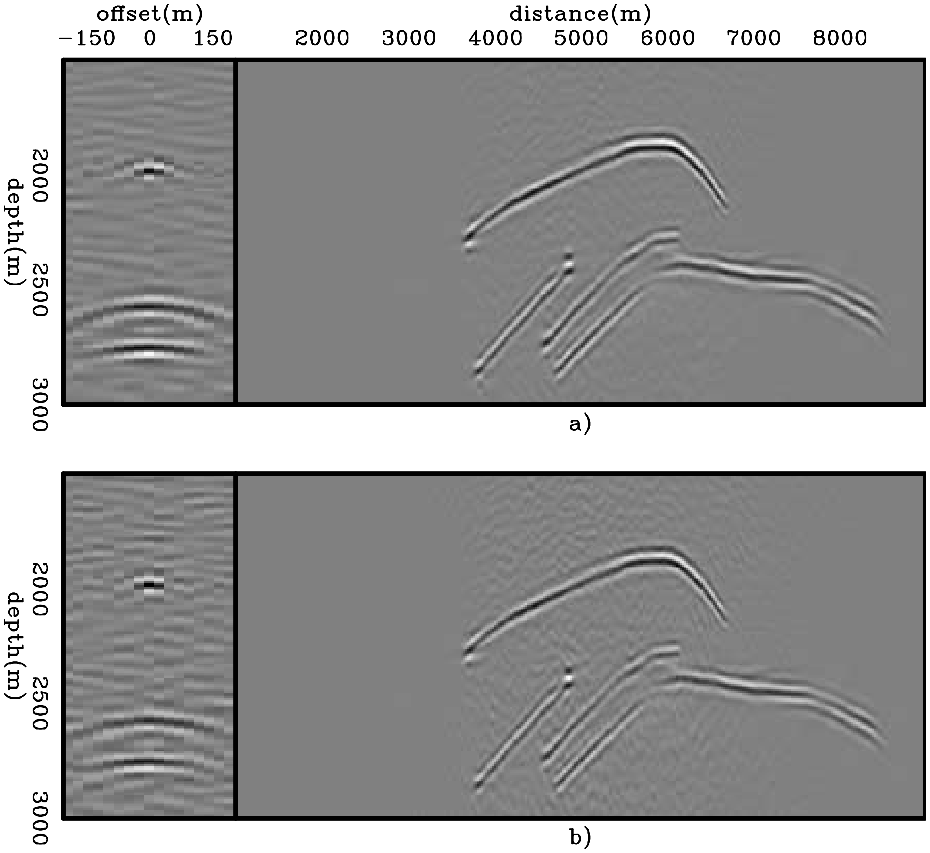

Figure 3.12: Pre-stack images computed with: a) Four random realizations of ISPEW, and b) a single random realization. ispew/. ismarm07

the same wavefields, computing the gradient of the objective function of migration-velocity analysis by wavefield-extrapolation can be 60 times faster. This difference in performance is even more dramatic when we consider that several iterations of migrations and gradient computations are performed during migration velocity optimization by wavefield-extrapolation. In Chapter 4, we will see the usefulness of ISPEW in migration velocity optimization by wavefield-extrapolation.

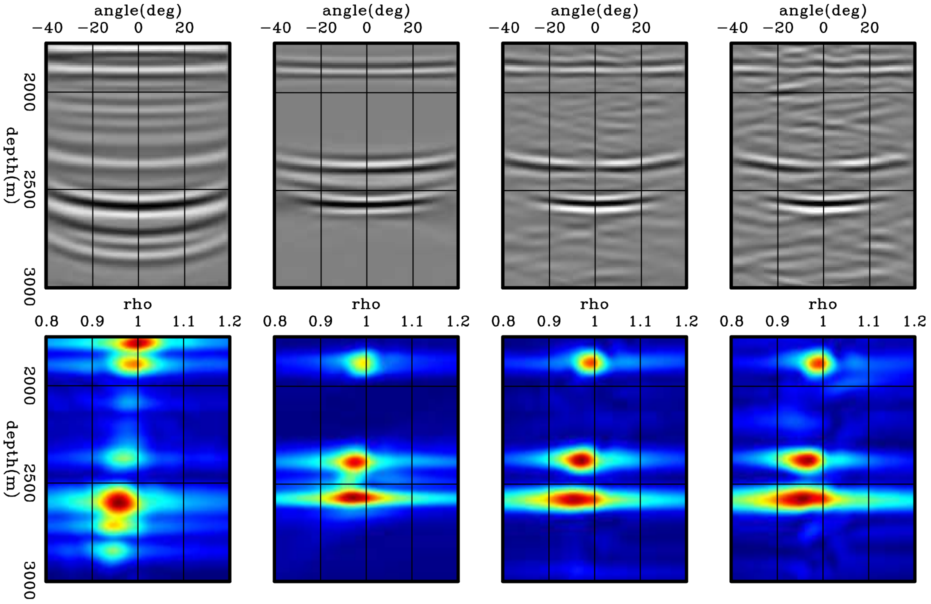

Figure 3.13: ADCIGs (top) and ρ-panels (bottom) corresponding to images computed by: a) Shot-profile migration of 360 shot gathers, b) areal-shot migration of 35 PERM wavefields using the time-windowed imaging condition, c) areal-shot migration of 44 ISPEW corresponding to four random realizations, and d) areal-shot migration of 11 ISPEW corresponding to a single random realization. The moveout information is basically the same. ispew/. ismarm08

CONCLUSIONS

In this chapter, PERM was used to model wavefields without observing the decorrelation distance between SODCIGs and using more than one reflector in the initial conditions. Doing this generates two types of crosstalk are generated: the reflector crosstalk and the crosstalk from unrelated SODCIGs. The reflector crosstalk is generated when performing the cross-correlation of the wavefields in time, whereas the crosstalk from unrelated SODCIGs is generated when performing the cross-correlation of the wavefields in space.

Since reflectors are imaged at time zero of wavefield propagation, an effective strategy to almost completely attenuate the reflector crosstalk is to cross-correlate wavefields only within a small window around the zero time of wavefield propagation. To apply the time-windowed imaging condition, the frequency slices of the wavefields must be stored, which can be impractical for 3D applications. This strategy does not avoid the crosstalk from unrelated SODCIGs and, therefore, the decorrelation distance has to be used. In addition, in the presence of velocity inaccuracy, this strategy can corrupt the velocity information.

A more general method for attenuating crosstalk, independent of its origin, is to phase-encode the modeling experiments. Since the phase-encoding sequences are defined as a function of image parameters, namely spatial coordinates and reflector index, the wavefields are called image-space phase-encoded wavefields – ISPEW. We exemplified the usefulness of ISPEW with an example using the Marmousi data. The migrated images using these wavefields have kinematic information similar to that obtained with shot-profile migration for the selected reflectors, but at a much lower cost. This was illustrated using residual moveout panels. In the next chapter, we will see that they also provide a similar gradient for the migration-velocity analysis by wavefield-extrapolation objective function.

Chapter 4

MVA using image-space generalized sources

The theory of migration-velocity analysis by wavefield extrapolation has already been developed using survey-sinking migration and also using shot-profile migration. In this chapter, I extend the theory of migration-velocity analysis by wavefield extrapolation using areal-shot migration, more specifically using wavefields computed in the image-space generalized-source domain. In this new domain, PERM wavefields and ISPEW are used to compute the velocity updates. These wavefields allow fast velocity updates compared to when conventional wavefields are used, like in shot-profile migration. The small data size of image-space generalized-source wavefields in addition to their inherent capability for being used in a target-oriented manner are the main causes for the computational efficiency. Moreover, the use of these wavefields enable us to incorporate well-established strategies in migration-velocity analysis by ray-methods, such as horizon-based tomography and possibly grid-based tomography, into migration-velocity analysis by wavefield extrapolation. This new feature gives more flexibility to migration-velocity analysis by wavefield extrapolation and can improve the convergence to an optimal velocity. I illustrate the use of image-space generalized wavefields in velocity optimization with 2D examples.

INTRODUCTION

Wave-equation tomography aims at solving for earth models that explain observed seismograms under some norm. There are two main categories, depending on the domain in which the objective function is computed. In one category, known as waveform inversion, the objective function is minimized in the data space where data modeled with the current model parameters data are compared with the recorded seismograms (Lailly, 1983; Tarantola, 1987; Woodward, 1992; Virieux and Operto, 2009).

In the other category, here called image-space wave-equation tomography (ISWET), the objective function is minimized in the image space. Two variants of ISWET are wave-equation migration velocity analysis (WEMVA) (Sava and Biondi, 2004a,b) and differential semblance velocity analysis (DSVA) (Shen, 2004; Shen and Symes, 2008).

Despite their differences, those two categories are linked by the concept of extended modeling (Symes, 2008). Symes (2008) showed that ISWET can be regarded as a solution method for the partially linearized waveform inversion. Whereas ISWET solves for the long-wavelength components of the slowness model, assuring global convergence, waveform inversion computes the short-wavelength components, providing accuracy.

Like waveform inversion, ISWET is a computationally demanding process. This computational cost is commonly decreased by using generalized sources (Shen and Symes, 2008; Tang et al., 2008). Because wavefield propagation is a linear process, generalized sources are computed by linearly combining source wavefields and receiver wavefields, using phase-encoding techniques (Whitmore, 1995; Romero et al., 2000). In particular, Guerra et al. (2009b) used phase-encoding modeling in the image space to synthesize generalized source functions that drastically decrease the cost of DSVA.

WEMVA and DVSA seek the optimal slowness by driving an image perturbation to a minimum. However, they differ in the way the image perturbation is computed and, consequently, in the numerical optimization scheme applied. As Biondi (2008) points out, WEMVA is not easily automated. The image perturbation is computed by the linearized residual prestack-depth migration (Sava and Biondi, 2004a), which uses a manually picked residual-moveout parameter. Since the perturbed image computed with the linearized residual prestack-depth migration is consistent with the application of the forward wave-equation tomographic operator, WEMVA can be solved using linear conjugate-gradient methods. Linear iterations drive the the objective function to a minimum for the current residual-moveout parameter field, which gives the current velocity perturbation. The corresponding velocity solution is used to compute a new image whose focusing will be evaluated by a new run of residual-moveout parameter interpretation.

In DSVA, the perturbed image is computed by applying the fully automated differential-semblance operator (DSO) to SODCIGs or ADCIGs. When applied to SODCIGs, DSO minimizes the energy not focused at zero-offset. When applied to ADCIGs, DSO minimizes energy of the reflectors departing from flatness. Although DSO easily automates ISWET, it produces perturbed images that do not present the depth phase-shift introduced by the forward one-way ISWET operator. Moreover, the amplitude behavior of the perturbed image computed with DSO greatly differs from that of the perturbed image computed with the forward one-way ISWET operator. These differences, prevents the use of linear conjugate-gradient methods and, therefore, the objective function computed with DSO is typically minimized by nonlinear optimization methods.

IMAGE-SPACE WAVE-EQUATION TOMOGRAPHY

Image-space wave-equation tomography is a non-linear inverse problem that tries to find an optimal background slowness that minimizes the residual field, $\mathbf{\Delta I}$, defined in the image space. The residual field is derived from the background image, $\mathbf{I}$, which is computed with a background slowness (or the current estimate of the slowness). The residual field measures the correctness of the background slowness; its minimum (under some norm, e.g. ℓ_2) is achieved when a correct background slowness has been used for migration. There are many choices of the residual field, such as residual moveout in the Angle-Domain Common-Image Gathers (ADCIGs), differential semblance in the ADCIGs, reflection-angle stacking power (in which case we have to maximize the residual field, or minimize the negative stacking power), etc.. Here we follow a definition similar to that in Biondi (2008), and define a general form of the residual field as follows:

$$\boldsymbol{\Delta}\mathbf{I} = \mathbf{I} - \mathbf{F}(\mathbf{I}), \tag{4.1}$$

where $\mathbf{F}$ is a focusing operator, which measures the focusing of the migrated image. For example, in the Differential Semblance Optimization (DSO) method (Shen, 2004), the focusing operator takes the following form:

$$\mathbf{F}(\mathbf{I}) = (\mathbf{1} - \mathbf{O})\,\mathbf{I}, \tag{4.2}$$

where $\mathbf{1}$ is the identity operator and $\mathbf{O}$ is the DSO operator either in the subsurface offset domain or in the angle domain (Shen, 2004). The subsurface-offset-domain DSO focuses the energy at zero offset, whereas the angle-domain DSO flattens the ADCIGs.

In the wave-equation migration velocity analysis (WEMVA) method (**?**), the focusing operator is the linearized residual migration operator defined as follows:

$$\mathbf{F}(\mathbf{I}) = \mathbf{R}[\rho]\mathbf{I} \approx \mathbf{I} + \mathbf{K}[\Delta\rho]\mathbf{I}, \tag{4.3}$$

where ρ is the ratio between the background slowness $\widehat{\mathbf{s}}$ and the true slowness $\mathbf{s}$, and $\Delta\rho = 1 - \rho = 1 - \frac{\widehat{\mathbf{s}}}{\mathbf{s}}$; $\mathbf{R}[\rho]$ is the residual migration operator (Sava, 2003), and $\mathbf{K}[\Delta\rho]$ is the differential residual migration operator defined as follows (Sava and Biondi, 2004a,b):

$$\mathbf{K}[\Delta\rho] = \Delta\rho\,\left.\frac{\partial\mathbf{R}[\rho]}{\partial\rho}\right|_{\rho=1}. \tag{4.4}$$

The linear operator $\mathbf{K}[\Delta\rho]$ applies different phase rotations to the image for different reflection angles and geological dips (Biondi, 2008).

In general, if we choose ℓ_2 norm, the tomography objective function to minimize can be written as follows:

$$J = \frac{1}{2}||\mathbf{\Delta I}||_2 = \frac{1}{2}||\mathbf{I} - \mathbf{F}(\mathbf{I})||_2, \tag{4.5}$$

where $||\cdot||_2$ stands for the ℓ_2 norm. Gradient-based optimization techniques such as the quasi-Newton method and the conjugate gradient method can be used to minimize the objective function J. The gradient of J with respect to the slowness $\mathbf{s}$ reads as follows:

$$\nabla J = \Re\left(\left(\frac{\partial \mathbf{I}}{\partial \mathbf{s}} - \frac{\partial \mathbf{F}(\mathbf{I})}{\partial \mathbf{s}}\right)' (\mathbf{I} - \mathbf{F}(\mathbf{I}))\right), \tag{4.6}$$

where $\Re$ denotes taking the real part of a complex value and $'$ denotes the adjoint. For the DSO method, the linear operator $\mathbf{O}$ is independent of the slowness, so we have

$$\frac{\partial \mathbf{F}(\mathbf{I})}{\partial \mathbf{s}} = (\mathbf{1} - \mathbf{O})\frac{\partial \mathbf{I}}{\partial \mathbf{s}}. \tag{4.7}$$

Substituting Equations 4.2 and 4.7 into Equation 4.6 and evaluating the gradient at a background slowness yields

$$\nabla J_{\text{DSO}} = \Re\left(\left(\left.\frac{\partial \mathbf{I}}{\partial \mathbf{s}}\right|_{\mathbf{s}=\widehat{\mathbf{s}}}\right)' \mathbf{O}'\mathbf{O}\widehat{\mathbf{I}}\right), \tag{4.8}$$

where $\widehat{\mathbf{I}}$ is the background image computed using the background slowness $\widehat{\mathbf{s}}$.

For the WEMVA method, the gradient is slightly more complicated, because in this case, the focusing operator is also dependent on the slowness $\mathbf{s}$. However, one can simplify it by assuming that the focusing operator is applied on the background image $\widehat{\mathbf{I}}$ instead of $\mathbf{I}$, and $\widehat{\Delta\rho}$ is also picked from the background image $\widehat{\mathbf{I}}$, that is

$$\mathbf{F}(\widehat{\mathbf{I}}) = \widehat{\mathbf{I}} + \mathbf{K}[\widehat{\Delta\rho}]\widehat{\mathbf{I}}. \tag{4.9}$$

With these assumptions, we get the "classic" WEMVA gradient as follows:

$$\nabla J_{\text{WEMVA}} = \Re\left(-\left(\left.\frac{\partial \mathbf{I}}{\partial \mathbf{s}}\right|_{\mathbf{s}=\widehat{\mathbf{s}}}\right)' \mathbf{K}[\widehat{\Delta\rho}]\widehat{\mathbf{I}}\right) \tag{4.10}$$

The complete WEMVA gradient without the above assumptions can also be derived following the method described by Biondi (2008).

No matter which gradient we choose to back-project the slowness perturbation, we have to evaluate the adjoint of the linear operator $\left.\frac{\partial \mathbf{I}}{\partial \mathbf{s}}\right|_{\mathbf{s}=\widehat{\mathbf{s}}}$, which defines a linear mapping from the slowness perturbation $\mathbf{\Delta s}$ to the image perturbation $\mathbf{\Delta I}$. This is easy to see by expanding the image $\mathbf{I}$ around the background slowness $\widehat{\mathbf{s}}$ as follows:

$$\mathbf{I} = \widehat{\mathbf{I}} + \left.\frac{\partial \mathbf{I}}{\partial \mathbf{s}}\right|_{\mathbf{s}=\widehat{\mathbf{s}}} (\mathbf{s} - \widehat{\mathbf{s}}) + \cdots , \tag{4.11}$$

Keeping only the zero and first order terms, we get the linear operator $\left.\frac{\partial \mathbf{I}}{\partial \mathbf{s}}\right|_{\mathbf{s}=\widehat{\mathbf{s}}}$ as follows:

$$\mathbf{\Delta I} = \left.\frac{\partial \mathbf{I}}{\partial \mathbf{s}}\right|_{\mathbf{s}=\widehat{\mathbf{s}}} \mathbf{\Delta s} = \mathbf{T}\mathbf{\Delta s}, \tag{4.12}$$

where $\mathbf{\Delta I} = \mathbf{I} - \widehat{\mathbf{I}}$ and $\mathbf{\Delta s} = \mathbf{s} - \widehat{\mathbf{s}}$. $\mathbf{T} = \left.\frac{\partial \mathbf{I}}{\partial \mathbf{s}}\right|_{\mathbf{s}=\widehat{\mathbf{s}}}$ is the wave-equation tomographic operator. The tomographic operator can be evaluated either in the source and receiver domain (**?**) or in the shot-profile domain (Shen, 2004). In next section we follow an approach similar to that discussed by Shen (2004) and review the forward and adjoint tomographic operator in the shot-profile domain. In the subsequent sections, we generalize the expression of the tomographic operator to the generalized source domain.

THE TOMOGRAPHIC OPERATOR IN THE SHOT-PROFILE DOMAIN

For the conventional shot-profile migration, both source and receiver wavefields are downward continued with the following one-way wave equations (Claerbout, 1971b):

$$\left\{ \begin{array}{l} \left(\frac{\partial}{\partial z} + i\sqrt{\omega^2 s^2(\mathbf{x}) - |\mathbf{k}|^2}\right) D(\mathbf{x}, \mathbf{x}_s, \omega) = 0 \\ D(x, y, z = 0, \mathbf{x}_s, \omega) = \overline{f_s(\omega)\delta(\mathbf{x} - \mathbf{x}_s)} \end{array} \right. , \tag{4.13}$$

and

$$\left\{ \begin{array}{l} \left(\frac{\partial}{\partial z} + i\sqrt{\omega^2 s^2(\mathbf{x}) - |\mathbf{k}|^2}\right) U(\mathbf{x}, \mathbf{x}_s, \omega) = 0 \\ U(x, y, z = 0, \mathbf{x}_s, \omega) = Q(x, y, z = 0, \mathbf{x}_s, \omega) \end{array} \right. , \tag{4.14}$$

where the overline stands for complex conjugate; $D(\mathbf{x}, \mathbf{x}_s, \omega)$ is the source wavefield for a single frequency ω at image point $\mathbf{x} = (x, y, z)$ with the source located at $\mathbf{x}_s = (x_s, y_s, 0)$; $U(\mathbf{x}, \mathbf{x}_s, \omega)$ is the receiver wavefield for a single frequency ω at image point $\mathbf{x}$ for the source located at $\mathbf{x}_s$; $s(\mathbf{x})$ is the slowness at $\mathbf{x}$; $\mathbf{k} = (k_x, k_y)$ is the spatial wavenumber vector; $f_s(\omega)$ is the frequency dependent source signature, and $\overline{f_s(\omega)\delta(\mathbf{x} - \mathbf{x}_s)}$ defines the point source function at $\mathbf{x}_s$, which serves as the boundary condition of Equation 4.13. $Q(x, y, z = 0, \mathbf{x}_s, \omega)$ is the recorded shot gather for the shot located at $\mathbf{x}_s$, which serves as the boundary condition of Equation 4.14. To produce the image, the following cross-correlation imaging condition is used:

$$I(\mathbf{x}, \mathbf{h}) = \sum_{\mathbf{x}_s} \sum_{\omega} D(\mathbf{x} - \mathbf{h}, \mathbf{x}_s, \omega) U(\mathbf{x} + \mathbf{h}, \mathbf{x}_s, \omega), \tag{4.15}$$

where $\mathbf{h} = (h_x, h_y, h_z)$ is the subsurface half offset.

The perturbed image can be derived by a simple application of the chain rule to

Equation 4.15:

$$\begin{aligned} \Delta I(\mathbf{x},\mathbf{h}) &= \sum_{\mathbf{x}_s}\sum_{\omega}\Big(\Delta D(\mathbf{x}-\mathbf{h},\mathbf{x}_s,\omega)\widehat{U}(\mathbf{x}+\mathbf{h},\mathbf{x}_s,\omega)+ \\ &\qquad \widehat{D}(\mathbf{x}-\mathbf{h},\mathbf{x}_s,\omega)\Delta U(\mathbf{x}+\mathbf{h},\mathbf{x}_s,\omega)\Big)\,, \end{aligned} \tag{4.16}$$

where $\widehat{D}(\mathbf{x}-\mathbf{h},\mathbf{x}_s,\omega)$ and $\widehat{U}(\mathbf{x}+\mathbf{h},\mathbf{x}_s,\omega)$ are the background source and receiver wavefields computed with the background slowness $\widehat{s}(\mathbf{x})$; $\Delta D(\mathbf{x}-\mathbf{h},\mathbf{x}_s,\omega)$ and $\Delta U(\mathbf{x}+\mathbf{h},\mathbf{x}_s,\omega)$ are the perturbed source wavefield and perturbed receiver wavefield, which are the results of the slowness perturbation $\Delta s(\mathbf{x})$. The perturbed source and receiver wavefields satisfy the following one-way wave equations, which are linearized with respect to slowness (see Appendix A for derivations):

$$\begin{cases} \left(\frac{\partial}{\partial z}+i\sqrt{\omega^2\widehat{s}^2(\mathbf{x})-|\mathbf{k}|^2}\right)\Delta D(\mathbf{x},\mathbf{x}_s,\omega) = \frac{-i\omega\Delta s(\mathbf{x})}{\sqrt{1-\frac{|\mathbf{k}|^2}{\omega^2\widehat{s}^2(\mathbf{x})}}}\widehat{D}(\mathbf{x},\mathbf{x}_s,\omega) \\ \Delta D(x,y,z=0,\mathbf{x}_s,\omega)=0 \end{cases}, \tag{4.17}$$

and

$$\begin{cases} \left(\frac{\partial}{\partial z}+i\sqrt{\omega^2\widehat{s}^2(\mathbf{x})-|\mathbf{k}|^2}\right)\Delta U(\mathbf{x},\mathbf{x}_s,\omega) = \frac{-i\omega\Delta s(\mathbf{x})}{\sqrt{1-\frac{|\mathbf{k}|^2}{\omega^2\widehat{s}^2(\mathbf{x})}}}\widehat{U}(\mathbf{x},\mathbf{x}_s,\omega) \\ \Delta U(x,y,z=0,\mathbf{x}_s,\omega)=0 \end{cases}. \tag{4.18}$$

Recursively solving Equations 4.17 and 4.18 gives us the perturbed source and receiver wavefields. The perturbed source and receiver wavefields are then used in Equation 4.16 to generate the perturbed image $\Delta I(\mathbf{x},\mathbf{h})$, where the background source and receiver wavefields are precomputed by recursively solving Equations 4.13 and 4.14 with a background slowness $\widehat{s}(\mathbf{x})$. Appendix B gives a more detailed matrix representation of how to evaluate the forward tomographic operator $\mathbf{T}$.

To evaluate the adjoint tomographic operator $\mathbf{T}'$, we first apply the adjoint of the imaging condition in Equation 4.16 to get the perturbed source and receiver wavefields

$\Delta D(\mathbf{x}, \mathbf{x}_s, \omega)$ and $\Delta U(\mathbf{x}, \mathbf{x}_s, \omega)$ as follows:

$$\begin{aligned} \Delta D(\mathbf{x}, \mathbf{x}_s, \omega) &= \sum_{\mathbf{h}} \Delta I(\mathbf{x}, \mathbf{h}) \overline{\widehat{U}(\mathbf{x}+\mathbf{h}, \mathbf{x}_s, \omega)}, \qquad (4.19) \\ \Delta U(\mathbf{x}, \mathbf{x}_s, \omega) &= \sum_{\mathbf{h}} \Delta I(\mathbf{x}, \mathbf{h}) \overline{\widehat{D}(\mathbf{x}-\mathbf{h}, \mathbf{x}_s, \omega)}. \qquad (4.20) \end{aligned}$$

Then we solve the adjoint equations of Equations 4.17 and 4.18 to get the slowness perturbation $\Delta s(\mathbf{x})$. Again, in order to solve the adjoint equations of Equations 4.17 and 4.18, the background source wavefield $\widehat{D}(\mathbf{x}, \mathbf{x}_s, \omega)$ and the background receiver wavefield $\widehat{U}(\mathbf{x}, \mathbf{x}_s, \omega)$ have to be computed in advance. Appendix C gives a more detailed matrix representation of how to evaluate the adjoint tomographic operator $\mathbf{T}'$.

Image-space encoded wavefields

From Equation **??**, the perturbed image is easily obtained as follows:

$$\begin{aligned} \Delta I_{\mathrm{me}}(\mathbf{x}, \mathbf{h}) = \sum_{\mathbf{p}_m} \sum_{\omega} \Big(& \Delta \widetilde{D}(\mathbf{x}-\mathbf{h}, \mathbf{p}_m, \omega) \widehat{\widetilde{U}}(\mathbf{x}+\mathbf{h}, \mathbf{p}_m, \omega) + \\ & \widehat{\widetilde{D}}(\mathbf{x}-\mathbf{h}, \mathbf{p}_m, \omega) \Delta \widetilde{U}(\mathbf{x}+\mathbf{h}, \mathbf{p}_m, \omega) \Big), \qquad (4.21) \end{aligned}$$

where $\widehat{\widetilde{D}}(\mathbf{x}, \mathbf{p}_m, \omega)$ and $\widehat{\widetilde{U}}(\mathbf{x}, \mathbf{p}_m, \omega)$ are the image-space encoded background source and receiver wavefields; $\Delta \widetilde{D}(\mathbf{x}, \mathbf{p}_m, \omega)$ and $\Delta \widetilde{U}(\mathbf{x}, \mathbf{p}_m, \omega)$ are the perturbed source and receiver wavefields in the image-space phase-encoding domain, which satisfy the perturbed one-way wave equations defined by Equations 4.17 and 4.18. The tomographic operator $\mathbf{T}$ and its adjoint $\mathbf{T}'$ can be implemented in a manner similar to that discussed in Appendices B and C, by replacing the original wavefields with the image-space phase-encoded wavefields.

INTRODUCTION

Wave-equation tomography aims to solve for earth models that explain observed seismograms under some norm. There are two main categories, depending on the domain in which the objective function is computed. In one category, known as waveform inversion (Lines and Treitel, 1984; Tarantola, 1987; Woodward, 1992), the objective function is defined in the data space, where the modeled data are compared with the recorded seismograms. In the other category, here called image-space wave-equation tomography (ISWET), the objective function is minimized in the image space. Two variants of ISWET are wave-equation migration velocity analysis (WEMVA) (Sava and Biondi, 2004a,b) and differential semblance velocity analysis (DSVA) (Shen, 2004; Shen and Symes, 2008).

Like waveform inversion, ISWET is a computationally demanding process. This computational cost is commonly decreased by using generalized sources (Shen and Symes, 2008; Tang et al., 2008). Because wavefield propagation is a linear process, generalized sources are computed by linearly combining source wavefields and receiver wavefields, using phase-encoding techniques (**??**). In particular, Guerra et al. (2009b) used phase-encoding modeling in the image space to synthesize generalized source functions that drastically decrease the cost of DSVA.

WEMVA and DVSA seek the optimal slowness by driving an image perturbation to a minimum. However, they differ in the way the image perturbation is computed and, consequently, in the numerical optimization scheme applied. As Biondi (2008) points out, WEMVA is not easily automated. The image perturbation is computed by the linearized residual prestack-depth migration (Sava and Biondi, 2004a), which uses a manually picked residual-moveout parameter. Because the perturbed image computed with the linearized residual prestack-depth migration is consistent with the application of the forward wave-equation tomographic operator, the forward and adjoint ISWET operators can be used in conjugate-gradient methods to invert for the slowness perturbation. In DSVA, the perturbed image is computed by applying the fully automated differential-semblance operator (DSO) to the subsurface-offset gathers (ODCIGs) or angle gathers (ADCIGs). When applied to ODCIGs, DSVA minimizes the energy not focused at zero-offset. When applied to ADCIGs, DSVA minimizes energy departing from flatness of the reflectors. Although DSVA easily automates ISWET, it produces perturbed images that do not present the depth phase-shift introduced by the forward one-way ISWET operator, neither the DVSA amplitude behavior can be modeled by this operator. Therefore, the objective function computed with DSO is tipically minimized by quasi-Newton algorithms, which require computation of the gradient of the objective function.

The gradient of the objective function can be computed with the Frechét derivatives. However, even for 2D applications of ISWET this computation can be very expensive. An efficient way to compute the gradient without using Frechét derivatives is the adjoint-state method (**??**). **?** describes two methodologies for computing the gradient of the objective function using the adjoint-state method. One methodology uses the perturbation theory, which states that, at first order, a perturbation of the model parameters causes a perturbation of the objective function. The other uses the augmented Lagrangian. The augmented Lagrangian is formed by the objective function and the scalar product of the adjoint-state variables with general solutions of the forward modeling equations. The adjoint-state variables are, in turn, solutions of the adjoint-state equations. The adjoint-state equations are defined by equating to zero the derivatives of the augmented Lagrangian with respect to the state variables. For the linear case, the adjoint of the modeling operator applied to the adjoint-state variables gives the gradient of the objective function.

Although previous studies have computed the gradient of the ISWET objective function by the adjoint-state method (for example, **?**), they have not provided a detailed derivation. Here, I show a detailed derivation the gradient of the ISWET objective function using the augmented Lagrangian methodology. The derivation is valid whether ISWET uses areal-shot migration or shot-profile migration. A complete description of the forward and adjoint of ISWET operators is given in Tang et al. (2008). A numerical example of slowness optimization on the Marmousi model illustrates the use of the gradient by a quasi-Newton algorithm.

Because I use image-space phase-encoded gathers in the numerical example, for completeness, I first briefly describe how to compute these phase-encoded gathers. A detailed treatment of the image-space phase-encoded gathers can be found in Biondi (2006b); **?** and Guerra and Biondi (2008a). Then I derive the ISWET gradient using the adjoint-state method, and show the numerical example .

IMAGE-SPACE PHASE-ENCODED GATHERS

Biondi (2006b); **?** introduced the concept of the prestack exploding-reflector as a generalization of the exploding-reflector method (**?**). The prestack exploding-reflector modeling synthesizes areal data and the corresponding areal source function, having as an initial condition a prestack image computed with wave-equation migration. If the slowness is accurate and the energy is focused at zero-subsurface offset, the prestack exploding-reflector modeling reduces to the conventional exploding-reflector method. Basically, the prestack exploding-reflector method models one single reflection event from one single ODCIG by recursive upward continuation with the following one-way wave equations:

$$\begin{cases} \left(\frac{\partial}{\partial z} - i\sqrt{\omega^2 \hat{s}^2(\mathbf{x}) - |\mathbf{k}|^2}\right) d(\mathbf{x},\omega;x_m,y_m) = r_D(\mathbf{x},\mathbf{h};x_m,y_m) \\ d(x,y,z=z_{\max},\omega;x_m,y_m) = 0 \end{cases}, \tag{4.22}$$

and

$$\begin{cases} \left(\frac{\partial}{\partial z} + i\sqrt{\omega^2 \hat{s}^2(\mathbf{x}) - |\mathbf{k}|^2}\right) u(\mathbf{x},\omega;x_m,y_m) = r_U(\mathbf{x},\mathbf{h};x_m,y_m) \\ u(x,y,z=z_{\max},\omega;x_m,y_m) = 0 \end{cases}, \tag{4.23}$$

where $r_D(\mathbf{x},\mathbf{h};x_m,y_m)$ and $r_U(\mathbf{x},\mathbf{h};x_m,y_m)$ are a single ODCIG at the horizontal location (x_m,y_m) with a single reflector, and are suitable initial conditions for modeling the source and receiver wavefields, respectively. They are obtained by rotating the original unfocused ODCIGs according to the apparent geological dip of the reflector. This operation maintains the velocity information needed for migration velocity analysis, especially for dipping reflectors (**?**). Note that $d(x,y,z=z_c,\omega;x_m,y_m)$ is the areal source data and $u(x,y,z=z_c,\omega;x_m,y_m)$ is the areal receiver data for a single reflector and a single ODCIG located at (x_m,y_m); $z=z_c$ denotes that the wavefields can be collected at any depth level, z_c. This characteristic is important for accelerating ISWET, especially if z_c separates regions of sufficiently accurate slowness above and inaccurate slowness below. Therefore, the synthesized gathers are naturally datumized, and the wavefield propagations during ISWET can be restricted to the region where the slowness model must be updated. This feature allows the application of ISWET to be target-oriented.

As initially formulated, if one models a single reflection from one ODCIG at a time, the prestack exploding-reflector method generates a dataset that can be orders of magnitude bigger than the original dataset. As discussed by Biondi (2006b) and Guerra and Biondi (2008b,a), modeling several reflectors and several ODCIGs simultaneously and using random phase encoding generates a much smaller dataset that, when migrated, do not produce crosstalk. The randomly encoded areal source and areal receiver wavefields can be computed as follows:

$$\begin{cases} \left(\frac{\partial}{\partial z} - i\sqrt{\omega^2 \hat{s}^2(\mathbf{x}) - |\mathbf{k}|^2}\right) \widetilde{d}(\mathbf{x},\mathbf{p}_m,\omega) = \widetilde{r}_D(\mathbf{x},\mathbf{h},\mathbf{p}_m,\omega) \\ \widetilde{d}(x,y,z=z_{\max},\mathbf{p}_m,\omega) = 0 \end{cases}, \tag{4.24}$$

and

$$\begin{cases} \left(\frac{\partial}{\partial z} + i\sqrt{\omega^2 \hat{s}^2(\mathbf{x}) - |\mathbf{k}|^2}\right) \widetilde{u}(\mathbf{x},\mathbf{p}_m,\omega) = \widetilde{r}_U(\mathbf{x},\mathbf{h},\mathbf{p}_m,\omega) \\ \widetilde{u}(x,y,z=z_{\max},\mathbf{p}_m,\omega) = 0 \end{cases}, \tag{4.25}$$

where $\widetilde{r}_D(\mathbf{x},\mathbf{h},\mathbf{p}_m,\omega)$ and $\widetilde{r}_U(\mathbf{x},\mathbf{h},\mathbf{p}_m,\omega)$ are the encoded ODCIGs after rotations. They are defined as follows:

$$\widetilde{r}_D(\mathbf{x},\mathbf{h},\mathbf{p}_m,\omega) = \sum_{x_m}\sum_{y_m} r_D(\mathbf{x},\mathbf{h},x_m,y_m)\beta(\mathbf{x},x_m,y_m,\mathbf{p}_m,\omega), \tag{4.26}$$

$$\widetilde{r}_U(\mathbf{x},\mathbf{h},\mathbf{p}_m,\omega) = \sum_{x_m}\sum_{y_m} r_U(\mathbf{x},\mathbf{h},x_m,y_m)\beta(\mathbf{x},x_m,y_m,\mathbf{p}_m,\omega), \tag{4.27}$$

where $\beta(\mathbf{x}, x_m, y_m, \mathbf{p}_m, \omega) = e^{i\gamma(\mathbf{x}, x_m, y_m, \mathbf{p}_m, \omega)}$ is a pseudo-random phase-encoding function, with $\gamma(\mathbf{x}, x_m, y_m, \mathbf{p}_m, \omega)$ being a uniformly distributed random sequence in $\mathbf{x}$, x_m, y_m and ω; the variable $\mathbf{p}_m$ is the index of different realizations of the random sequence. The recursive solution of equations 4.24 and 4.25 gives the encoded areal source data $\widetilde{d}(x, y, z = z_c, \mathbf{p}_m, \omega)$ and areal receiver data $\widetilde{u}(x, y, z = z_c, \mathbf{p}_m, \omega)$, at the depth level, z_c.

GRADIENT OF ISWET BY THE ADJOINT-STATE METHOD

The gradient of the objective function can be computed with the Frechét derivatives. However, even for 2D applications of ISWET this computation can be very expensive. An efficient way to compute the gradient without using Frechét derivatives is the adjoint-state method (**??**). **?** describes two methodologies for computing the gradient of the objective function using the adjoint-state method. One methodology uses the perturbation theory, which states that, at first order, a perturbation of the model parameters causes a perturbation of the objective function. The other uses the augmented Lagrangian. The augmented Lagrangian is formed by the objective function and the scalar product of the adjoint-state variables with general solutions of the forward modeling equations. The adjoint-state variables are, in turn, solutions of the adjoint-state equations. The adjoint-state equations are defined by equating to zero the derivatives of the augmented Lagrangian with respect to the state variables. For the linear case, the adjoint of the modeling operator applied to the adjoint-state variables gives the gradient of the objective function.

Although previous studies have computed the gradient of the ISWET objective function by the adjoint-state method (for example, **?**), they have not provided a detailed derivation. Here, I show a detailed derivation the gradient of the ISWET objective function using the augmented Lagrangian methodology. The derivation is valid whether ISWET uses areal-shot migration or shot-profile migration. A complete description of the forward and adjoint of ISWET operators is given in Tang et al. (2008). A numerical example of slowness optimization on the Marmousi model illustrates the use of the gradient by a quasi-Newton algorithm.

Image-space wave-equation tomography aims to iteratively solve for the slowness model, $s = s(\mathbf{x})$, that minimizes the nonlinear objective function:

$$J(s) = \frac{1}{2} \left|\left|\Delta r(s)\right|\right|^2 = \frac{1}{2} \left|\left|r(s) - \mathbf{M} r(s)\right|\right|^2 , \tag{4.28}$$

where $\Delta r = \Delta r(\mathbf{x}, \mathbf{h})$ is the image perturbation that measures the accuracy of the slowness model. To compute Δr, a differential residual-focusing operator $\mathbf{M}$ is applied to the image $r = r(\mathbf{x}, \mathbf{h})$ obtained with the current slowness (Biondi, 2008), using either differential residual prestack migration (Sava and Biondi, 2004a,b) or differential-semblance optimization (DSO) operators (Shen and Symes, 2008). In this paper, operators are represented by bold capital letters.

If the differential residual-focusing operator $\mathbf{M}$ is independent of the slowness, the gradient of this objective function evaluated at the current slowness $\widehat{s} = \widehat{s}(\mathbf{x})$ is

$$\nabla J(s) = \left(\frac{\partial r}{\partial s} \right)' \Bigg|_{s=\widehat{s}} \left(\mathbf{I} - \mathbf{M}' \right) \Delta \widehat{r}, \tag{4.29}$$

where the prime denotes the adjoint, $\mathbf{I}$ is the identity operator, and $\Delta \widehat{r} = \Delta \widehat{r}(\mathbf{x}, \mathbf{h})$ is the perturbed image obtained with the current slowness model. The linear operator $\frac{\partial r}{\partial s}$ defines the mapping $\frac{\partial r}{\partial s} \Delta s = \Delta r$ between the slowness perturbation Δs and the image perturbation Δr; it is called the image-space wave-equation tomographic operator.

Because the image-space wave-equation tomographic operator is composed of different operators, it is difficult to envision from equation 4.29 which operations are performed to compute the gradient. Therefore, for a clear explanation of the operators involved, I use the adjoint-state method to derive the gradient of the objective function (equation 4.28).

In migration with generalized sources or shot-profile migration, the source and receiver wavefields are propagated independently, and the image $r_z = r_z(\mathbf{x}, \mathbf{h})$ at a depth level z, is computed by the crosscorrelation

$$r_z(\mathbf{x},\mathbf{h}) = \sum_{\omega} d_z^*(\mathbf{x}-\mathbf{h},\omega)u_z(\mathbf{x}+\mathbf{h},\omega), \tag{4.30}$$

where $d_z(\mathbf{x},\omega)$ is the source wavefield for a single frequency ω at horizontal coordinates $\mathbf{x} = (x, y)$; $u_z(\mathbf{x},\omega)$ is the receiver wavefield, $\mathbf{h} = (h_x, h_y)$ is the subsurface half-offset, and "*" stands for the complex-conjugate. An additional summation over shots is required when migrating more than one shot. Hereafter, letters d and u stand for source and receiver wavefields, respectively, irrespective of the migration scheme.

In a more compact notation, not explicitly writing the dependencies on $\mathbf{x}$ and $\mathbf{h}$, equation 4.30 can be re-written as follows:

$$r_z = \mathbf{S}\mathbf{D}_z'(\omega)u_z(\omega) = \mathbf{S}\mathbf{U}_z(\omega)d_z^*(\omega), \tag{4.31}$$

where $\mathbf{D}$ and $\mathbf{U}$ are convolutional operators composed of (h_x, h_y)-shifted versions of $d_z(\mathbf{x},\omega)$ and $u_z(\mathbf{x},\omega)$, respectively. Operator $\mathbf{S}$ corresponds to the summation over frequency.

For subsequent depth levels, $d(\mathbf{x},\omega)$ is computed by means of the recursive downward propagation

$$\begin{cases} d_{z+1}(\omega) = \mathbf{T}_z^{\downarrow}(\omega, s)d_z(\omega) \\ d_1(\omega) = q(\omega), \end{cases} \tag{4.32}$$

where $\mathbf{T}_z^{\downarrow}$ is the downward continuation operator, which is a function of the slowness s, and $q(\omega)$ is the source wavefield used as a boundary condition. In the case of conventional shot-profile migration, $q(\omega) = f_s(\omega)\delta(\mathbf{x}-\mathbf{x_s})$ is the source signature located at $\mathbf{x}_s = (x_s, y_s, 0)$. If using the generalized sources in the image space, $q(\omega)$ represents the image-space phase-encoded source wavefield of equation 4.24.

The downward continuation of the receiver wavefield is performed by

$$\begin{cases} u_{z+1}(\omega) = \mathbf{T}_z^{\downarrow}(\omega, s)u_z(\omega) \\ u_1(\omega) = w(\omega), \end{cases} \tag{4.33}$$

where $w(\omega)$ is the recorded data at the surface for shot-profile migration. If using generalized sources in the image space, $w(\omega)$ is the phase-encoded areal receiver wavefield of equation 4.25. In equations 4.32 and 4.33, I omitted the dependencies of the wavefield with respect to $\mathbf{x}$. The subscript *1* in equations 4.32 and 4.33 represents the surface for the shot-profile migration and the "collection" depth level, z_c, for the image-space phase-encoded wavefields.

In the image-space wave-equation tomography problem, the perturbed source and receiver wavefields, and the image perturbation are used to compute the slowness perturbation that updates the current slowness model. From the perturbation theory, we have $d = \widehat{d} + \Delta d$, $u = \widehat{u} + \Delta u$, and, consequently, $r = \widehat{r} + \Delta r$ are physical realizations with $s = \widehat{s} + \Delta s$, where the *hat* refers to fields obtained with the background slowness. To the first order (Born approximation), these perturbed fields are given by

$$\Delta d_{z+1}(\omega) = \mathbf{T}_z^{\downarrow}(\omega, \widehat{s})\Delta d_z(\omega) + \widetilde{\widetilde{\mathbf{D}}}_z(\omega)\Delta s_z \tag{4.34}$$

and

$$\Delta u_{z+1}(\omega) = \mathbf{T}_z^{\downarrow}(\omega, \widehat{s})\Delta u_z(\omega) + \widetilde{\widetilde{\mathbf{U}}}_z(\omega)\Delta s_z. \tag{4.35}$$

The diagonal operators $\widetilde{\widetilde{\mathbf{D}}}_z$ and $\widetilde{\widetilde{\mathbf{U}}}_z$ have in the diagonal entries the scattered source and receiver wavefields, respectively. These wavefields are given by the action of the scattering operator $\Delta \mathbf{T}_z^{\downarrow}$ on the background wavefields:

$$\widetilde{\widetilde{\mathbf{D}}}_z(\omega) = \Delta \mathbf{T}_z^{\downarrow}(\omega, \widehat{s})\widehat{d}_z(\omega) = i\frac{\omega^2 \widehat{s}}{\sqrt{\omega^2 \widehat{s}^2 - |\mathbf{k}|^2}} dz \; \widehat{d}_z(\omega) \tag{4.36}$$

and

$$\tilde{\tilde{\tilde{\mathbf{U}}}}_z(\omega) = \Delta \mathbf{T}_z^{\downarrow}(\omega, \widehat{s})\widehat{u}_z(\omega) = -i \frac{\omega^2 \widehat{s}}{\sqrt{\omega^2 \widehat{s}^2 - |\mathbf{k}|^2}} dz \ \widehat{u}_z(\omega). \tag{4.37}$$

The perturbed image is given by

$$\Delta r_z = \mathbf{S}\left(\widehat{\mathbf{U}}_z(\omega)\Delta d_z^*(\omega) + \widehat{\mathbf{D}}_z'(\omega)\Delta u_z(\omega)\right). \tag{4.38}$$

The matrix representations of equations 4.34, 4.35, 4.38 are

$$\Delta \underline{\mathbf{d}} = \mathbf{T}^{\downarrow}\Delta \underline{\mathbf{d}} + \tilde{\tilde{\tilde{\mathbf{P}}}}\mathbf{S}'\Delta \mathbf{s}, \tag{4.39}$$

$$\Delta \underline{\mathbf{u}} = \mathbf{T}^{\downarrow}\Delta \underline{\mathbf{u}} + \tilde{\tilde{\tilde{\mathbf{U}}}}\mathbf{S}'\Delta \mathbf{s}, \tag{4.40}$$

and

$$\Delta \underline{\mathbf{r}} = \mathbf{S}\left(\widehat{\mathbf{U}}\Delta \underline{\mathbf{d}}^* + \widehat{\mathbf{D}}'\Delta \underline{\mathbf{u}}\right), \tag{4.41}$$

where $\mathbf{S}'$ is a spreading operator that replicates the slowness perturbation for every frequency.

Equations 4.39, 4.40, and 4.41 are the forward modeling equations of the image-space wave-equation tomography problem using the generalized sources or shot-profile schemes. They depend on the state variables $\Delta \underline{\mathbf{d}}$, $\Delta \underline{\mathbf{u}}$, and $\Delta \underline{\mathbf{r}}$. **?** describes how to compute the adjoint states using the augmented functional methodology. By introducing the adjoint-state variables $\underline{\lambda}_d$, $\underline{\lambda}_u$, and $\underline{\lambda}_r$, the augmented Lagrangian reads

$$\begin{aligned}\mathcal{L}(\Delta\underline{\mathbf{d}}, \Delta\underline{\mathbf{u}}, \Delta\underline{\mathbf{r}}, \underline{\lambda}_d, \underline{\lambda}_u, \underline{\lambda}_r; \Delta\mathbf{s}) = \mathcal{R}\left[\tfrac{1}{2}\left|\left|\Delta\underline{\mathbf{r}}\right|\right|^2 - \right. & \\ & \left\langle \underline{\lambda}_d, \left(\mathbf{I}-\mathbf{T}^{\downarrow}\right)\Delta\underline{\mathbf{d}} - \tilde{\tilde{\mathbf{D}}}\mathbf{S}'\Delta\mathbf{s}\right\rangle - \\ & \left\langle \underline{\lambda}_u, \left(\mathbf{I}-\mathbf{T}^{\downarrow}\right)\Delta\underline{\mathbf{u}} - \tilde{\tilde{\mathbf{U}}}\mathbf{S}'\Delta\mathbf{s}\right\rangle - \\ & \left\langle \underline{\lambda}_r, \Delta\underline{\mathbf{r}} - \mathbf{S}\left(\widehat{\mathbf{U}}\Delta\underline{\mathbf{d}}^* + \widehat{\mathbf{D}}'\Delta\underline{\mathbf{u}}\right)\right\rangle.\end{aligned}$$

The adjoint-state variables are computed by taking the derivative of $\mathcal{L}$ with respect to the state variables and equating to zero, which gives

$$\left(\mathbf{I}-\mathbf{T}^{\downarrow}\right)'\underline{\lambda}_d = \widehat{\mathbf{U}}\underline{\lambda}_r, \tag{4.42a}$$

$$\left(\mathbf{I}-\mathbf{T}^{\downarrow}\right)'\underline{\lambda}_u = \widehat{\mathbf{D}}\underline{\lambda}_r, \tag{4.42b}$$

$$\underline{\lambda}_r = \Delta\underline{\mathbf{r}}. \tag{4.42c}$$

Notice that

$$\left(\mathbf{I}-\mathbf{T}^{\downarrow}\right)' = \left(\mathbf{I}-\mathbf{T}^{\downarrow'}\right) = \left(\mathbf{I}-\mathbf{T}^{\uparrow}\right) \tag{4.43}$$

corresponds to the recursive upward propagation operator. Therefore, equations 4.42a and 4.42b can be written as

$$\underline{\lambda}_p = \mathbf{T}^{\uparrow}\underline{\lambda}_d + \widehat{\mathbf{U}}\underline{\lambda}_r, \tag{4.44a}$$

$$\underline{\lambda}_u = \mathbf{T}^{\uparrow}\underline{\lambda}_u + \widehat{\mathbf{D}}\underline{\lambda}_r, \tag{4.44b}$$

which correspond to the recursive upward propagation of the perturbed wavefields resulting from the convolution of the wavefields computed with the current slowness and the perturbed image.

Finally, the gradient of J is

$$\nabla_s J(\mathbf{s}) = \mathbf{S}\left(\widetilde{\widetilde{\mathbf{D}}}' \underline{\lambda}_d + \widetilde{\widetilde{\mathbf{U}}}' \underline{\lambda}_u\right). \tag{4.45}$$

To compute the gradient, the adjoint-state wavefields, $\underline{\lambda}_d$ and $\underline{\lambda}_u$, are upward propagated and cross-correlated in time with the scattered wavefields.

Chapter 5

3D field data example

Bibliography

Bagaini, C., 2006, Overview of simultaneous vibroseis acquisition methods: SEG Technical Program Expanded Abstracts, **25**, 70–74.

Ben-Hadj-Ali, H., S. Operto, and J. Vineux, 2009, Three-dimensional frequency-domain full waveform inversion with phase encoding: SEG Technical Program Expanded Abstracts, **28**, 2288–2292.

Berkhout, A. J., 1997a, Pushing the limits of seismic imaging, PART I: Prestack migration in terms of double dynamic focusing: Geophysics, **62**, 937–953.

———, 1997b, Pushing the limits of seismic imaging, PART II: Integration of prestack migration, velocity estimation, and avo analysis: Geophysics, **62**, 954–969.

Bernstein, M. A., K. E. King, X. J. Zhou, and W. Fong, 2005, Handbook of mri pulse sequences: Medical Physics, **32**, 1452–1452.

Berryhill, J. R., 1979, Wave-equation datuming: Geophysics, **44**, 1329–1344.

Bevc, D., 1997, Imaging complex structures with semirecursive kirchhoff migration: Geophysics, **62**, 577–588.

Billette, F., G. Lambare, and P. Podvin, 1997, Velocity macromodel estimation by stereotomography: SEG Technical Program Expanded Abstracts, **16**, 1889–1892.

Biondi, B., 2006a, Prestack exploding-reflectors modeling for migration velocity analysis: SEG Technical Program Expanded Abstracts, **25**, 3056–3060.

———, 2006b, Prestack exploding-reflectors modeling for migration velocity analysis: 76th Ann. Internat. Mtg., Expanded Abstracts, 3056–3060, Soc. of Expl. Geophys.

———, 2007, Prestack modeling of image events for migration velocity analysis: **SEP-131**, 71–89.

———, 2008, Automatic wave-equation migration velocity analysis: **SEP-134**, 65–78.

Biondi, B., S. Fomel, and N. Chemingui, 1998, Azimuth moveout for 3-D prestack imaging: Geophysics, **63**, 574–588.

Biondi, B. and G. Palacharla, 1996, 3-D prestack migration of common-azimuth data: Geophysics, **61**, 1822–1832.

Biondi, B. and G. Shan, 2002, Prestack imaging of overturned reflections by reverse time migration: SEG Technical Program Expanded Abstracts, **21**, 1284–1287.

Biondi, B. and W. W. Symes, 2004, Angle-domain common-image gathers for migration velocity analysis by wavefield-continuation imaging: Geophysics, **69**, 1283–1298.

Biondi, B. and T. Tisserant, 2004, 3D angle-domain common-image gathers for migration velocity analysis: Geophysical Prospecting, **52**, 575–591.

Black, J. L. and M. S. Egan, 1988, True-amplitude DMO in 3-D: SEG Technical Program Expanded Abstracts, **7**, 1109–1112.

Bleistein, N., J. Cohen, and H. Jaramillo, 1999, True-amplitude transformation to zero offset of data from curved reflectors: Geophysics, **64**, 112–129.

Castoldi, P., 2002, Multiuser detection in CDMA mobile terminals: Artech House Publishers.

Claerbout, J., 1985, Imaging the Earth's Interior: Blackwell Scientific Publications.

Claerbout, J. F., 1971a, Toward a unified theory of reflector mapping: Geophysics, **36**, 467–481.

——, 1971b, Towards a unified theory of reflector mapping: Geophysics, **36**, 467–481.

Clapp, R., 2003, Geologically constrained migration velocity analysis, *in* Ph.D. thesis, Stanford University.

Cruz, J. C. R., P. Hubral, M. Tygel, J. Schleicher, and G. Höcht, 2000, The common reflecting element (CRE) method revisited: Geophysics, **65**, 979–993.

Dinan, E. and B. Jabbari, 1998, Spreading codes for direct sequence CDMA and wideband CDMA cellular networks: IEEE Communications Magazine, **36**, 48–54.

Duquet, B. and P. Lailly, 2006, Efficient 3D wave-equation migration using virtual planar sources: Geophysics, **71**, S185–S197.

Fei, W., P. Williamson, and A. Khoury, 2009, 3-D common-azimuth wave-equation migration velocity analysis: SEG Technical Program Expanded Abstracts, **28**, 2283–2287.

Gelchinsky, B., 1988, The common reflecting element (CRE) method (non-uniform asymmetric multifold system): Exploration Geophysics, **19**, 71–75.

Gold, R., 1967, Optimal binary sequences for spread spectrum multiplexing: IEEE Transactions on Information Theory, **14**, 619–621.

Guerra, C. and B. Biondi, 2008a, Phase encoding with gold codes for wave-equation migration: **SEP-136**, 23–42.

———, 2008b, Prestack exploding reflector modeling: The crosstalk problem: **SEP-134**, 79–92.

Guerra, C., Y. Tang, and B. Biondi, 2009a, Wave-equation tomography using image-space phase encoded data: SEG Technical Program Expanded Abstracts, **28**, 3964–3968.

———, 2009b, Wave-equation tomography using image-space phase-encoded data: **SEP-138**, 95–116.

Hale, D., 1984, Dip-moveout by fourier transform: Geophysics, **49**, 741–757.

Javidi, B., G. Zhang, and J. Li, 1996, Experimental demonstration of the random phase encoding technique for image encryption and security verification: Optical Engineering, **35**, 2506–2512.

Kapoor, S. J., M. O'Brian, D. Desta, I. Atakishiyev, and M. Tomida, 2007, Subsalt imaging — the raz/waz experience: SEG Technical Program Expanded Abstracts, **26**, 926–930.

Kosloff, D., J. Sherwood, Z. Koren, E. Machet, and Y. Falkovitz, 1996, Velocity and interface depth determination by tomography of depth migrated gathers: Geophysics, **61**, 1511–1523.

Kosloff, D., U. I. Zackhem, and Z. Koren, 1997, Subsurface velocity determination by grid tomography of depth migrated gathers: SEG Technical Program Expanded Abstracts, **16**, 1815–1818.

Krebs, J. R., J. E. Anderson, D. Hinkley, R. Neelamani, S. Lee, A. Baumstein, and M.-D. Lacasse, 2009, Fast full-wavefield seismic inversion using encoded sources: Geophysics, **74**, WCC177–WCC188.

Lailly, P., 1983, The seismic inverse problem as a sequence of before stack migrations: Conference on Inverse Scattering, Theory and Application, Society for Industrial and Applied Mathematics, Expanded Abstracts, 206–220.

Levanon, N. and E. Mozeson, 2004, Radar signals: Wiley, John & Sons, Inc.

Liner, C. L., 1991, Born theory of wave-equation dip moveout: Geophysics, **56**, 182–189.

Lines, L. and S. Treitel, 1984, A review of least-squares inversion and its application to geophysical problems: Geophys. Prospecting, **32**, 159–186.

Liu, F., D. W. Hanson, N. D. Whitmore, R. S. Day, and R. H. Stolt, 2006, Toward a unified analysis for source plane-wave migration: Geophysics, **71**, 129–139.

Loewenthal, D., L. Lu, R. Roberson, and J. Sherwood, 1976, The wave equation applied to migration: Geophysical Prospecting, **24**, 380–399.

Martin, J. E., 1993, Simultaneous Vibroseis recording: Geophysical Prospecting, **41**, 943–967.

Moldoveanu, N., J. Kapoor, and M. Egan, 2008, Full-azimuth imaging using circular geometry acquisition: The Leading Edge, **27**, 908–913.

Mulder, W. A. and A. P. E. ten Kroode, 2002, Automatic velocity analysis by differential semblance optimization: Geophysics, **67**, 1184–1191.

Peles, O., A. Bartana, D. Kosloff, and Z. Koren, 2004, Limitations of the exploding reflector model in sub-salt imaging: SEG Technical Program Expanded Abstracts, **23**, 2455–2457.

Regone, C. J., 2007, Using 3d finite-difference modeling to design wide-azimuth surveys for improved subsalt imaging: Geophysics, **72**, SM231–SM239.

Rickett, J., B. Biondi, and D. Lumley, 1996, Modeling heterogeneous reservoirs using the first order Born approximation: **SEP-92**, 75–82.

Rickett, J. E. and P. C. Sava, 2002, Offset and angle-domain common image-point gathers for shot-profile migration: Geophysics, **67**, 883–889.

Rietveld, W. E. A. and A. J. Berkhout, 1992, Prestack depth migration by means of controlled illumination: Geophysics, **59**, 801–809.

Rietveld, W. E. A., A. J. Berkhout, and C. P. A. Wapenaar, 1992, Optimum seismic illumination of hydrocarbon reservoirs: Geophysics, **57**, 1334–1345.

Romero, L., D. Ghiglia, C. Ober, and S. Morton, 2000, Phase encoding of shot records in prestack migration: Geophysics, **65**, 426–436.

Sava, P., 2003, Prestack residual migration in frequency domain: Geophysics, **68**, 634–640.

Sava, P. and B. Biondi, 2004a, Wave-equation migration velocity analysis-I: Theory: Geophysical Prospecting, **52**, 593–606.

———, 2004b, Wave-equation migration velocity analysis-II: Examples: Geophysical Prospecting, **52**, 607–623.

Sava, P. and S. Fomel, 2006, Time-shift imaging condition in seismic migration: Geophysics, **71**, S209–S217.

Sava, P. C. and S. Fomel, 2003, Angle-domain common-image gathers by wavefield continuation methods: Geophysics, **68**, 1065–1074.

Schultz, P. S. and J. Claerbout, 1978, Velocity estimation and downward continuation by wavefront synthesis: Geophysics, **43**, 691 714.

Shen, P., 2004, Wave-equation Migration Velocity Analysis by Differential Semblance Optimization: PhD thesis, Rice University.

Shen, P. and W. W. Symes, 2008, Automatic velocity analysis via shot profile migration: Geophysics, **73**, VE49–VE59.

Stork, C., 1992, Reflection tomography in the postmigrated domain: Geophysics, **57**, 680–692.

Sun, P., S. Zhang, and F. Liu, 2002, Prestack migration of areal shot records with phase encoding: 72nd Ann. Internat. Mtg, Soc. Expl. Geophys., Expanded Abstracts, 1172–1175.

Symes, B., 2008, Migration velocity analysis and waveform inversion: Geophysical Prospecting, **56**, 765–790.

Tang, Y., 2009, Target-oriented wave-equation least-squares migration/inversion with phase-encoded hessian: Geophysics, **74**, WCA95–WCA107.

Tang, Y., C. Guerra, and B. Biondi, 2008, Image-space wave-equation tomography in the generalized source domain: **SEP-136**, 1–22.

Tarantola, A., 1987, Inverse problem theory: Methods for data fitting and model parameter estimation: Elsevier.

Teh, P. C., P. Petropoulos, M. Ibsen, and D. J. Richardson, 2001, A comparative study of the performance of seven and 63-chip optical code-division multiple-access encoders and decoders based on superstructured fiber bragg gratings: Journal of Lightwave Technology, **19**, 1352–1365.

Thorbecke, J. and A. J. Berkhout, 2006, Recursive prestack depth migration using CFP gathers: Geophysics, **71**, S273–S283.

Tygel, M., J. Schleicher, P. Hubral, and L. T. Santos, 1998, 2.5-D true-amplitude kirchhoff migration to zero offset in laterally inhomogeneous media: Geophysics, **63**, 557–573.

Vigh, D. and E. W. Starr, 2008, 3d prestack plane-wave, full-waveform inversion: Geophysics, **73**, VE135–VE144.

Virieux, J. and S. Operto, 2009, An overview of full-waveform inversion in exploration geophysics: Geophysics, **74**, WCC1–WCC26.

Wang, B., V. Dirks, P. Guillaume, F. Audebert, and D. Epili, 2006, A 3d subsalt tomography based on wave-equation migration-perturbation scans: Geophysics, **71**, E1–E6.

Wang, R. K., I. A. Watson, and C. Chatwin, 1996, Random phase encoding for optical security: Optical Engineering, **35**, 2464–2469.

Ward, R. M., R. H. Brune, A. Ross, and L. H. Kumamoto, 1990, Phase encoding of Vibroseis signals for simultaneous multisource acquisition: SEG Technical Program Expanded Abstracts, **9**, 938–941.

Weishaupt, D., V. Koechli, and J. M.Froehlich, 2006, How Does MRI Work? : An Introduction to the Physics and Function of Magnetic Resonance Imaging.

Whitmore, N. D., 1995, An imaging hierarchy for common angle plane wave seismograms, *in* Ph.D. thesis, University of Tulsa.

Woodward, M. J., 1992, Wave-equation tomography: Geophysics, **57**, 15–26.

Yamada, H., K. Takada, and S. Mitachi, 1998, Crosstalk reduction in a 10-ghz spacing arrayed-waveguide grating by phase-error compensation: Journal of Lightwave Technology, **16**, 364–371.

Yang, T. and P. Sava, 2009, Wave-equation migration velocity analysis using extended images: SEG Technical Program Expanded Abstracts, **28**, 3715–3719.

Zigangirov, K., 2004, Theory of code division multiple access communication: Wiley, John & Sons, Inc.